Development and Dosimetry of a Conformal Superficial Brachytherapy Device

BY

Brent Joyner Rogers

A DISSERTATION
SUBMITTED TO THE FACULTY OF THE GRADUATE SCHOOL OF THE

University of Minnesota

IN PARTIAL FULFILLMENT FOR
THE DEGREE OF

Doctor of Philosophy in Medical Physics

Clara Ferreira, Ph.D. (Advisor)

September, 2020

For my family.

ACKNOWLEDGMENTS

What a long and winding road it has been. I would like to thank my advisor, Dr. Clara Ferreira. Although I was Dr. Ferreira's first Ph.D. student, her knowledge, skills, and management abilities were more representative of a veteran. Clara kept me focused and showed me what takes to be a great researcher and medical physicist. I was very lucky to have her as a mentor. I would also like to Dr. Jessica Lawrence. She is an incredibly skilled researcher and author. My writing has improved immensely through her guidance. I would also like to thank Dr. Lawrence for her contributions during the experiments. Thank you to Dr. Eric Ehler. Without his insight and deep understanding of physics, this project would not have been possible. Additionally, thank you to Dr. Parham Alaei for your contributions to this work and your steadfastness as the program director. Thank you to Jennifer Chmura for contributing your engineering expertise and constructing the CSBT device.

I would also like to thank Dr. Chris Wilke for lending his expertise during the weekly research meetings. Thank you to the remaining professors in the department who have taught me so much: David Sterling, Dr. Damian Mathew, Dr. Yoichi Watanabe, and Dr. Jianling Yuan. Thank you to the administrative staff for keeping the department running smoothly. Thank you to all of my friends and classmates.

Finally, a heartfelt thank you to my family. My wife, Julia, is the definition of dedication. My mother, Marilou, who is the matriarch of our family, has been an absolute rock. My father, Ben, showed me how to work hard and succeed. My brothers, Scott and Erik, whose dedication to their children have made me a better father.

ABSTRACT

Shortly after their discovery in 1895, x-rays began to be used to treat dermatologic ailments and malignant tumors. Superficial brachytherapy is the process of using ionizing radiation to kill skin cancer cells and is the oldest form of radiation therapy. Advancements in technology and our understanding of how ionizing radiation interacts with matter have led to vast improvements in the quality and efficacy of care in cancer treatment. Contemporary radiation therapy techniques for the treatment of cutaneous malignancies are diverse. The most common radiation therapy modality is external beam radiation therapy with standard fractionation. Recently, there has been a resurgence in applying superficial brachytherapy techniques with the introduction to the market of high dose remote afterloading brachytherapy applicators and electronic brachytherapy units, which provide fast, reliable, and effective treatments. However, currently available commercial devices are limited in that they are incapable of providing patient-specific dose distributions. Addressing those limitations, a conformal superficial brachytherapy (CSBT) applicator was manufactured and rigorously tested. The applicator was designed to house between one and 19 yttrium-90 (^{90}Y) beta-minus radiation sources. Each source was affixed to the distal end of one of 19 translatable rods, which allowed each of the sources to be moved in parallel with one another to varied locations. The goal of this work was to examine the capability of the CSBT applicator to deliver patient-specific treatments and to maximize the conformality of planned dose distributions to uneven surfaces. The work presented in this thesis relied heavily on Monte Carlo (MC) simulation and film-based measurement methods to determine dose rates. It was necessary to benchmark and validate the MC code to know its accuracy in simulating the novel ^{90}Y source's dose rates. The

CSBT source was characterized under standard treatment conditions. Next, examples of dose rate distributions from multiple sources are presented. Lastly, the clinical results of a murine model dose rate escalation study are presented. This work shows that, with the CSBT applicator, it is possible to deliver accurate and conformal dose to superficial tissue.

CONTENTS

Dedication i

Acknowledgments ii

Abstract iii

Contents v

List of Tables vii

List of Figures viii

List of Symbols & Abbreviations xi

1 Introduction 1

1.1 Overview 1
1.2 Description of Chapters 3

2 Background 5

2.1 Skin 5

2.1.1 Skin Anatomy 5
2.1.2 Stochastic Effects of Radiation Exposure to Skin 7
2.1.3 Deterministic Effects of Radiation Exposure to Skin 7
2.1.4 Skin Cancers 10
2.1.5 Skin Cancer Treatment Modalities 13

2.2 Contemporary Superficial Brachytherapy Applicators 15

2.2.1 HDR Surface Brachytherapy Applicators 15
2.2.2 Electronic Source Brachytherapy 17
2.2.3 Molds and Radioactive Patches 19
2.2.4 Strontium Probe 19

2.3 Therapeutic Electrons and their Interactions with Matter 20
2.4 Beta-Minus Nuclear Decay 22
2.5 ^{90}Y Production 26
2.6 Dose Measurement and Calculation 27

2.6.1 Radiochromic Film Dosimetry 27
2.6.2 Monte Carlo Radiation Transport Simulation 29
2.6.3 Analytical Methods for Determination of β^- Source Dose Rates 32

3 Methodology **36**

3.1 The Conformal Superficial Brachytherapy Applicator 36

3.1.1 ^{90}Y Source Description 39
3.1.2 ^{90}Y Source Placement Procedure 39

3.2 Dose Rate Determination 40

3.2.1 Film Calibration 40
3.2.2 Experimental Measurements 41
3.2.3 Monte Carlo Transport Simulations 42
3.2.4 Gamma Analysis 45

4 ^{90}Y Source Characterization **50**

4.1 Benchmark Simulation 51
4.2 Simulation Validation 53
4.3 Dose Rate Uncertainties 59
4.4 Discussion 61

5 Conformal Superficial Brachytherapy Applicator Characterization **63**

5.1 Effect of increasing the Tip-to-Surface Distance 64
5.2 Effect of the Tip on Dose Distribution 65
5.3 Source Position and Activity Optimization 67
5.4 Superposition of Two Sources 70
5.5 Discussion 72

6 Murine Model Dose Escalation Study **74**

6.1 Introduction 74
6.2 Materials and Methods 75

6.2.1 CSBT Device 75
6.2.2 Pre-Experiment Quality Assurance 76
6.2.3 Animal Preparation 77
6.2.4 Monitoring of Mice and Collection of Skin Samples 77

6.3 Results 78
6.4 Discussion 82

7 Summary and Recommendations for Future Work **84**

7.1 Summary 84

Bibliography **87**

Appendix A **97**

Appendix B **99**

LIST OF TABLES

2.1. Basic terminology of radiation-induced skin injury. (From ICRP-59).....8

2.2. Special case terminology of radiation-induced skin injury. (From ICRP-59) 9

2.3. RTOG/EORTC radiation morbidity scoring criteria for human skin. 9

2.4. Simplified AJCC (7^{th} Ed.) TNM scale of non-melanoma and non-Merkel cell carcinoma staging. 10

2.5. Karnofsky performance status 15

2.6. ECOG performance status 15

2.7. Properties of five neutron activated beta emitters. Some of the nuclides may be obtained by means other than by neutron activation. 24

3.1. Gamma analysis results showing the differences between the Matlab (ML) script and the MapCheck (MC) software.....48

4.1. Estimated uncertainty in dose rate to water from a tipped ^{90}Y source. 59

5.1. Widths of surface dose profiles at different percentages of maximum dose for TSDs: 0.0, 0.01, 0.02, 0.03, 0.04, & 0.05 cm. 64

6.1. Modified VRTOG acute skin toxicity scoring criteria 78

6.2. Mouse irradiation schedule 79

LIST OF FIGURES

2.1. A simplified depiction of human skin. Ten days following a single dose of radiation, damage to the epidermis may be observed as an early (or acute) reaction. Damage to the dermis, primarily to the vasculature, may appear as a late reaction months after exposure. (Figure from Hall and Giaccia, 2012 [20]).....6

2.2. Decay diagram for ^{90}Y. (Figure from iaea.org) 25

2.3. Radiochromic EBT3 film layer structure.....27

2.4. (a) Probability density function. (b) Continuous probability distribution. 32

3.1. Drawing of the Conformal Superficial Brachytherapy Device (CSBT). (a) CSBT in its initial position. The patient-specific 3D printed insert is placed in the proximal end of the carriage tray. (b) CSBT in its treatment position. The upper actuator is in its forward position, bringing the 3D printed insert into the rod channels and moving the rods to their treatment positions 37

3.2. The transverse cross-sectional view of the rod holder. The rods, and therefore the tips and sources, are arranged in a hexagonal arrangement and have a center-to-center distance (C2C) of 0.45 cm. 37

3.3. A picture of a 3D printed insert. 38

3.4. Drawing of the 3D printed rod tip. Each tip is placed on a rod and is held in place via interference. The source is located within a tapered cavity at the distal end of the tip. 38

3.5. A picture of a 3D printed insert. 38

3.6. ^{90}Y CSBT device source loading procedure. 41

3.7. The beta particle energy spectrum of ^{90}Y. The data was extracted from ICRU56. 42

3.8. Typical geometry of an MCNP5 single tipped source dose rate simulation. 44

3.9. Eight comparisons of the Matlab script and MapCheck planar dose distributions displaying the failed gamma analysis points for each. 49

4.1. (a) MC simulation scoring geometry for the benchmarking dose point kernel simulations. (b) Relative error of the benchmarking simulation. 52

4.2. MCNP5 benchmarking simulation dose rate and total energy deposited as a function of distance (r).....53

4.3. MC simulated and measured depth dose rates for a bare and a tipped ^{90}Y source placed on the surface of a water-equivalent phantom. The thickness of the EBT3 film was radiologically scaled to make the depth of measurement water equivalent. The error bars represent the total combined uncertainty (k = 1) of each measurement. 54

4.5. Dose distribution in water for ^{90}Y superficial brachytherapy source within the source holder tip of the CSBT applicator. 56

4.4. Film-based measured and MC simulated dose rate profiles in water at d = 0.0171 cm and 0.1171 cm or 0.1513 cm. (a) Profiles for a bare source placed on the surface of a water-equivalent phantom. (b) Profiles for a tipped source with the distal end of the tip placed. 56

4.6. Planar dose rate distributions at d = 0.0171 cm for six tipped sources located directly on the water equivalent phantom surface. (a) Relative measured and MC simulated planar distributions. (b) MC simulated planar dose rate distribution. The red crosses indicate the calculation points of the measured dose rate distribution where gamma analysis criteria were not met. The passing rate for this analysis was 91.58%. 57

4.7. MC simulated relative dose profiles for a single tipped source and a matrix of seven sources. The seven-source profile at y = 0 in Figure 4.6. (a) Depths in water of 0.0171 cm and 0.1171 cm. (b) Depths in water of 0.2171cm and 0.3171 cm. 58

4.8. Type A simulation error for tipped single and seven-source MC simulations at depths: 0.0171 cm, 0.1171 cm, 0.2171 cm, and 0.3171 cm. 60

5.1. Relative profile dose distributions for TSDs: 0.0, 0.1, 0.2, 0.3, 0.4, & 0.5 cm. 65

5.2. Central axis depth dose rates for tipped CSBT sources with increasing TSDs. (a) Absolute dose rates in cGy s^{-1} Bq^{-1}. (b) Percentage depth dose rates normalized to the maximum dose rates for each TSD. 66

5.3. (a) MC simulated profile depth dose distributions showing the effect of the 3D printed source tip when TSD = 0 cm. The dotted line shows the dose distribution of the standard tip-on-surface setup. The dotted line represents the distribution for the exact same setup except that the tip is removed. (b) Percent profile dose at d = 0.0171 cm (surface) and d = 0.1171 cm for the tipped and "not tipped" CSBT source. 67

5.4. Positions and relative activities of the tip-source-rod assemblies for the four MC simulated dose distributions (shown in Figure 5.5). The grey circles represent the sources that were included in the simulations and the white circles represent possible positions of sources that were not included in the simulations. (a) Source numbers. (b) Source TSDs in mm. (c) Relative source

activities in percent. (d) Source TSDs in mm (top) and relative source activities in percent (bottom).....68

5.5. MC simulated dose distributions at $d = 0.1$ cm for the exposure of a hypothetical "C" shaped target. (a) Each source had a TSD of 0.1 cm and equal activity. (b) Each source had an equal relative activity. The TSDs of each source was adjusted to redistribute the dose distribution. (c) Each source had an equal TSD of 0.1 cm and the relative source activities were adjusted. (d) The TSD and relative activity of each source was adjusted. 69

5.6. Normalized MC simulated planar dose rates for two CSBT sources with a TSD of 0.0 cm. The dashed lines represent the single simulation of two sources. The solid lines represent the superimposed dose rate distribution from a single source. 70

5.7. Percent surface profile dose of two CSBT sources for TSDs: 0.0 cm, 0.1 cm, 0.2 cm, and 0.3 cm. Each source was positioned on the x-axis. Profiles are shown for y = 0.0 cm, 0.1 cm, and 0.2 cm. 71

6.1. Picture of the distal (treatment) end of the CSBT device with 10 ^{90}Y sources and the modified tips (Tip-surface). 75

6.2. MC simulated relative surface dose profiles for Tip-0.5mm and Tip-surface. (a) Surface profiles from a single source. (b) Source profiles from two sources with a center-to-center spacing of 0.45 cm. 80

6.3. Pretreatment quality assurance CSBT film-based surface dose distributions: (a) standard tips (Tip-0.5mm) and (b) modified tips (Tip-surface).....81

6.4. Time course of radiation-induced skin dermatitis following exposure from the ^{90}Y-based CSBT device. 82

6.5. Mean skin toxicity scores (Modified VRTOG scheme) following exposure from the CSBT device. 83

LIST OF SYMBOLS & ABBREVIATIONS

^{166}Ho	holmium-166
^{188}Re	rhenium-188
^{192}Ir	iridium-192
^{32}P	phosphorous-32
^{89}Y	yttrium-89
^{90}Sr	strontium-90
^{90}Y	yttrium-90
^{90}Zr	zirconium-90
β^-	beta-minus particle, electron
β^+	beta-plus particle, positron
γ	gamma particle
λ	radioactive decay constant
μ	linear attenuation coefficient
ν	neutrino
σ	nuclear cross-section
φ	particle fluence
3D	three-dimensional
A	radioactive activity or mass number
ADCL	Accredited Dosimetry Calibration Laboratory
AJCC	American Joint Committee on Cancer
Au	gold
BCC	basal cell carcinoma
BT	brachytherapy
C & E	curettage and electrodesiccation
CSBT	conformal superficial brachytherapy
DD	dose difference
d_{max}	depth of maximum dose
DNA	deoxyribonucleic acid
DTA	distance to agreement
eBT	electronic brachytherapy
electron EBRT	electron external beam radiation therapy
EORTC	European Organization for Research and Treatment of Cancer
ESTRO	European Society for Therapeutic Radiology and Oncology

EWT	electroweak theory
FWHM	full-width half-maximum
GEC	Groupe Européen de Curiethérapie
HDR	high dose rate
ICRP	International Commission on Radiological Protection
ICRU	International Commission on Radiation Units and Measurements
IMRT	intensity-modulated radiation therapy
IVBT	intravascular brachytherapy
Li	lithium
LNT	linear non-threshold
MC	Monte Carlo
MCNP5	Monte Carlo n-particle code – version 5
MURR	University of Missouri Research Reactor Center
n	neutron
NCCN	National Comprehensive Cancer Network
netOD	net optical density
NIST	National Institute of Standards and Technology
NMSC	non-melanoma skin cancer
p	proton
PCDA	pentacosa-10,12-diynoate
photon EBRT	photon external beam radiation therapy
PMMA	poly(methyl methacrylate)
QA	quality assurance
ROI	region of interest
r_{rad}	radiological distance
RT	radiation therapy
RTOG	Radiation Therapy Oncology Group
SCC	squamous cell carcinoma
SW	solid water
TLD	thermoluminescent dosimeter
TNM	tumor, node, metastasis
TSD	tip-to-surface distance
VROTG	Veterinary Radiation Therapy Oncology Group
Z	atomic number

Chapter 1

INTRODUCTION

1.1 Overview

Each year, more people are diagnosed with skin cancer than all other cancers combined [1]. Non-melanoma skin cancer (NMSC) is the most common. In 2012, the United States incidence was near 4.0 million, with 2.5 million people treated [2]. Basal cell carcinoma and squamous cell carcinoma comprised approximately 99% of those tumors, with the remaining 1% being Merkel cell carcinoma, Kaposi sarcoma, dermatofibrosarcoma, or others [3–5]. Actinic keratoses are the most common keratinocyte-derived precancerous lesion in humans, and the incidence of these lesions is rising in the aging population [6], stressing the need for early intervention and effective, well-tolerated therapies.

The standard of care treatment for NMSC is surgery; however, radiation therapy (RT) is commonly recommended for patients with incompletely removed tumors, unresectable tumors, and for those who decline surgery or have poor performance scores and are not good surgical candidates [7–11]. For these patients, RT provides effective tumor control with recurrence-free rates exceeding 90% [12–15]. While external electron

beam radiation therapy (electron EBRT), external photon beam radiation therapy (photon EBRT), brachytherapy (BT), and electronic BT (eBT) have been well described, many skin tumors on curved and irregular surfaces (e.g., on the face, head, and neck) are inherently challenging to treat with all of these approaches. The efficacy of RT is dependent on precisely targeting neoplastic cells while minimizing dose to normal tissue. For well-defined and superficial NMSC treated with radiation, it is ideal to limit radiation penetration to ensure that the dose extends minimally beyond the target lesion's thickness. Electron EBRT provides an advantage over photon EBRT since electrons have lower penetrating power because they interact via Coulombic forces. However, electron EBRT may fail to deliver conformal dose distributions for small and irregular fields, compromising tumor control [16].

In recent years, iridium-192 (^{192}Ir) based high dose rate (HDR) surface brachytherapy applicators have gained popularity for the treatment of NMSC. These applicators are available in various fixed sizes and place the ^{192}Ir source above the target such that a circular or oval-shaped dose distribution occurs at the target surface. These applicators are limited by the size and shape of the shielding cup intrinsic to the devices. Being a gamma particle emitter, ^{192}Ir penetrates to depths beyond the thickness of many NMCS lesions. The result is that HDR surface brachytherapy applicators are incapable of providing conforming doses to complex and shallow target lesions.

To address the need for improved dose conformity for superficial brachytherapy, a conformal superficial brachytherapy device (CSBT) has been designed and built [17–19]. The CSBT device places up to 19 hexagonally arranged sources on a target. Each source is independently translatable along the direction normal to the target surface, which, compared to HDR surface brachytherapy applicators, significantly improves the control of the dose distributions by selecting the position and involvement of each of the 19 sources. The current version CSBT device radiation source is yttrium-90 (^{90}Y), which, being a beta-

minus particle emitter, is approximately 10-fold less penetrating than ^{192}Ir. In the treatment of superficial NMSC with radiation, the ideal dose penetration is low and does not extend beyond the thickness of human skin (0.4 mm to 0.5 mm). Thus, this elegant, user-friendly CSBT device improves dose-target conformity, which is expected to result in improved cosmesis and fewer complications.

The primary goal of this project was to examine the potential of the CSBT device as a clinically viable mode of treatment of NMSC. Three specific aims were defined to achieve this goal. The first aim was to fully characterize the ^{90}Y source. The second aim was to describe the variability and control of the CSBT dose distribution using varying source numbers and positions. The final aim was to determine the appropriate dose to administer with the CSBT device and determine the temporal association between radiation and radiation-induced dermatitis. The characterizations of the ^{90}Y source and the CSBT produced dose distributions were performed by film-based measurement and by Monte Carlo (MC) simulation. The final aim was achieved by performing a dose-escalation study in a non-tumor murine model, monitoring the clinical grade of radiation-induced tissue damage following exposure. Following euthanasia of the animal subjects, skin samples were collected, stabilized, and stored for future histologic examination.

1.2 Description of Chapters

Chapter 2 presents the background information relevant to this work. Basal cell and squamous cell carcinomas are introduced. Human skin anatomy, skin cancer, and the detrimental and therapeutic effects that radiation has on skin are discussed. The theory and physics of the methods used in this work to determine dose deposition are also discussed.

Chapter 3 presents the general methodology of this work. The CSBT device is presented. The methods of film-based measurements and MC simulation for determining dose rates under various conditions is presented. A gamma analysis program was

developed and tested to compare dose distributions empirically and through MC simulation.

Chapter 4 discusses the measurements performed to characterize the ^{90}Y CSBT source. To ensure the simulated data's reliability, benchmarking and validation of the MC software and input files were performed. Film-based measurements and the three-dimensional ^{90}Y dose distributions were obtained.

In Chapter 5, the CSBT device is fully characterized, focusing on the dose distributions from multiple ^{90}Y sources and source positions. An examination of the effect of the source mounting components was performed. Simulations were performed to demonstrate possible dose distribution optimization methods.

Chapter 6 demonstrates the clinical capability of the CSBT device. A dose-escalation study was performed in a non-tumor murine model. Following exposure, skin toxicity was monitored and graded daily.

Chapter 7 summarizes this work. Discussion and conclusions are presented as well as recommendations for the future development of the CSBT.

Chapter 2

BACKGROUND

2.1 Skin

Skin is the largest organ in humans and makes up roughly 7% of a typical human body mass. Exposure to ionizing radiation may cause the skin to exhibit various deterministic and/or stochastic effects. When exposed to beta particles or low energy X-rays (<5-10 keV), the biological response of the skin shows a strong dependence on the energy of the incident particles. It is, therefore, necessary to keep in mind the anatomical structure of exposed skin.

2.1.1 Skin Anatomy

As depicted in Figure 2.1, human skin consists of three distinct layers; the stratified, cellular epidermis; the dermis of connective tissue; and the subcutaneous layer. Depending on the body site, the epidermis may be as thin as 20 μm or as thick as 500 μm [20]. International Commission on Radiological Protection (ICRP) Publication 59 proposed a standardized epidermis thickness of 20 to 100 μm [21], which has been adopted by the International Commission on Radiation Units and Measurements (ICRU) [22]. The

epidermis consists of five layers. From most shallow to most deep, those layers are the stratum corneum, the stratum lucidum, the stratum granulosum, the stratum spinosum, and the stratum basale. Ninety percent of the epidermis is made up of keratinocytes, which originate in the stratum basale. As keratinocytes differentiate, they are pushed up through the layers of the epidermis. The most superficial layer, the stratum corneum, is made up of dead keratinocytes.

Melanocytes are pigment-producing cells and are located near the epidermis stratum basale and in the inner ear, the choroid and iris of the eye, the vaginal epithelium, and the meninges. These cells produce melanin, which, upon production, is transferred to neighboring keratinocytes in the epidermis and the growing shaft of hair follicles. Melanin production protects the skin from harmful ultraviolet radiation.

The dermis is sandwiched between the epidermis and the subcutaneous hypodermis. It consists of mostly collagen and elastic fibers and provides protection and

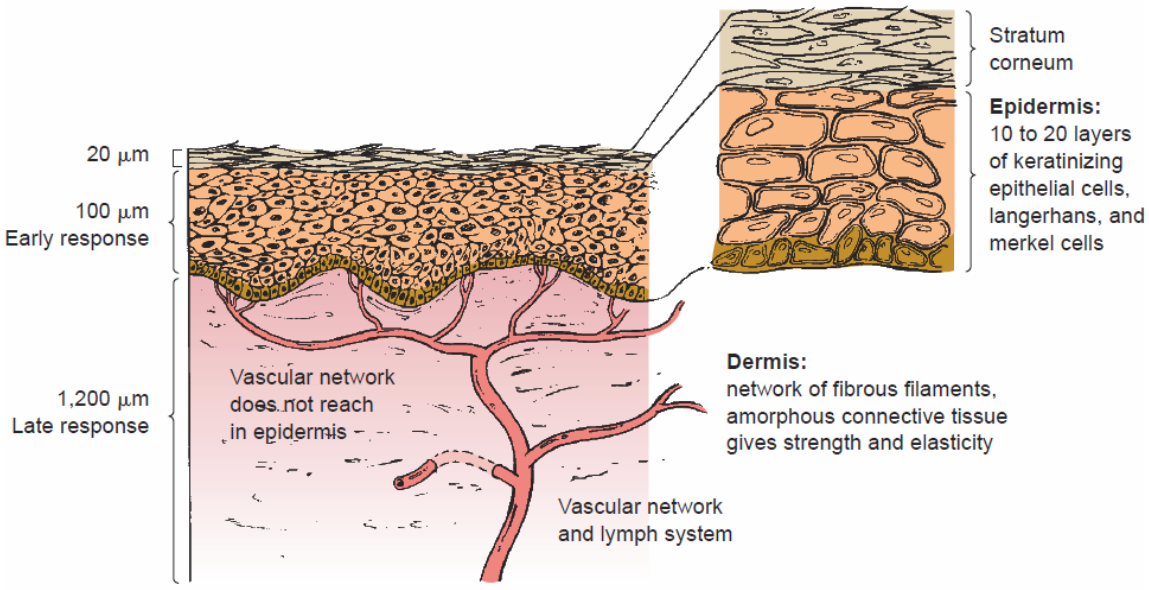

Figure 2.1. A simplified depiction of human skin. Ten days following a single dose of radiation, damage to the epidermis may be observed as an early (or acute) reaction. Damage to the dermis, primarily to the vasculature, may appear as a late reaction months after exposure. (Figure from Hall and Giaccia, 2012 [20])

support for various other structures, such as the cutaneous lymph system, sebaceous glands, sweat glands, and hair follicles. It is divided into two layers: the papillary dermis and the reticular dermis. The more superficial papillary layer is composed of highly vascular and loose connective tissue. The deeper reticular layer constitutes most of the dermal layer and is composed of dense connective tissue.

2.1.2 Stochastic Effects of Radiation Exposure to Skin

The ICRP supports that, for purposes of radiation protection, for doses as low as 100 mSv, it is plausible to assume that an increase in the equivalent dose to tissue will result in a directly proportional increase in the probability of developing cancer in that tissue [23]. Although various dose-response models have been hypothesized, the ICRP radiation protection recommendations are based on the "linear no-threshold" model (LNT) of stochastic risk.

According to the LNT model, the probability of skin cancer induction is directly proportional to the absorbed dose, the area of exposed skin, and is higher for areas of skin routinely exposed to sunlight. However, the component of risk related to skin exposed to sunlight is also dependent on the degree of pigmentation of the exposed skin. For skin routinely exposed to sunlight, the risk estimate is 6.7×10^{-4}/Gy per person-year for a skin area of about 3000 cm^2. For skin not routinely exposed to sunlight, the risk estimate is 2.0×10^{-4}/Gy per person-year for a skin area of about 15,000 cm^2. When all of the skin is exposed to ionizing radiation, the total risk estimate is 8.7×10^{-4}/Gy per person-year [24].

2.1.3 Deterministic Effects of Radiation Exposure to Skin

In the treatment of NMSC's, radiation-induced deterministic effects, also known as harmful tissue reactions, are of more concern than stochastic effects. The existence of a threshold dose characterizes radiation-induced deterministic effects. The threshold dose exists because a critical percentage of the cell population must sustain severe damage

before macroscopic tissue injury is observed. At doses greater than the threshold dose, the severity of harmful tissue reaction increases with increasing dose.

The terminology of the harmful tissue reactions due to radiation exposure was outlined by J. W. Hopewell [25] and was again presented in ICRP Publication 59 [21]. Here, the terminology of radiation-induced skin injury is presented in Table 2.1 and Table 2.2.

Table 2.1. Basic terminology of radiation-induced skin injury. (From ICRP-59)

Effect	Time of Onset	Description
Dry desquamation	3-6 weeks	Atypical keratinization of the skin is due to the reduction in the number of clonogenic cells within the epidermis' basal layer.
Moist desquamation	4-6 weeks	Tissue loss due to the sterilization of a high proportion of clonogenic cells within the epidermis' basal layer.
Secondary ulceration	>6 weeks	Secondary damage to the dermis as a consequence of dehydration and infection when moist desquamation is severe and protracted due to the reproductive sterilization of the vast majority of the clonogenic cells in the irradiated area.
Dermal necrosis	>10 weeks	Necrosis of dermal tissues as a consequence of vascular insufficiency.
Dermal atrophy	>26 weeks	A thinning of the dermal tissue that is associated with the contraction of the previously irradiated area.
Telangiectasia	>52 weeks	An atypical dilatation of the superficial dermal capillaries.
Invasive fibrosis	--	The method of healing associated with acute ulceration, secondary ulceration, and dermal necrosis that leads to scar tissue formation.

Table 2.2. Special case terminology of radiation-induced skin injury. (From ICRP-59)

Effect	Time of Onset	Description
Acute ulceration	<14 days	An early loss of the epidermis and, to a varying degree, dermal tissue that results from the death of fibroblasts and endothelial cells in interphase.
Acute epidermal necrosis	<10 days	Interphase death of post-mitotic keratinocytes in the viable upper layers of the epidermis. This type of lesion may occur with high-dose, low-energy β irradiation.

In 1985, the Radiation Therapy Oncology Group (RTOG) developed the Acute Radiation Morbidity Scoring Criteria. In 1992, the RTOG, in conjunction with the European Organization for Research and Treatment of Cancer (EORTC), published the Late Radiation Morbidity Scoring Scheme. In 1995, the current RTOG Acute Radiation Morbidity Scoring Criteria and the RTOG/EORTC Late Radiation Morbidity Scoring Scheme were published [26] and are shown in Table 2.3 for human skin. Acute (or early, reversible) radiation toxicity typically presents within days or weeks of radiation exposure. Late, irreversible radiation toxicity typically presents after months or years of exposures.

Table 2.3. RTOG/EORTC radiation morbidity scoring criteria for human skin.

Grade	RTOG Acute Toxicity Description	RTOG/EORTC Late Toxicity Description
0	no change over baseline	no change over baseline
1	follicular, faint or dull erythema epilation dry desquamation decreased sweating	slight atrophy pigmentation change some hair loss
2	tender or bright erythema patchy moist desquamation moderate edema	patchy atrophy moderate telangiectasia total hair loss
3	confluent, moist desquamation pitting edema	marked atrophy gross telangiectasia
4	ulceration hemorrhage necrosis	ulceration
5	-	death

Table 2.4. Simplified AJCC (7th Ed.) TNM scale of non-melanoma and non-Merkel cell carcinoma staging.

Stage	Description
0	Carcinoma *in situ*, i.e., confined to the epidermis.
1	No more than 2 cm in diameter, has not metastasized, and has fewer than two high-risk features.
2	Greater than 2 cm in diameter and has not metastasized.
3	The disease has spread to nearby bone or one lymph node less than 3 cm in diameter but has spread to no other organ.
4	The disease has spread to one or more lymph nodes and has spread to bone or other organs.

2.1.4 Skin Cancers

2.1.4.1 Staging

Staging is a quantification of cancer risk by determining the extent that cancer has developed. According to the American Joint Committee on Cancer (AJCC), there are five stages of cutaneous malignancies and are dependent on the Tumor, Node, and Metastasis (TNM) classification grouping criteria. The T-criterion is dependent on the primary tumor thickness and level of ulceration. The N-criterion is dependent on the level of regional lymph node involvement. The M-criterion is dependent on the level of distant metastases [27,28]. Table 2.4 presents simplified descriptions of the clinical stages of NMSC

2.1.4.2 Basal Cell Skin Cancer

Basal cell carcinoma (BCC) originates in the stratum basal layer of the epidermis. Approximately 80% of all NMSC's are BCCs. For this type of cancer, there are no precancerous lesions. Left untreated, they may extend into deeper tissue and possibly infiltrate vital tissues, causing cosmetic deformities or loss of function. Fortunately, BCCs are very rarely life-threatening. Compared with other skin cancer types, BCCs are very low risk for metastasis with a reported metastatic rate of less than 0.1% [29–31]. Those most at risk of developing BCCs are people with a fair complexion and a history of chronic sun exposure.

The National Comprehensive Cancer Network (NCCN®) provides practice guidelines for the workup and treatment of BCCs [32]. The risk of BCC recurrence is categorized as low risk or high risk. After initial treatment, the risk of recurrence depends on various factors such as tumor location, size, depth of infiltration, and histologic subtype [33,34]. If BCCs recur, they typically do so within three years of the initial treatment.

Following the recommendations of the NCCN, the recommended primary treatment of low-risk BCC is curettage and electrodesiccation (C&E), standard surgical excision with 4 mm clinical margins and postoperative margin assessment, or RT for non-surgical candidates. Adjuvant treatment is recommended in cases of positive margin assessment following surgical excision. The recommended adjuvant treatments are Mohs micrographic surgery, re-excision, or RT.

The NCCN recommended primary treatment of high-risk BCC is RT, Mohs micrographic surgery with margin assessment, or standard surgical excision with wide surgical margins and with postoperative margin assessment, with RT reserved only for non-surgical candidates. RT may also be considered for adjuvant treatment if margin assessment is positive, or if margin assessment is negative and there is extensive perineural or large-nerve involvement. For a positive margin assessment following standard surgical excision, Mohs micrographic surgery or re-excision are also possible adjuvant treatments.

2.1.4.3 Squamous Cell Skin Cancer

Cutaneous squamous cell carcinomas (SCC) are skin tumors arising from keratinized epidermal cells that have breached into the skin's dermal layers. Premalignant lesions, such as actinic keratoses, precede the development of SCCs. They most often occur in sun-exposed areas of the body, such as the head, neck, and arms; but may also appear in areas of chronic radiation dermatitis, burn scars, or areas of chronic inflammation. They may involve soft tissue, cartilage, and bone. SCC can cause considerable local destruction

but is rarely metastatic. The risk of lymph node metastasis for patients with one primary SCC is 3.7% and the risk of distant metastatic disease is 0.4% [35].

Generally, SCCs have good prognoses. The 5-year survival rate is ≥90% [36–38]. The reported rate of SCC recurrence in patients who received surgical excision of non-metastatic SCCs was ≤6% with a range of 0% to 16% [39]. A large meta-analysis reported that, following RT, the 5-year recurrence rates were 6.7% for the treatment of primary SCCs and 10% for recurrent SCCs [40]. Other large studies (n>50) reported 5-year cure rates between 90% and 93% and 5-year recurrence rates between 4% and 7% following RT for primary lesions [40-43].

Like BCC, the SCC risk of recurrence and metastasis is categorized as low risk and high risk. The quantities to consider when establishing the risk of SCC include tumor location and size, whether the tumor has a well-defined border, tumor growth rate, degree of differentiation, and tumor depth. Poorly differentiated tumor cells; perineural, lymphatic, or vascular involvement; or tumors located on prior RT sites all constitute a high risk.

The recommended primary treatment of local low-risk SCC is C&E, standard surgical excision with 4-6 mm clinical margins and postoperative margin assessment, or RT. If margin assessment is positive following surgical excision, Mohs micrographic surgery, re-excision, or RT is recommended.

The recommended primary treatment of local high-risk SCC is Mohs micrographic surgery with margin assessment or standard surgical excision with large surgical margins and postoperative margin assessment. For non-surgical candidates, RT or systemic therapy are options. As with BCC, Mohs micrographic surgery, re-excision, and/or RT are standard adjuvant treatments for positive margin assessment cases.

2.1.5 Skin Cancer Treatment Modalities

2.1.5.1 Curettage and electrodesiccation

C&E is a procedure in which a curette is used to scrape away epidermal tumor tissue. After scraping, the area is denatured by electrodesiccation. The process of scraping and denaturing may be repeated two more times. Therefore, this procedure does not allow for histologic margin assessment and is only appropriate for treating non-penetrating superficial lesions. The recurrence rate for BCC is between 91% and 97%. For SCC, the recurrence rate ranges from 0.4% to 19% [45–48].

2.1.5.2 Surgical excision

Surgical excision with postoperative margin assessment is the process of surgically removing the lesion followed by pathologic evaluations of the surgical margin tissues. This procedure is recommended for the treatment of BCC, SCC, and melanomas unless conflicting circumstances exist. The 5-year cure rate following surgical excision is 98% for BCC and 95% for SCC [40,46,49–52].

2.1.5.3 Superficial therapies

Superficial therapies for NMSC include topical therapies, cryosurgery, and photodynamic therapy. Topical therapies involve applying a therapeutic cream, such as imiquimod and 5-fluorouracil cream, directly to the lesion. Cryotherapy involves applying freeze/thaw cycling to destroy target cells. Photodynamic therapy is the process of applying a photosensitizing agent, such as 5-aminolevulinic acid, to a target lesion and exposing it to laser light in the visible light spectrum.

Superficial therapies have been shown to be effective but with cure rates lower than surgery. For example, a randomized controlled trial comparing surgical excision vs. imiquimod 5% cream for BCC treatment found that the 3-year disease rates were 84% for

imiquimod and 98% for surgery. Cosmetic outcomes, however, were significantly better with imiquimod (61%) than with surgery (36%) [53].

2.1.5.4 Radiation therapy

In general, conformal RT is the process of exposing diseased tissue – while minimizing exposure to healthy tissue – with ionizing radiation. Treating with external high energy photon or electron beam radiation produced by a clinical linear particle accelerator (linac) is a mainstay of most radiation therapy clinics. Treating small skin cancer lesions with radiation produced by a linac is difficult because of the deep penetration of the high energy photons or the dose calculation uncertainties for small electron fields.

Brachytherapy (BT) – derived from the Greek word "brachys", meaning "short-distance" – involves placing a radiation source in, on, or near a target lesion. Intracavitary brachytherapy involves placing radiation sources in a natural cavity of the body, such as the trachea, vagina, or rectum. Interstitial brachytherapy involves surgically implanting radiation sources directly into or near a tumor. Superficial brachytherapy (also called surface or contact brachytherapy) involves placing a radioactive source directly on or a short distance away from the surface of a target lesion. Historically, superficial brachytherapy was performed only with radioisotopes, but with the advent of the miniature x-ray source, superficial electronic brachytherapy became possible. Electronic brachytherapy sources can also be used for intracavitary and interstitial brachytherapy.

Many factors may lead to RT being chosen as the primary treatment option, such as patient age and performance score. To minimize risks associated with deterministic effects of radiation exposure, RT may be reserved for patients older than 60 years. Performance scoring is a method of quantitatively assessing a patient's well-being by gauging their ability for self-care and levels of function and ambulation. Table 2.5 and Table 2.6 show the Karnofsky and ECOG performance status scales, respectively. RT has

Table 2.5. Karnofsky performance status

Stage	Description
100	Normal
90	Only minor signs or symptoms of disease
80	Able to perform normal activities with some effort, some signs of disease
70	Capable of self-care; incapable of
60	Capable of most self-care; requires occasional assistance
50	Requires considerable assistance and frequent medical care
40	Disabled; requires special assistance and care
30	Severely disabled; hospitalization is indicated; death not imminent
20	Very ill; requires hospitalization and active care
10	Moribund;
0	Dead

Table 2.6. ECOG performance status

Stage	Status Description
0	Fully active; normal
1	Restricted in physically strenuous activity; able to perform work of a light or sedentary nature
2	Ambulatory but unable to perform any work activities; out of bed more than 50% of waking hours
3	Capable of limited self-care; confined to bed more than 50% of waking hours
4	Completely disabled; confined to bed or chair all hours
5	Dead

been shown to be an effective option for treating SCC and BCC. The cure rates for BT are over 90% for most skin lesions [49].

2.2 Contemporary Superficial Brachytherapy Applicators

2.2.1 HDR Surface Brachytherapy Applicators

HDR surface brachytherapy applicators are small, cone-shaped applicators used in tandem with high-dose-rate (HDR) afterloader machines. Commercially available

applicators are sold as sets in a range of fixed inner diameters and with a source dwell position at the vertex of the cone, aligning the HDR seed either perpendicular or parallel to the lesion surface. The applicators are made from high Z materials (e.g., tungsten), which shields the healthy tissue outside the treatment area. A plastic end cap attaches to the applicator's treatment face, which reduces skin surface dose from electron contamination. The two most common applicators are the Varian (Varian Medical Systems, Palo Alto, CA, USA) and Elekta Leipzig-style applicators [54–57] and the Elekta Valencia applicator (Elekta AB-Nucletron, Stockholm, Sweden) [55,58–60].

The Varian Leipzig-style applicator comes as a single cone-shaped surface applicator that receives one of four fixed diameter insets with diameters of 30 mm, 35 mm, 40 mm, and 45 mm. The source transportation tube is parallel to the treatment surface. Varian also provides surface applicators that are equivalent to the parallel source Leipzig-style applicator except that the distal end source transportation tube is perpendicular to the treatment surface rather than parallel. Two cone-shaped surface applicators are available – a smaller diameter applicator and a larger diameter applicator. The larger diameter applicator receives the same fixed diameter insets as the Leipzig-style applicator as well as a 30 mm × 20 mm oval inset, or a 45 mm × 25 mm oval inset. The small diameter applicator receives one of three fixed diameter insets with diameters of 15 mm, 20 mm, and 25 mm.

The Elekta surface brachytherapy applicators are available with fixed diameters of 10 mm, 20 mm, and 30 mm with parallel (Elekta H-type) and perpendicular (Elekta V-type) source orientation configurations. Elekta also provides the Valencia applicator, which has a flattening filter built into the treatment cap, improving flatness and homogeneity of the isodose distribution compared to Leipzig-style applicators. Treatment planning may be performed with Elekta's Oncertra Brachy treatment planning software; however, dose distribution charts are only available for Ir^{192} HDR seeds.

The strength of HDR brachytherapy sources should be determined by the National Institute of Standards and Technology (NIST) or an Accredited Dosimetry Calibration Laboratory (ADCL). Source output verification for HDR surface brachytherapy applicators may be performed by a combination of Monte Carlo (MC) calculations, thermoluminescent dosimeter (TLD) measurements, and film dosimeter measurements [61].

Alternatively, Standard Imaging (Deming Way, Middleton, W) supplies a Leipzig-type applicator holder to be used in conjunction with the HRD 1000 Plus or IVB 1000 well chambers [62,63]. Given the inherent size and shape of HDR brachytherapy surface applicators, appropriately placing the applicators inside a well chamber is impossible. To circumvent the applicator geometry issue, the applicator may be placed at the entrance of the well chamber via the aforementioned applicator holder. After accounting for atmospheric conditions and the well chamber calibration factor, the correspondence factor is calculated by taking the ratio of the corrected reading to the air kerma strength of the HDR source. The correspondence factor is then compared to a table of published correspondence factors. Standard Imaging recommends that the calculated correspondence factor is within ±5% of the corresponding published table value.

2.2.2 Electronic Source Brachytherapy

In the early to mid-1990s, a miniaturized x-ray source was developed for use in surface and interstitial brachytherapy procedures [64]. An early version of an electronic interstitial radiosurgery x-ray source was composed of a miniature electron gun with a barium oxide thermionic cathode. Electron intensity was controlled by manipulating the cathode filament current. Thermionically emitted electrons were accelerated by the positively charged cathode and then focused and further accelerated to their final energy by a triad of anodes. A drift tube was attached to the electron gun, through which the accelerated electrons traveled before striking a thin gold (Au) target set within a beryllium

window. Magnetic shielding and beam deflectors were placed around the drift tube to allow the electrons' trajectory to be controlled, albeit minutely. The treatment end of the device had an outer diameter of 3 mm.

Examples of modern electronic brachytherapy (eBT) machines include the Zeiss Intrabeam (Carl Zeiss Surgical, Oberkochen, Germany), iCAD Xoft (iCAD Inc., Nashua, NH, USA), Ariane Papillon (Ariane Medical Systems, Alfreton, England), Xstrahl Photoelectric Therapy (Xstrahl, Surrey, England), Elekta Esteya (Elekta AB-Nucletron, Stockholm, Sweden), and Sensus Healthcare SRT 100 (Sensus Healthcare, Boca Raton, FL, USA). These machines typically operate between 50 and 100 kVp [65,66]. In general, eBT systems' strengths include that they have no radiation leakage when in the off-state and have a user-adjustable dose rate. They also have standard non-customizable source sizes and applicators, which limits dose conformity.

The Xoft Axxent eBT system uses a small 23 mm long by 2.25 mm diameter proprietary X-ray source with a multi-lumen catheter. Similar to an HDR source, the Axxent source may be stepped through the length of a catheter. It may be used to treat early-stage breast cancer, gynecological malignancies, and, with the addition of a Xoft Axxent surface applicator, skin cancer [67,68]. The Axxent system has a limited lifetime of about 3 hours or 10 treatments [69]. The surface applicators are cone-shaped collimators ranging from 10 mm to 50 mm in diameter.

The Zeiss Intrabeam system is a mobile X-ray source system. To produce x-rays, electrons are accelerated down a drift tube, striking an Au target at the distal end of a target tube. Four applicator types are available: a spherical applicator for intracavitary intraoperative eBT, a flat applicator to treat surgically exposed surfaces, a needle applicator for interstitial irradiation, and a surface applicator for treatment of superficial lesions. The surface applicators range in size from 10 to 60 mm in diameter. The Zeiss flat and surface applicators consist of a 0.05 mm lead-equivalent shielding tube and a flattening filter [70].

The Esteya [71], Photoelectric Therapy [72], and SRT 100 [73] systems were uniquely designed for the treatment of superficial skin lesions. Each system uses a collimated source with applicators ranging from 10 to 50 mm in diameter and accelerating potentials ranging from 50 kVp to 80 kVp. Typical treatment times are 1-2 minutes [65,69].

2.2.3 Molds and Radioactive Patches

Another option for radiotherapeutic treatment of skin lesions is to create 3D printed HDR molds or radioactive patches. These devices are highly customizable and are made specifically for each target lesion. Mold-type applicators are formed directly to the patient's surface and, with the aid of an HDR treatment planning system, source catheters are inlaid in poly(methyl methacrylate) (PMMA) or another clinically appropriate material [74–76]. Radioactive bandages or patches are typically constructed in-house. Some beta-minus emitting sources that have been studied are holmium-166 (^{166}Ho), rhenium-188 (^{188}Re), strontium-90 (^{90}Sr), yttrium-90 (^{90}Y), and phosphorus-32 (^{32}P) [78-81].

2.2.4 Strontium Probe

Strontium probe therapy involves topically applying a ^{90}Sr source to a target region. The ^{90}Sr is located on the distal end of a shielded rod, which the medical professional holds in place during the treatment. ^{90}Sr has been used to successfully treat SCC in dogs and cats. In one retrospective study, ^{90}Sr was used to treat nasal planum SCC in 15 cats. Excellent cosmetic results were achieved, and 13 of the 15 cats achieved complete response with a median disease-free interval of 692 days [81]. In a retrospective study of 49 cats with SCC of the nasal planum treated with ^{90}Sr plesiotherapy yielded, 88% of the cats had a complete response, and 20% of the cats experienced recurring SCC. The researchers found that the overall survival time was significantly longer for cats with a complete response to treatment than those with a partial response [82]. Berlato et al. [83] aimed to determine the efficacy of a fractionated protocol versus a single-dose protocol of ^{90}St plesiotherapy. In their study,

74 cats with SCC of the nasal planum were included with 32 treated with a fractionated protocol and the remaining 42 were treated with a single-dose protocol. They found that ^{90}Sr plesiotherapy induced a complete response in 74% of the cats, with 17% of the cats experiencing local recurrence. They also found that the disease-free interval for cats treated with the fractionated protocol was significantly longer than for the cats treated with the single-dose protocol. Response and overall survival were not statistically significant for fractionated versus single-dose protocols.

In a case series of canine third eyelid SCC in which nine dogs were treated with ^{90}Sr, seven of the dogs were disease-free for 1,239 to 2,555 days [84]. Two dogs required surgical treatment for local tumor recurrence within one year [84]. Notably, no occurrence of radiation-induced cataracts was reported, illustrating its tolerability even when near critical structures.

Strontium-90 (^{90}Sr) is the parent isotope of yttrium-90 (^{90}Y) and has an average decay energy of 196 keV and a half-life of 28.5 years. Secular equilibrium is reached in approximately seven ^{90}Y half-lives. ^{90}Y is the therapeutic component of ^{90}Sr.

2.3 Therapeutic Electrons and their Interactions with Matter

The most prevalent theory of how ionizing radiation damages living human tissue is that, through direct or indirect processes, enough energy is transferred to cellular deoxyribonucleic acid (DNA) to cause single- or double-strand breaks of the DNA sugar-phosphate backbone. The creation of DNA strand breaks may ultimately lead to chromosomal aberrations and mitotic catastrophe, resulting in cell death.

Therapeutic electrons are directly ionizing particles and interact with atomic matter through Coulombic interactions with bound atomic electrons and atomic nuclei. There are two manners in which a high-energy charged particle may lose energy as it interacts with matter – collisional interactions and radiative interactions. The linear stopping power (S)

is the rate of energy loss per unit distance (*-dE/dx*) due to these interactions and is expressed mathematically as:

$$S = -\frac{dE}{dx} = -\left(\frac{dE}{dx}\right)_{col} - \left(\frac{dE}{dx}\right)_{rad} \tag{2.1}$$

Radiative interactions occur when a charged particle interacts with the nucleus of a nearby atom. The pull of an atomic nucleus will cause a charged particle to experience an accelerating force and release a bremsstrahlung (braking radiation) photon at any point along its track. The specific energy loss through the radiative process is inversely proportional to the squared rest mass (m_0^2) of the particle and proportional to the squared atomic number (Z^2). The implication is that the probability bremsstrahlung is very small for charged particles more massive than the electron and quickly increases with increasing particle energy.

Collisional interactions occur when a charged particle interacts with an atomic electron cloud and result in atomic ionization, excitation, or distortion. A charged particle with kinetic energy greater than the binding energy of an atomic electron can ionize an atom, liberating a secondary electron – known as a δ-ray or knock-on electron – that potentially has enough kinetic energy to cause additional collisional or radiative interaction events in the medium. Excitation occurs when the incident charged particle imparts just enough energy to promote an atomic electron but not liberate it, making the atom unstable. Following excitation, the atom will decay with some half-life ($t_{1/2}$) and emit a characteristic x-ray. Ionization and excitation require that the distance between the path of the incident charged particle and the atom be relatively small – approximately equal to one Bohr radius. Ionization typically occurs when the incident particle is closer to the atom than the distance for atomic excitation.

Atomic distortion occurs when the charged particle's path is relatively far from the atom and the charged particle distorts the electron clouds of atoms in the medium. When the medium is dielectric and the charged particle's velocity is greater than the speed of light in the medium through which it is traversing, visible light will be emitted. This visible light is known as Cerenkov radiation.

2.4 Beta-Minus Nuclear Decay

Ernest Rutherford is credited with first identifying the process of beta-minus (β^-) decay in 1899. In 1900, after J.J. Thompson discovered the electron, Henri Becquerel suggested that the β^- particle was simply a fast-moving electron. In 1934, Irène and Frédéric Joliot-Curie first observed positron emissions through beta-plus (β^+) decay. Also in 1934, Gian-Carlo Wick first proposed the process of electron capture, which was further discussed by Hideki Yukawa and was observed by Luis Alvarez in 1937. Each process (β^- decay, β^+ decay, and electron capture) is explained by Enrico Fermi's theory of beta decay, which was a precursor to the theory of weak nuclear force interaction – or electroweak theory (EWT). The three processes involve neutrons (n), protons (p), electrons (β^-), positrons (β^+), neutrinos (ν), and antineutrinos ($\bar{\nu}$) – described mathematically as:

$$n \rightarrow p + \beta^- + \bar{\nu} \qquad \text{(beta-minus decay)} \tag{2.2}$$

$$\text{p} \rightarrow n + \beta^+ + \nu \qquad \text{(beta-plus decay)} \tag{2.3}$$

$$p + \beta^- \rightarrow n + \nu \qquad \text{(electron capture)} \tag{2.4}$$

A neutron is composed of one up and two down quarks, and a proton is composed of two up quarks and one down quark. In neutron-rich atomic nuclei, one of the neutron down quarks can transmute to an up quark, releasing an intermediate W^- boson which immediately decays into a β^- and $\bar{\nu}$. When this occurs, the nuclear conservation laws are

obeyed, and energy released (Q) is shared as kinetic energy of the β^- and the $\bar{\nu}$. This is the beta-minus decay process.

Nuclear decay events follow Poisson statistics, meaning that each decay event is an independent and random event with a constant probability of occurrence for each particular decay process. The probability of a decay event occurring per unit time is termed the decay constant (λ). For a sample of N unstable atoms, the time rate change in the number of atoms, which is the activity (A), is equal to the product of N with a probability of a decay event occurring per unit time times the number of unstable atoms:

$$A = {}^{dN}/_{dt} = -\lambda N \tag{2.5}$$

The solution to this differential equation yields the number of unstable atoms after time t where N_0 is the number of unstable atoms at $t = 0$ and is expressed as:

$$N(t) = N_0 e^{-\lambda t} \tag{2.6}$$

or, in terms of activity as:

$$A(t) = A_0 e^{-\lambda t} \tag{2.7}$$

It is often convenient to express λ in terms of the decay half-life ($t_{1/2}$), which is the amount of time required for N to decrease by half and is given by:

$$t_{1/2} = {}^{\ln(2)}/_{\lambda} \tag{2.8}$$

From Equations 2.7 and 2.8, activity in terms of half-life is:

$$A(t) = A_0 e^{\frac{-ln(2)t}{t_{1/2}}} \tag{2.9}$$

The Radiation Therapy Committee Task Group No. 60 (TG60) of the American Association of Physicists in Medicine (AAPM) published a report regarding the physics of

Table 2.7. Properties of five neutron activated beta emitters. Some of the nuclides may be obtained by means other than by neutron activation.

Isotope	Half-Life	Decay Mode	Maximum Beta Energy	Mean Beta Energy	CSDA Range in Water	Daughter Nucleus
		(%)	(keV)	(keV)	(cm)	
^{32}P	14.27 d	100	1711	695.03	0.8215	^{32}S
^{90}Y	64.04 h	100	2280	933.6	1.129	^{90}Zr
^{106}Rh	30.07 s	100	3541	1410	1.795	^{106}Pd
^{142}Pr	19.12 h	99.9836	2162	810	1.065	^{142}Nd
^{188}Re	17.00 h	100	2120	763	1.0424	^{188}Os

intravascular brachytherapy (IVBT) [85]. While TG60 does not focus specifically on beta-emitting sources used in intravascular brachytherapy, it does provide a list of five therapeutic beta-emitting radionuclides, namely: phosphorus-32 (^{32}P), yttrium-90 (^{90}Y), strontium-90 (^{90}Sr), rhodium-106 (^{106}Rh), and rhenium-188 (^{188}Re) (Table 2.7).

Even though each isotope decays by beta minus emission essentially 100% of the time, each of them other than ^{32}P occasionally decays to an excited state of the daughter atom. The resulting excited atoms then relax, releasing an isomeric transition gamma (more probable) or an internal conversion electron (less probable).

The radionuclide ^{90}Y is the subject of this research and decays purely by beta-minus decay, with a Q of 2.2801 MeV, an average β^- energy of 0.9267 MeV, a continuous slowing down approximation range (R_{CSDA}) of 1.129 g·cm^{-2}, and a half-life of 2.6684 days (64.0414 hours). It decays 99.98% of the time to the stable state of zirconium-90 (^{90}Zr). The remaining 0.02% of the time it decays by beta-minus decay to the excited 2^+ (1.4×10^{-6} %) or 0^+ (0.0115%) state of ^{90}Zr and subsequently decays to the ground state by two-photon de-excitation, internal pair-production, or internal conversion.

Figure 2.2 shows the ^{90}Y beta minus decay scheme. ^{90}Y decays to the ground state of ^{90}Zr by three possible paths of decay. By convention, beta minus decay is indicated by the arrow pointing down and right. Beta plus decay has an arrow pointing down and left.

The vertical blue arrows between the excited states and the ground state represent the difference in energy of those states, and therefore the amount of energy (in keV) released as the excited nucleus relaxes.

As discussed in section 2.3, bremsstrahlung photons result from the conservation of momentum of charged particles undergoing inelastic collisions with atomic nuclei. For an incident β^-, the rate of bremsstrahlung production is roughly proportional to the Z^2. Therefore, the primary shielding of β- particles should be composed of low-Z materials to minimize bremsstrahlung photon production. This material does not need to be exceedingly thick because of the short-range of β^- particles, so long as its thickness is greater than the maximum range of β^- particles in that material. A high-Z material can then be placed on the low-Z material's external surface to shield against any ancillary high-energy photons.

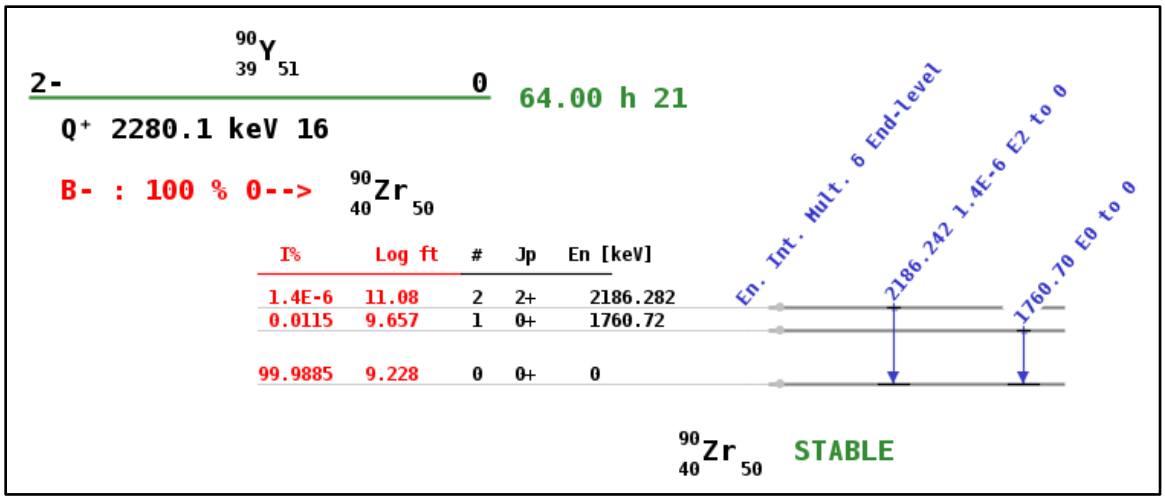

Figure 2.2. Decay diagram for ^{90}Y. (Figure from iaea.org)

2.5 ^{90}Y Production

^{90}Y is produced by fast neutron activation or slow neutron activation. It is also a nuclear fission product and can be obtained from a ^{90}Sr/^{90}Y generator. The ^{90}Y used for the work presented in this document was produced from yttrium-89 (^{89}Y) by slow neutron activation at the Missouri University Research Reactor (MURR) (Columbia, MO, USA).

For neutron activation, depending on the material being bombarded, several neutron interactions may occur (e.g., neutron-gamma, neutron-proton, neutron-alpha, or neutron-neutron). The dominant interaction for the activation of β^- emitters is the neutron-gamma (n, γ) reaction, which is expressed as:

$$ {}^{A}_{Z}X(n,\gamma){}^{A+1}_{Z}X \tag{2.10} $$

or

$$ n + {}^{A}_{Z}X \rightarrow {}^{A+1}_{Z}X^{*} \rightarrow {}^{A+1}_{Z}X + \gamma \tag{2.11} $$

When the target atom (X) captures a neutron, its mass number (A) and neutron number increase by one, and it is briefly left in an excited state (X*). It quickly relaxes by prompt γ-ray emission.

If a target of N_0 atoms is bombarded with a constant neutron fluence (ϕ) of n cm^{-2} sec^{-1} and the probability of interaction is σ, then, accounting for the decay of the daughter atoms ($-\lambda N$), the production rate of daughter atoms (N) is

$$ {dN}/{dt} = \phi\sigma N_0 - \lambda N \tag{2.12} $$

The solution to the differential equation 2.12 is the simplified neutron activation equation:

$$ N(t) = \frac{\phi\sigma N_0}{\lambda}\left(1 - e^{-\lambda t}\right) \tag{2.13} $$

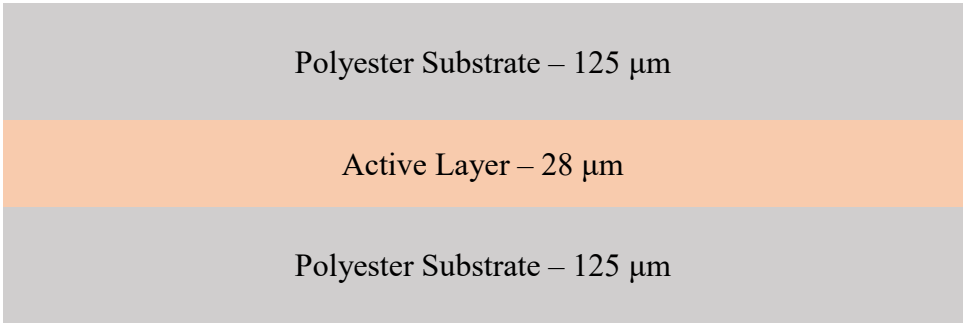

Figure 2.3. Radiochromic EBT3 film layer structure.

In terms of activity, the neutron activation equation is:

$$A(t) = \phi\sigma A_0\left(1 - e^{-\lambda t}\right) \tag{2.14}$$

The maximum possible activity, termed the saturation activity, occurs when *t* approached infinity, and the exponential of Equation 2.13 approaches zero and is expressed as:

$$A(t) \cong \phi\sigma N_0 \qquad \text{(for large } t\text{)} \tag{2.15}$$

2.6 Dose Measurement and Calculation

2.6.1 Radiochromic Film Dosimetry

Film-based dosimetry is a convenient and powerful tool often used in RT treatment verification and quality assurance (QA). The high resolution offered by film dosimeters is particularly useful when the measurement of high dose gradients is needed. GAFChromic™ EBT3 radiochromic film (International Specialty Products, Wayne, NJ) is highly energy independent and has an ideal dose range of 0.2-10 Gy but is suitable for a range of 0.1-20 Gy. Sandwiched between two matte-polyester layers, the active layer comprises the lithium salt of pentacosa-10,12-diynoic acid (LiPCDA) monomers (Figure 2.3). The LiPCDA monomers can absorb energy and polymerize to form linear long-chained polymer (polyPCDA). The backbone of polyPCDA absorbs light, increasing the film's opacity with increasing absorbed dose [86].

To read the film, International Specialty Produces recommends that the film be scanned with am EPSON Expression 11000XL or 10000XL (Seiko Epson Corporation, Suwa, Nagano Prefecture, Japan) 48-bit (16 bit per color channel) high-resolution photo scanner yielding digitized images in red-green-blue (RGB) format. Historically, only a single color channel was used for analysis. The red channel is most often used because it provides the greatest sensitivity in the clinical dose range (<10 Gy). Above 10 Gy, the green channel is more sensitive to differences in absorbed dose and is used to increase the dynamic range of EBT3 film.

Challenges in radiochromic film dosimetry include accounting for uncertainties caused by dose-independent perturbations that appear in the digitized film image. These characteristics include sensitivity to scanner orientation, postirradiation coloration, film handling effects, and scanner lateral response artifacts. Fortunately, these characteristics have been previously investigated [87–89]. Micke et al. developed a triple-channel dosimetry technique that corrects for non-uniformities in the digitized film image [90]. This method allows for separation and removal of the film image's dose-independent components, resulting in an image that is only dependent on absorbed dose.

The triple-channel dosimetry method has been shown to be superior to single-channel dosimetry in that it compensates for film thickness nonuniformities, increases the signal to noise levels, mitigates lateral response artifacts, and extends the evaluable dose range. However, multi-channel dosimetry can be complex and difficult to implement. Further, steps can be taken to lessen uncertainties in single-channel dosimetry. Single-channel dosimetry was used for this work and is discussed further in section 3.2.1.

The dose-dependent change in the opacity of EBT3 film may be characterized by the net optical density (*netOD*) and is related to the intensity of light transmitted through an unexposed film (I_0) and the intensity of light transmitted through the exposed film (I) by the Lambert-Beer law:

$$netOD = -log\left(\frac{I}{I_0}\right) \tag{2.16}$$

To relate $netOD$ to dose (D), it is recommended that the calibration function has the form:

$$netOD = a + b/(D - c) \tag{2.17}$$

where a, b, and c are fitting parameters [91]. Unknown film dose as a function of $netOD$ can be found by inverting Equation 2.17:

$$D = c + b/(netOD - a) \tag{2.18}$$

2.6.2 Monte Carlo Radiation Transport Simulation

Monte Carlo (MC) simulation of a variable embedded in a stochastic model – as in particle transport – is simply a numerical computation of the expected value of a quantity that represents a real event. The MC technique requires *a priori* information, such as the probability distributions that govern particles' interactions with matter, to simulate the random trajectories and energy loss of individual particles. Randomly sampling the probability distributions and recording the resulting quantities of interest for many iterations yields a distribution of values whose mean value represents the true physical quantity within some statistical uncertainty range.

The most fundamental form of MC radiation transport simulation is called *analog* and is the one-to-one simulation of real physics processes [92]. The transport process can be broken down into five distinct steps. The first step is to determine the particle's initial position and energy by randomly sampling the specified particle decay spectrum and source geometry. The second step is to determine the length to the next point of interaction. The third step is to ray trace the particle to the next interaction location while accounting for the features of the phase space (e.g., the materials compositions, boundaries, mass densities, etc.). The fourth step is to determine the type of interaction that occurs at the new

location. The final step is to determine the consequences of the interaction based on a random sampling of the interaction type's differential cross-sections. The generation of secondary particles is possible, depending on the energies and interactions that are simulated. Steps 2-5 are repeated until the primary and secondary particles fall below specified energy thresholds or exit the phase space. The completion of this five-step process is known as a "history".

The Monte Carlo process is highly dependent on the generation of random numbers to randomly sample the probability distributions – commonly called the cross-sections – to determine the series of events that a simulated particle experience. Suppose that there is a random number ξ such that $0 \leq \xi < 1$ and a probability density function $p(x)$ that governs the mutually exclusive outcome of an event E_n. The sum of probabilities on the interval a$\leq x <$b for an event E_n is equal to one:

$$\int_a^b p(x)dx = 1 \tag{2.19}$$

The variable x can then be uniquely related to ξ through the probability distribution function $P(x)$.

$$\xi = P(x) = \int_a^x p(x')dx' \tag{2.20}$$

Determining the distance between interactions for step number two is relatively straight forward. Consider the following example. The linear attenuation coefficient (μ) describes the number of interactions a particle experiences per unit length in a medium. For a traveling particle, the probability of collision $p(r)$, (Figure 2.4.a), between *r* and *r*+*dr* is

$$p(r)dr = e^{-\mu r}\mu dr \tag{2.21}$$

From Equation 2.20, the cumulative probability distribution $P(r)$ (Figure 2.4.b) is

$$P(r) = \int_0^r e^{-\mu r'} \mu dr' \tag{2.22}$$

It follows that

$$\xi = P(r) = 1 - e^{-\mu r} \tag{2.23}$$

By rearranging, we can solve for r in terms of ξ.

$$r = -\ln(1 - \xi) / \mu \tag{2.24}$$

The variable r is the distance from the initial location of a simulated particle to the particle's next point of interaction. Additional similar operations are performed to determine the direction the particle travels and what interaction occurs at the next interaction point.

Even though many relevant probability distributions are continuous functions, such as that of Equation 2.21, many relevant probability distributions are discontinuous. The same procedure is performed to relate the target variable to a uniformly distributed random variable between zero and one. The discrete summation of continuous probability density functions is sometimes advantageous.

MC techniques in which non-physical assumptions are made, meaning they are not strictly equivalent to reality, are called *non-analog*. The purpose of *non-analog* MC simulation is to reduce computer time and, thus, reduce the length of time needed to produce statistically significant results. Consider an isotropic particle source far enough from a detector that the particles incident on the detector may be treated as traveling parallel to one another. In a simulation, we may define the source to emit particles in only the

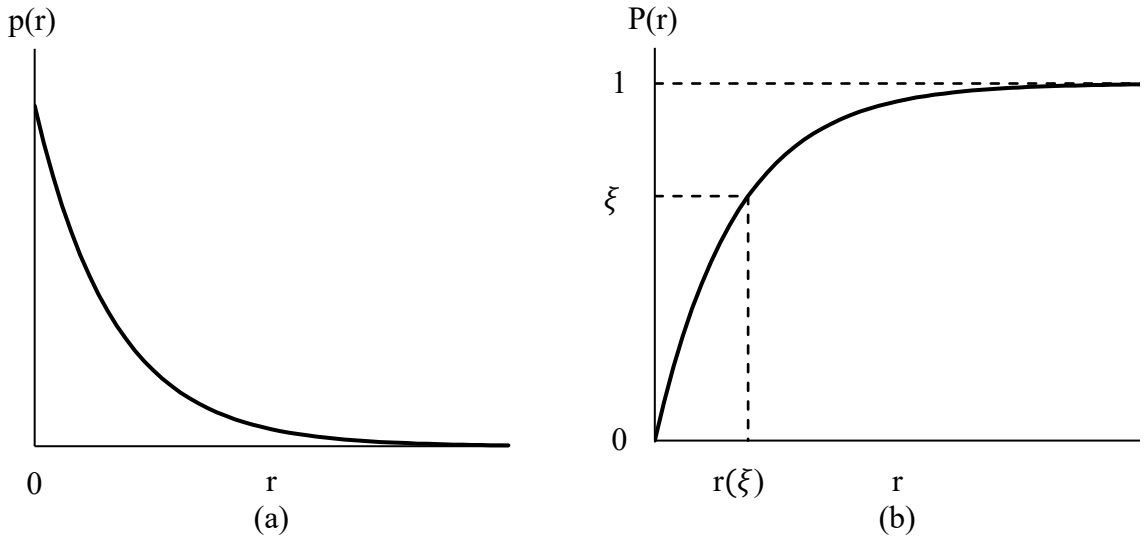

Figure 2.4. (a) Probability density function. (b) Continuous probability distribution.

detector's direction and omit particles that would not have interacted with the detector. This action would significantly reduce the number of calculations because it avoids unnecessary transport calculation. The quantity of interest could then be related to the realistic activity of the source by scaling the calculated quantity by the ratio of the solid angle between the exposed area of the detector and the source over 4π steradians; which can be approximated by the ratio of the area of the detector exposed to the source and the area of a sphere with a radius equal to the distance between the source and the detector.

2.6.3 Analytical Methods for Determination of β^- Source Dose Rates

Beta ray dosimetry calculation methods based on R_{CSDA} provide a quick and accurate means of approximating dose from β^- particles to various materials. The methodology presented in this section is based on the work of Cross et al. [22,93] and Deufel et al. [94], which are both extensions of work by Loevinger et al. [95].

Deufel et al. provide a useful and descriptive derivation of the absorbed dose rate ($\dot{D}$) to water as a function of the distance (r) in a heterogeneous medium by β^- particles, for a point source yielding:

$$\dot{D}_{in\ medium}^{to\ water}(r) = Activity\ * f\left(Z_{eff}, r\right)\frac{K_{water}(r_{rad})}{r^2} \tag{2.25}$$

and for a finite source:

$$\dot{D}_{in\ medium}^{to\ water}(r) = Activiy * f\left(Z_{eff}, r\right)\sum_{sources,i}^{N}\frac{K_{water}(r_{rad,i})}{r^2} \tag{2.26}$$

The function $f\left(Z_{eff}, r\right)$ is a medium-specific scaling factor. The factor K_{water} is an expression presented by Cross, which used MC simulated results to incorporate empirical parameters in the calculations.

$$K_{water} = \frac{k}{\nu^2}\begin{cases} U + V & r_{rad} \leq \mathrm{C}/\nu, \\ V & \mathrm{C}/\nu < r_{rad} < R, \\ 0 & r \geq R \end{cases} \tag{2.27}$$

where

$$U = C - \nu r_{rad}e^{\left(1-\frac{\nu r_{rad}}{C}\right)} \tag{2.28}$$

$$V = \nu r_{rad}e^{(1-\nu r_{rad})} - A \tag{2.29}$$

$$A = \nu R e^{(1-\nu R)} \tag{2.30}$$

The source-specific DPK parameters R, ν, C, and k were obtained by Cross and are based on data from ICRU-56 [22]. The parameter R is a function of R_{CSDA}, which closely approximates the average path length of charged particles emitted from sources that emit a range of particle energies. In this case, R is the point at which the function goes to zero and is approximately $0.74R_{max}$ for each radionuclide. Conservation of energy requires that the total energy per disintegration absorbed in an infinite medium is equal to the average

energy released by a radioactive source. Parameter k acts as a normalization factor that holds the function to the energy conservation requirement.

The effective atomic number (Z_{eff}) of the medium in which the dose rate is being calculated determines the probability of electron scattering versus energy loss. For a 2-dimensional source with an infinite area, the absorbed dose at depth d is proportional to the absorbed dose to water at depth $\eta \times d$ where η is a correction factor. This scaling factor is proportional to $f(Z_{eff}) \times dE/dz$. For various materials, $f(Z_{eff})$ is found by comparing dose distributions in various media and comparing those to dose distributions in water and dividing them by mass stopping powers relative to water and then plotting versus Z_{eff}. ICRU-56 provides a formula to calculate $f(Z_{eff})$ and Cross et al. have provided values for various materials.

The radiological distance, (r_{rad},) is the water equivalent depth in a non-water material and is given by:

$$r_{rad} = \sum_{materials,j} \eta_j \left(\frac{\rho_m}{\rho_w}\right) \Delta r_j \tag{2.31}$$

where η_j is the radiological scaling factor for material j, and Δr_j is the length of a straight line (r) that joins the source point and the field point that passes through material j. Following the work of Deufel et al., for a point source located at $S = (x_s, y_s, z_s)$ and a reference point located at $P = (x_p, y_p, z_p)$ and a point at (x_i, y_i, z_i) that lays on line r at the intersection of materials j and j+1:

$$\Delta r_j = \sqrt{(x_i - x_s)^2 + (y_i - y_s)^2 + (z_i - z_s)^2} \tag{2.32}$$

and

$$x_i = x_s + \left(x_p - x_s\right) \frac{(z_j - z_s)}{(z_p - z_s)} \tag{2.33}$$

$$y_i = y_s + (y_p - y_s)\frac{(z_j - z_s)}{(z_p - z_s)} \tag{2.34}$$

$$z_i = z_j \tag{2.35}$$

Chapter 3

METHODOLOGY

3.1 The Conformal Superficial Brachytherapy Applicator

The CSBT prototype (Figure 3.1) was designed in SolidWorks 2017 (Dassault Systèmes, Vélizy-Villacoublay, France) and was 3D printed with a desktop 3D printer (CR-10, Creality, Shenzhen, China) using PLA filament as previously described in the literature [17]. The device holds up to 19 sources in a hexagonal arrangement (Figure 3.2) with each source affixed to the distal end of a tungsten carbide rod housed within a 3D printed aperture.

Because of its relatively high energy, short half-life, and accessibility, ^{90}Y was selected to be the radiation source for the CSBT device. The ^{89}Y neutron capture cross-section is large enough to allow for activation into ^{90}Y in a nuclear reactor, making ^{90}Y very accessible. Its half-life is long enough to allow for shipping, planning, and treatment; and is short enough to not create a radioactive waste nuisance. Because it is a pure beta emitter, it is easily shielded when not in use, and its dose is deposited in a relatively short range, thus sparing deeper normal tissue. It has the additional advantage of having been

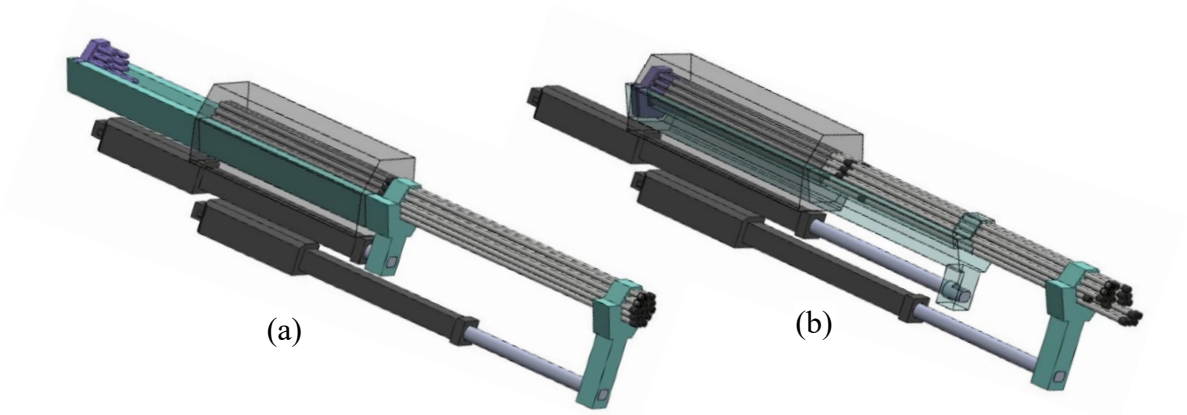

Figure 3.1. Drawing of the Conformal Superficial Brachytherapy Device (CSBT). (a) CSBT in its initial position. The patient-specific 3D printed insert is placed in the proximal end of the carriage tray. (b) CSBT in its treatment position. The upper actuator is in its forward position, bringing the 3D printed insert into the rod channels and moving the rods to their treatment positions

previously used as the therapeutic component of strontium-90 (^{90}Sr) based therapies and is well understood.

The sources were secured to the rods by custom made 3D printed source holder tips. The source holder tips (Figure 3.4) were 3D printed by stereolithography (Form 2 SLA, Formlabs, Somerville, MA, USA). The procedure of securing a source to the CSBT

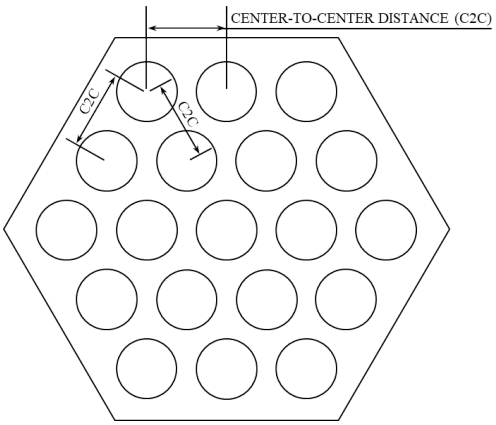

Figure 3.2. The transverse cross-sectional view of the rod holder. The rods, and therefore the tips and sources, are arranged in a hexagonal arrangement and have a center-to-center distance (C2C) of 0.45 cm.

device involved dropping a source in the proximal end of a 3D printed tip and then inserting the distal end of a rod into the proximal end of the tip. Within the tip's interior, there was a small taper to assist in orienting the source and a small lip to prevent the source from falling out of the distal end of the tip. The tips fit by interference on the distal ends of the rods.

The CSBT device had two linear actuators – an upper actuator and a lower actuator. The upper actuator drove a carriage, the proximal end of which housed a target-specific 3D printed "rod pusher" insert (Figure 3.5). When in the "home" position, the actuator was fully retracted, allowing the rod pusher to be placed in the carriage. When the upper

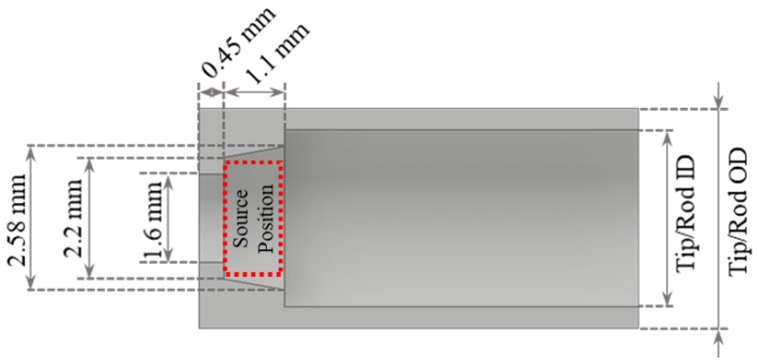

Figure 3.4. Drawing of the 3D printed rod tip. Each tip is placed on a rod and is held in place via interference. The source is located within a tapered cavity at the distal end of the tip.

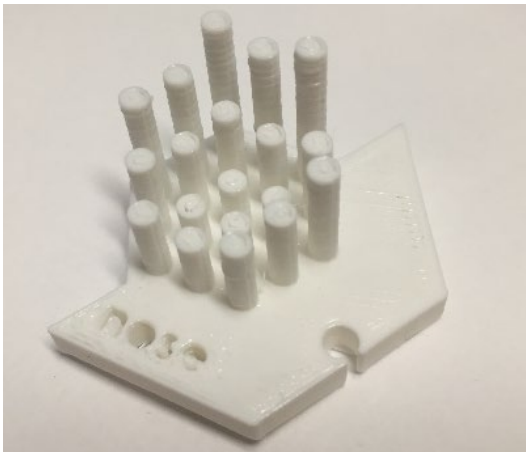

Figure 3.3. A picture of a 3D printed insert.

actuator was driven to the extended “treatment” position, the rod pusher was driven forward, and each leg of the rod pusher dove forward each corresponding rod. In the treatment position, each ^{90}Y source's relative position – located at the distal end of each rod – corresponded to the individual length of each rod pusher leg.

3.1.1 ^{90}Y Source Description

To fabricate the novel ^{90}Y sources, stable yttrium-89 (^{89}Y) disks were obtained from American Elements (Los Angeles, CA, USA). The ^{89}Y disks had a mean diameter of 2.03 ± 0.01 mm and a thickness of 1.01 ± 0.01 mm (n = 24). The disks were measured with a 6-inch digital Vernier caliper. The ^{89}Y disks were shipped to Mo-Sci Corporation (Rolla, MO, USA), who sealed ten disks per 1 quartz glass vial. Once sealed, the vials were shipped to the MURR for activation by slow neutron bombardment to ^{90}Y before being shipped to the University of Minnesota. The requested activity at delivery was 1 mCi per disk or a total of 10 mCi for each sample.

3.1.2 ^{90}Y Source Placement Procedure

During film-based measurement, it was discovered that some of the ^{90}Y sources were not laying flush with the inner bottom surface of the tips as necessary. The solution was to use medical-grade silicone to adhere each source to the bottom of a rod and then placing the rod and source in a tip using a 3D printed specially made source loading tool. The base of the tool had an opening large enough for a source to fit in it. The base was also thinner than the height of the disk-shaped sources. This feature allowed the sources to contact the work surface and the distal end of one of the rods simultaneously. When the rod – with silicon – was removed from the tool, the ^{90}Y source was also lifted out. The modified procedure of loading the sources is depicted in Figure 3.6.

3.2 Dose Rate Determination

3.2.1 Film Calibration

Film calibration was performed with a clinical linear accelerator (Varian Clinac iX, Varian Medical Systems, Palo Alto, CA) in 6 MeV electron mode. Pieces of film (3.5 × 3.5 cm^2) were placed at the depth of maximum dose (d_{max} = 1.2 cm) in Solid Water® HE (SW) (Sun Nuclear Gammex, Middleton, WI) during irradiation. The film was exposed to 0-1000 cGy in 100 cGy increments using a 10 × 10 cm^2 field size. After development, the films were placed in the center of an Epson Expression 11000XL scanner's scanning area. The scanner was set to transmission scan mode, with 48-bit color and 72 dpi (0.0353 cm per pixel) resolution. An imaging processing software (ImageJ, U.S. National Institutes of Health, Bethesda, MD, USA) was used to measure each dose's average scanner response. Red channel scanner response was converted to $netOD$ and fit to a rational function (Equation 2.17) by a non-linear least square fit.

As was discussed in section 2.6.1, certain uncertainties exist when performing single-channel film dosimetry. For this work, steps were taken to mitigate most of those uncertainties. Ten warm-up scans were always performed and a self-development period of 12 or 24 hours was applied. Care was taken to not touch the ROI of the films and nitrile gloves were always worn when handling. These actions prevented inadvertent marking of the ROIs with fingerprints or scratches. Care was also taken to place each piece of film in the same orientation within the flatbed scanner. Finally, a black, opaque piece of card stock with an open central window was placed over the film's edges. This black cardboard ensured that all pieces of film were placed flat in the scanner and were read in the same position, mitigating scanner lateral effects. Marroquin et al. reported that for their system, EBT3 film has a total red channel dose uncertainty of 3.2% [96]. With the steps taken to mitigate uncertainty, it was felt that 3.2% was a reasonable, if not conservative, value.

3.2.2 Experimental Measurements

The depth of the film measurements was radiologically scaled to account for the differences in densities between EBT3 film and water – or SW, which allowed for a more accurate comparison between simulation and measurement. EBT3 film consists of an active layer sandwiched between two matt-polyester base layers. The active layer has a nominal thickness of 0.0028 cm, a density of 1.20 g/cm^3, and a radiological scaling factor of 1.158 g/cm^3. Each polyester layer has a nominal thickness of 0.0125 cm, a mass density of 1.35 g/cm^3, and a radiological scaling factor of 1.238 g/cm^3 [94,97]. The radiological thickness (r_{rad}) of EBT3 film is:

$$r_{rad} = (1.158)(0.0028\ \text{cm}) + (2)\,(1.238)(0.0125\ \text{cm}) = 0.0341\ \text{cm} \qquad (3.1)$$

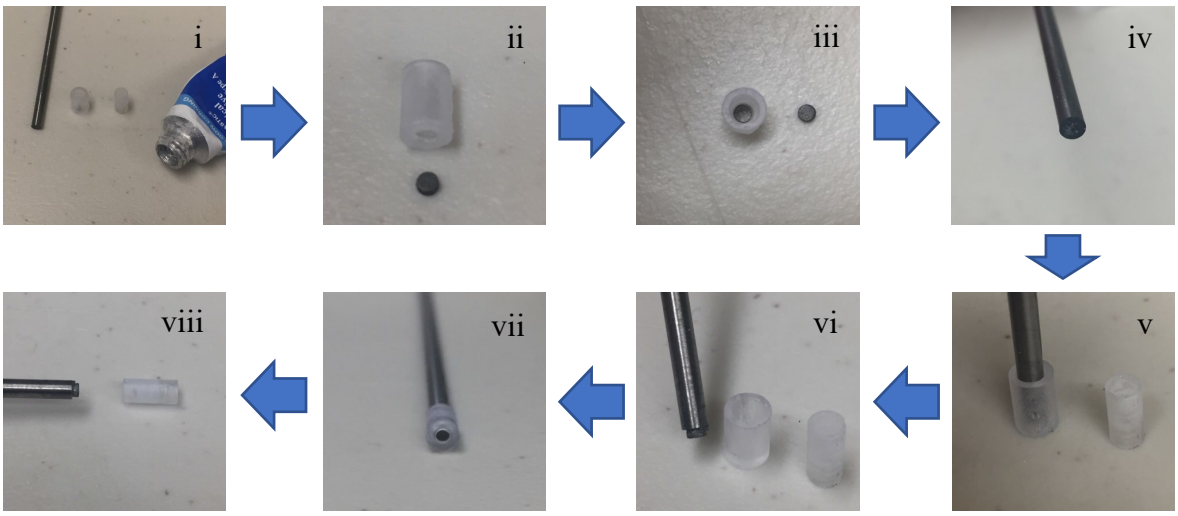

Figure 3.6. ^{90}Y CSBT device source loading procedure.

(i) Source placement tool, medical grade silicone, rod, and tip
(ii) Source placement tool and source
(iii) Source in contact with the work surface within the placement tool
(iv) Distal end of rod with small dab of silicone
(v) Rod with silicone in contact with source within placement tool
(vi) Source adhered to distal end of rod
(vii) Rod and source placed with treatment tip
(viii) Tip removed after treatment. The source remained adhered to the rod.

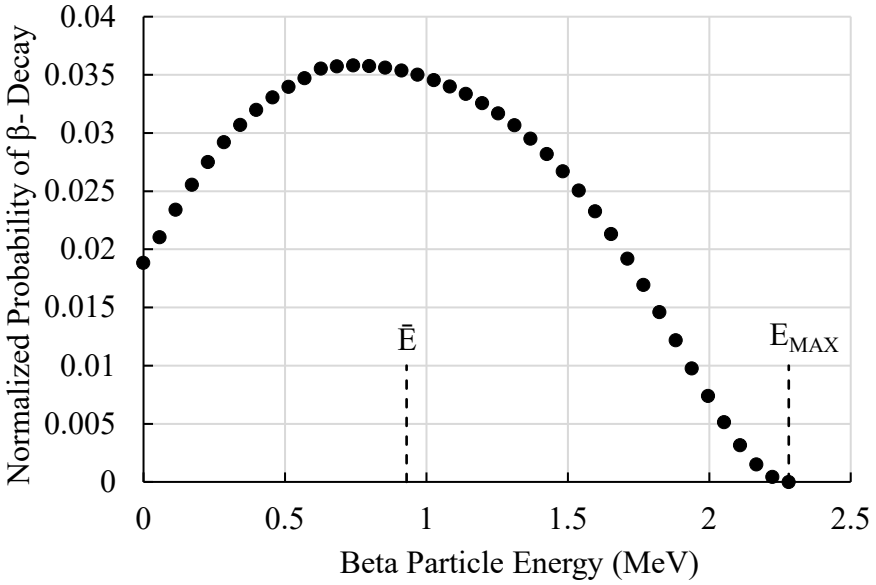

Figure 3.7. The beta particle energy spectrum of ^{90}Y. The data was extracted from ICRU56.

For depth measurements, the point of measurement was assumed to be at half the thickness of the EBT3 film, so for measurement with 0.1 cm of SW, r = 0.1 cm + 0.03410/2 cm = 0.1171 cm. This radiological range was only applied in the normal direction relative to the surface of the film.

3.2.3 Monte Carlo Transport Simulations

In the report of Task Group 268 (TG268) [98], the AAPM has provided recommendations to improve the reporting of MC studies in medical physics research and provides a template table to report relevant details of MC simulations. The "Update of AAPM Task Group No. 43 Report" (TG43U1) [99] provides recommendations for MC simulation of dose-rate distributions from photon-emitting brachytherapy sources. The current document aims to adhere to the recommendations of TG268 and TG43U1, accounting for the fact that the radionuclide being studied here, ^{90}Y, is a beta emitter.

The Monte Carlo n-particle code – version 5 (MCNP5) [100] was used to simulate the energy deposited, in MeV, in each user-defined voxel, achieved by the implementation of the modified energy deposition tally (*F8). The EL03 electron physics library database [101] and the MCPLIB04 photo atomic library database [100] were selected to define the problems' interaction cross-sections. With the release of MCNP5 (2002) came a new electron energy indexing algorithm, namely the energy and step-specific method [102]. This energy straggling logic was used for all simulations. Bremsstrahlung photons generated by the interaction of beta particles in the medium were also considered in the MC simulation of total dose deposited.

In ^{90}Y decay to the ^{90}Zr ground state, there is a very low abundance of gamma (γ) emission (1.7 MeV, 0.0115%). This γ contribution to dose was considered negligible and was not incorporated into the simulation source spectrum definition. The ^{90}Y beta spectrum was extracted from ICRU-56, Table D.1. [22] In simulations involving volume sources, each ^{90}Y source was defined to have a mass density of ρ = 4.47 g/cm^3, a diameter of 2.03 mm, and a thickness of 1.01 mm. Figure 3.7 shows the ^{90}Y beta particle energy spectrum used for all simulations.

Energy deposition was calculated in a simulated water phantom with an atomic composition of 2:1 for H:O and a mass density of ρ = 0.998 g/cm^3, the density of water at

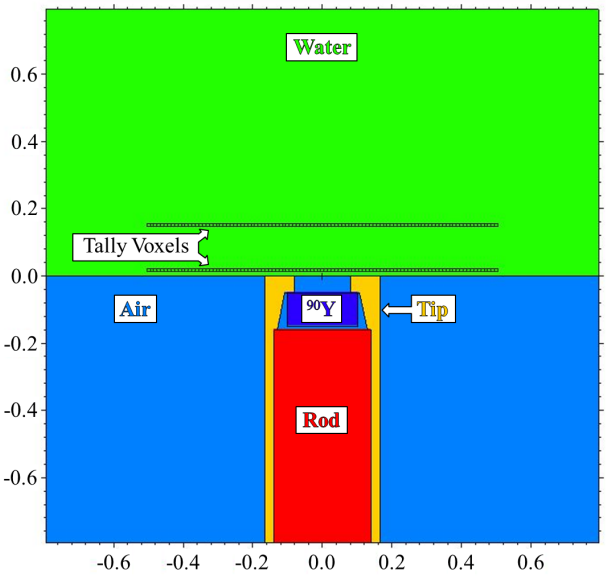

Figure 3.8. Typical geometry of an MCNP5 single tipped source dose rate simulation.

standard temperature and atmospheric calibration conditions [103]. For simulations involving the source/tip/rod assembly, the tip material was defined as acrylic acid ($C^3H^4O^2$) with a mass density of 1.15 g/cm^{3,} and the rod material was defined as 50% tungsten and 50% carbon with a mass density of 15.63 g/cm^3. The remaining volume within the problem's geometric space was defined as air with a mass density of ρ = 0.0013 g/cm^3 and composition of 78.09% nitrogen, 20.95% oxygen, and 0.96% argon.

Figure 3.8 depicts the geometry of a typical MCNP5 simulation. Each simulation's origin was located at the intersection of the water phantom's surface and the longitudinal central axis of the ^{90}Y disk and the central axis was always aligned perpendicular to the phantom surface. The initial voxel, used for calculating energy deposited, was centered about the point x = 0 cm, y = 0 cm, and z = 0.0171 cm, where the positive z-direction corresponded to the direction of increasing depth in the phantom. The voxel dimensions were 0.01 by 0.01 by 0.01 cm^3. The initial voxel was repeated throughout the phantom's volume to create a distribution of voxels for energy deposition simulation. For each voxel, the point of calculation was considered to be at the geometric center of each voxel.

In the direction of the source axis, the sample weighting was linear. In the radial direction, sample weighting was radial ("SP -21 1" in the source probability definition). For curved sources, neglecting to appropriately define for radial sampling will result in an uneven activity distribution within the source. Although MCNP5 will appropriately define for radial sampling by default in many cases, it behooves the user to verify that the activity distribution is properly defined. The MCNP5 software output provides eleven clear metrics for the reliability of simulation. For a simulation to be considered reliable, each of the eleven metrics must have passed upon completion of the simulation. The pass/fail state of ten of the metrics is provided in the MCNP5 output file as "passed" or "failed". The eleventh metric is the estimated relative error (R) and is provided for each mean tally value calculated. It is defined as the fractional standard deviation ($S_{\bar{x}}$) in the mean ($\bar{x}$), i.e., $R = S_{\bar{x}}/\bar{x}$. The MCNP5 manual recommends a 1σ (k = 1, 67%) $\leq$ 10% to be generally reliable except for point detectors, and TG43U1 recommends $1\sigma \leq 2\%$ at $r \leq 5$ cm for photons.

To validate the MC simulations, the depth dose rate from a single ^{90}Y source was simulated and compared to comparable film-based measurements. For the simulation, a single bare source was placed directly on the water phantom and the energy deposited per voxel was simulated. To perform the measurements, a single ^{90}Y source was placed above pieces of dosimetric film for a specified time. The source's dose rate was then defined after converting the film response to dose using appropriate film calibration. The time of each measurement was recorded to account for inter-measurement decay.

3.2.4 Gamma Analysis

Gamma analysis quantitatively compares two dose distributions in one, two, or three dimensions [104]. Its primary function is to compare a measured distribution to a calculated (or simulated) distribution for quality assurance. The standard gamma function

is a function of two defined passing criteria, namely the dose-difference (DD) criterion (ΔD_M) and the distance-to-agreement (DTA) criterion (Δd_M). Considering the gamma analysis of two single point dose distributions, the spatial point of measurement is defined by the vector $\mathbf{r}_m$ and the spatial point of calculation is defined by the vector $\mathbf{r}_c$. The scalar distance (r) between the point of measurement and the point of calculation is simply:

$$r(\mathbf{r}_m, \mathbf{r}_c) = |\mathbf{r}_c - \mathbf{r}_m| \tag{3.2}$$

Similarly, the dose difference (δ) between the magnitudes of the doses (D_c and D_m) at the measurement and calculation points is:

$$\delta(\mathbf{r}_m, \mathbf{r}_c) = |D_c(\mathbf{r}_c) - D_m(\mathbf{r}_m)| \tag{3.3}$$

Normalizing the variables δ and r by the gamma criteria ΔD_M and Δd_M, respectively, scales the spatial and dose magnitude differences and makes them unitless. The gamma function (Γ) is equal to the dimensionless euclidian distance between the two normalized points.

$$\Gamma(\mathbf{r}_m, \mathbf{r}_c) = \sqrt{\frac{r^2(\mathbf{r}_m, \mathbf{r}_c)}{\Delta d_M^2} + \frac{\delta^2(\mathbf{r}_m, \mathbf{r}_c)}{\Delta D_M^2}} \tag{3.4}$$

In three dimensions, Equation 3.4 is a spherical surface when equal to a constant. By setting Γ equal to 1, δ will equal ΔD when r equals 0 and r will equal Δd when r equals 0. Determining the minimum $\Gamma(\mathbf{r}_m, \mathbf{r}_c)$ for each $\mathbf{r}_c$ yields the quality index $\gamma(\mathbf{r}_m)$.

$$\gamma(\mathbf{r}_m) = min\{\Gamma(\mathbf{r}_m, \mathbf{r}_c)\} \forall \{\mathbf{r}_c\} \tag{3.5}$$

The passing criterion therefore becomes

$$\gamma(\mathbf{r}_m) \leq 1, \text{ calculation passes.} \tag{3.6}$$

Following the mathematical formalism presented by Low et al. [104], a two-dimensional gamma analysis script was written in-house (MATLAB ver. R2019a) to

compare MC simulated and measured planar dose distributions. The gamma analysis script was commissioned by comparing the in-house script results to clinical intensity-modulated radiation therapy (IMRT) QA results of a commonly used and commissioned gamma analysis radiation detector array and accompanying software (MapCheck 2, Sun Nuclear Corporation, Melbourne, FL, USA). The gamma analysis criteria were $\Delta D_M = 3\%$ for DD and $\Delta d_M = 3$ mm for DTA. The dose threshold was 10% of the maximum measured dose.

Eight comparisons were made. MapCheck gamma analysis result files for veterinary IMRT cases were chosen at random of all eight comparisons. Figure 3.9 displays the planar dose distributions and corresponding failed gamma analysis points for the Matlab script and MapCheck software. The only points that contributed to the number of "total points" were greater than the 10% threshold. For each comparison, the Matlab script performed the analysis on more data points than the MapCheck software. The difference in the number of "total points" ranged from one to 35. For six of the eight comparisons, the difference of "total points" was less than 10.

The passing percentage of the MapCheck-based gamma analyses was 100% for six of the eight comparisons. For the same Matlab-based analysis, gamma analyses were between 96.2% and 99.4%. Table 3.1 shows the gamma analysis of each of the eight comparisons.

Given the small size and high dose gradients of the ^{90}Y source, the DD criterion was kept at $\Delta D_M = 3\%$ and the DTA criterion was tightened to $\Delta d_M = 0.71$ mm. The Δd_M value was chosen because, with the scanned film resolution of 0.0353 cm/pixel, it encompassed data points within two pixels of the measurement point. The gamma analysis dose threshold was set to the commonly used value of 10% of the maximum dose.

Table 3.1. Gamma analysis results showing the differences between the Matlab (ML) script and the MapCheck (MC) software.

	Trial 1	Trial 2	Trial 3	Trial 4
	ML | MC	ML | MC	ML | MC	ML | MC
Total Points	53 | 54	151 | 155	112 | 128	157 | 161
Passed Points	51 | 54	149 | 155	110 | 128	153 | 161
Failed Points	2 | 0	2 | 0	2 | 0	4 | 0
Percent Passed	96.2 | 100	98.7 | 100	98.2 | 100	97.5 | 100

	Trial 5	Trial 6	Trial 7	Trial 8
	ML | MC	ML | MC	ML | MC	ML | MC
Total Points	160 | 168	144 | 150	150 | 159	117 | 152
Passed Points	159 | 168	141 | 150	133 | 142	113 | 147
Failed Points	1 | 0	3 | 0	17 | 17	4 | 5
Percent Passed	99.4 | 100	97.9 | 100	88.7 | 89.3	96.6 | 96.7

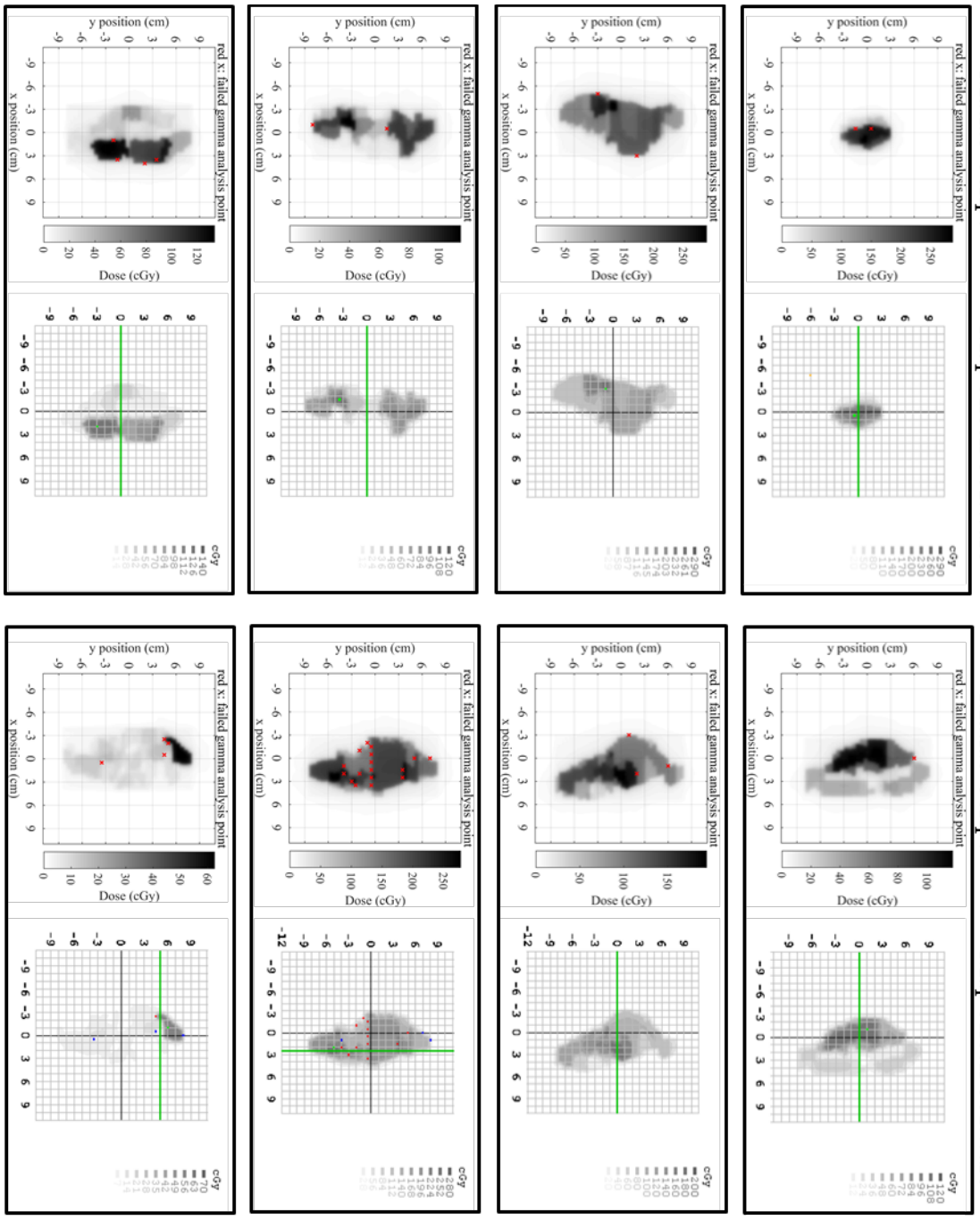

Figure 3.9. Eight comparisons of the Matlab script and MapCheck planar dose distributions displaying the failed gamma analysis points for each.

Chapter 4

^{90}Y Source Characterization

Aim 1 was to fully characterize the ^{90}Y source to be used in the CSBT device. Characterization of the bare and tipped sources revealed the full in water dose distributions of individual sources. This was done by performing film-based measurements and comparing those measurements to equivalent MC simulations.

Because of the rapid dose falloff, dosimetric characterizations of beta-emitting brachytherapy sources are full of unique challenges. Monte Carlo simulation aided in the source characterization, but before simulated data could be considered useful, it was required that the accuracy of the simulation was thoroughly assessed. A benchmarking dose point kernel simulation was performed. The resulting simulated radial dose distribution was compared to data from ICRU-56 [22], ensuring the accuracy of the fundamental MC simulation input parameters such as the ^{90}Y source beta particle spectrum and the particle interaction probability distribution libraries.

Ensuring controlled and accurate dose delivery from the CSBT device required a thorough and complete characterization of dose deposited within the target media. It was necessary to understand the influence of source, source placement, timing, and

measurement uncertainties. Bare source characterization was achieved through GAFChromic film measurement and MC simulation.

When installed in the CSBT device, each ^{90}Y source was held to a rod end by a 3D printed tip (Figure 3.4). Due to the design of the tip, the minimum source-to-surface distance was 0.45 mm. The tip also interacted with the particle fluence and altered the dose distribution. Through experimental measurement and simulation, the rod-source-tip assembly was fully characterized.

In this chapter, the initial characterization of the tipped ^{90}Y source is presented. The initial step was to ensure that the MC simulation was functioning properly by performing a benchmarking simulation. Following that, simulations of the depth dose and cross profiles were compared to the dose distributions of film-based measurements. These comparisons validated the MC simulated dose distributions. Finally, a dose rate uncertainty analysis and isodose depth distribution for a single tipped source are presented. Following TG268, Table A.1 of Appendix A lists the parameters for the tipped single and seven-source MC simulations presented in this chapter.

4.1 Benchmark Simulation

To benchmark the MC simulations, the ^{90}Y point source radial dose function in a very large water medium was simulated and compared to equivalent data presented in ICRU-56 – Appendix C. For the MC simulation, one ^{90}Y point source was placed in the center of a very large (r = 2 cm) spherical water medium with n = 200 scoring shells with radii $r_i = n_i \times 0.01 + 0.005$ cm (Figure 4.1.a). This benchmarking simulation's error requirement was $1\sigma \leq 1\%$ at $r \leq 0.9 \times R_{CSDA} = 1.0161$ g·cm^{-2}.

The MC simulation required 5×10^7 histories to pass the ten tests performed by MCNP and to reach the statistical error requirement (Figure 4.1.b). The error remained below 0.1% for radius $r \leq 0.71$ cm. Beyond 0.71 cm, the error increased exponentially,

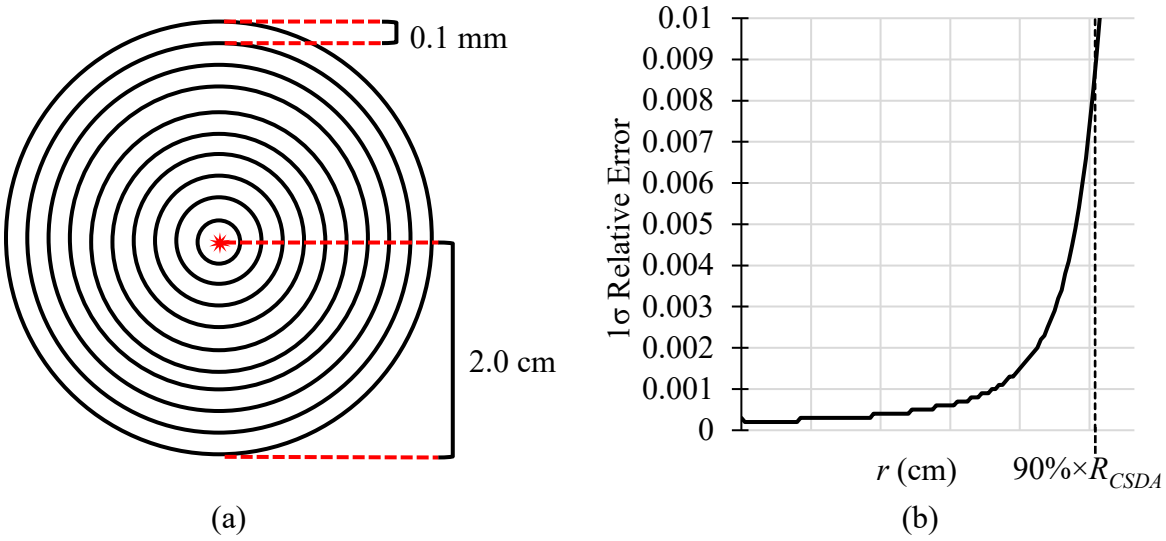

Figure 4.1. (a) MC simulation scoring geometry for the benchmarking dose point kernel simulations. (b) Relative error of the benchmarking simulation.

resulting in a statistical error of 0.91% at $r = 0.9 \times R_{CSDA}$ (1.0161 cm) and 1% at $r = 1.03$ cm.

The comparison of the radial dose functions is shown in Figure 4.2. From 0.016 cm to 0.480 cm from the point source, the MC simulated dose rate was, on average, 1.02% less than the ICRU-56 dose rate. Within the first 0.5 cm, the standard deviation of the percentage difference between the MC dose rate and the ICRU-56 dose rate was 2.31%. ICRU-56 states that, for their data, statistical uncertainty was about 2% and systematic uncertainty was 3-5% for a combined uncertainty of about 4.47%.

The MC simulated radial dose function completed the benchmark and provided a baseline for regions of interest for other MC simulations. Shown in Figure 4.2, for the MC benchmarking simulation, 87% of the beta particle average energy was deposited within 0.5 cm of the point source. Based on this result, for simulations involving volume sources, the region of interest (ROI) was defined as the phantom volume within a 5 mm depth and 3 mm from the source's edge in the radial direction. Simulation relative error within the

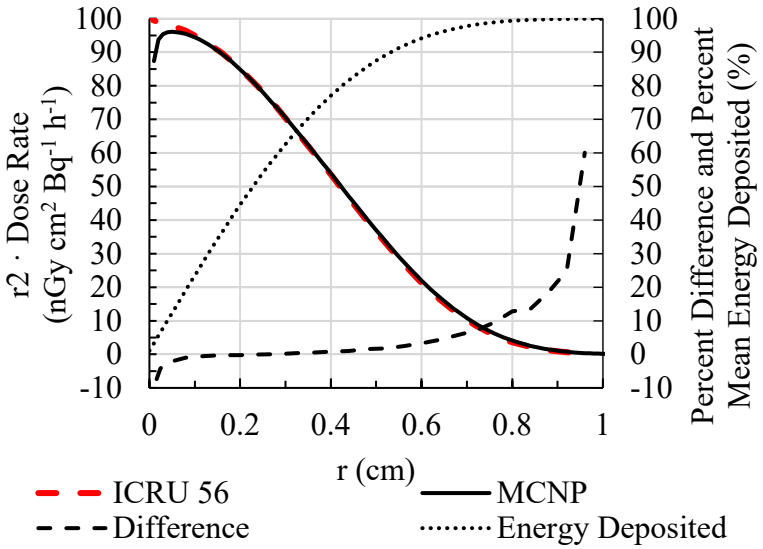

Figure 4.2. MCNP5 benchmarking simulation dose rate and total energy deposited as a function of distance (r).

ROI was limited to $1\sigma \leq 10\%$; however, it was expected that the maximum relative error would occur at a point far from the source.

4.2 Simulation Validation

Validation of the MC simulations was provided by comparing the MC simulated depth dose rate of a volumetric source with film-based dose rate measurements at increasing depth (Figure 4.3). The depths (d) of the film-based measurements have been radiologically scaled, as discussed in section 3.2.2. Measurements were performed at d = 0.0171, 0.1171, 0.2171, 0.3171, 0.4171, and 0.5171 cm for a bare source and d = 0.0171 and 0.1171 cm for a tipped source. Measurements at d = 0.0171 cm, which corresponded to half the thickness of the EBT3 film, were made by placing the source or source tip in direct contact with the film. A 5 cm thick slab of SW was used as backscatter material.

By comparing MC simulated and film measured maximum dose rates at d = 0.1171 cm for a bare source, it was determined that the activity was 24 MBq (0.65 mCi) per source

at the time of first measurement. All other activity measurements were based on that calibration measurement, accounting for source decay between measurements. At $d = 0.1171$ cm, the bare source dose rate was 6.59×10^{-8} cGy·s^{-1}·Bq^{-1}. The measured dose rate at $d = 0.0171$ cm was 3.46×10^{-7} cGy·s^{-1}·Bq^{-1} for a bare source and was 1.37×10^{-7} cGy s^{-1} Bq^{-1} for a tipped source. In the case of a bare source, the maximum measured surface dose rate was 21% greater than the maximum MC simulated dose rate. At each measured depth, the MC simulated depth dose rates were within 12.9%, on average, of the measured dose rates.

Bare and tipped source dose rate profiles are shown in Figure 4.4. Analyzing the profiles in a method similar to gamma analysis distance-to-agreement (DTA), the nearest MC simulated dose to each measured dose was within roughly 0.02 cm – equivalent to two tally voxels of the MC simulations. Including the source holder tip increased the distance between the source and the point of measurement by 0.16 cm. In conjunction with the

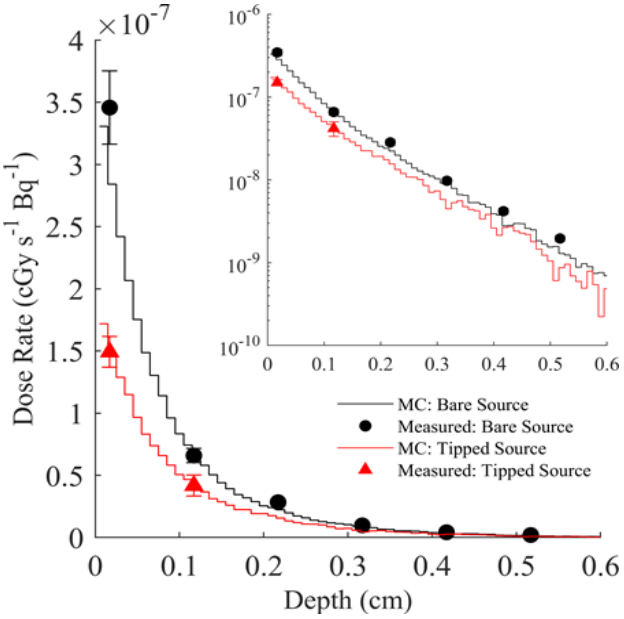

Figure 4.3. MC simulated and measured depth dose rates for a bare and a tipped ^{90}Y source placed on the surface of a water-equivalent phantom. The thickness of the EBT3 film was radiologically scaled to make the depth of measurement water equivalent. The error bars represent the total combined uncertainty (k = 1) of each measurement.

scattering and attenuating effects of the particle fluence due to intersecting tip material, that action decreased the central axis dose rate at $d = 0.0171$ cm by 58%. Also, at $d = 0.0171$ cm, the full-width-half-max (FWHM) of the tipped source profile was 28% larger than the FWHM of the bare source.

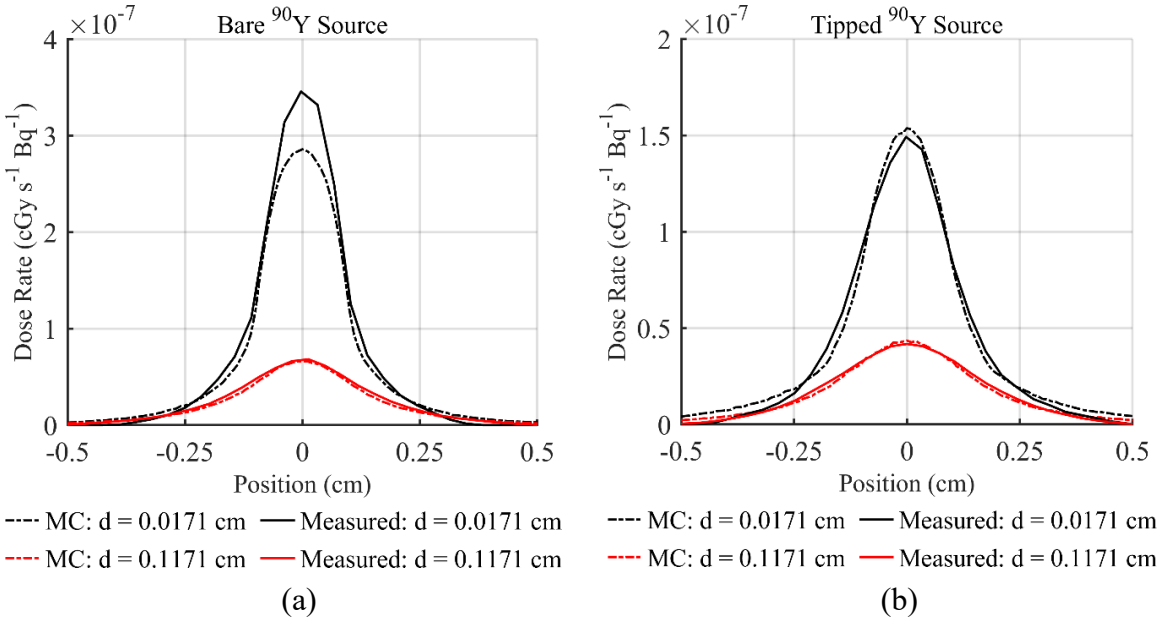

Figure 4.5. Film-based measured and MC simulated dose rate profiles in water at d = 0.0171 cm and 0.1171 cm or 0.1513 cm. (a) Profiles for a bare source placed on the surface of a water-equivalent phantom. (b) Profiles for a tipped source with the distal end of the tip placed.

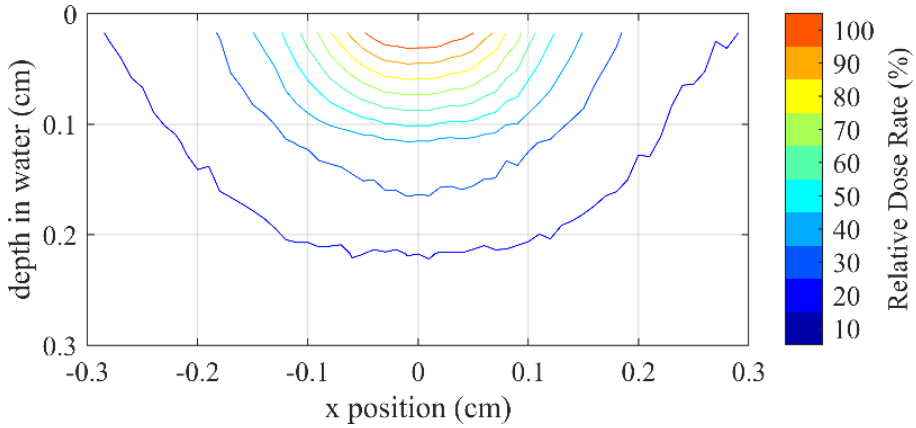

Figure 4.4. Dose distribution in water for ^{90}Y superficial brachytherapy source within the source holder tip of the CSBT applicator.

The two-dimensional depth dose distribution of a single tipped source is shown in Figure 4.5. The distribution is normalized to the maximum central axis dose at d = 0.0171 cm and shows the dose falloff and divergence from the tipped ^{90}Y source. This distribution

is reintroduced in the following chapter as part of the source superposition based multi-source CSBT characterization.

Figure 4.6 shows the MC simulated planar dose distribution at $d = 0.0171$ cm for seven tipped sources. The tipped sources were located directly on a water phantom's surface and replicated one possible source arrangement of the CSBT device. Figure 4.6.a shows the MC simulated surface distribution superimposed with the measured surface dose distribution. Figure 4.6.b shows the MC simulated surface dose distribution with the red crosses representing the failed gamma analysis points for a film-based measurement with setup conditions equivalent to the MC simulation. A total of 1,199 measurement points were compared, with 71 of those points failing to meet the defined passing criteria. The passing rate was 94.08% with a dose threshold of 10%, a dose-distance (DD) criteria of 3%, and a DTA criteria of 0.7056 mm (twice the film measurement resolution of 0.353 mm).

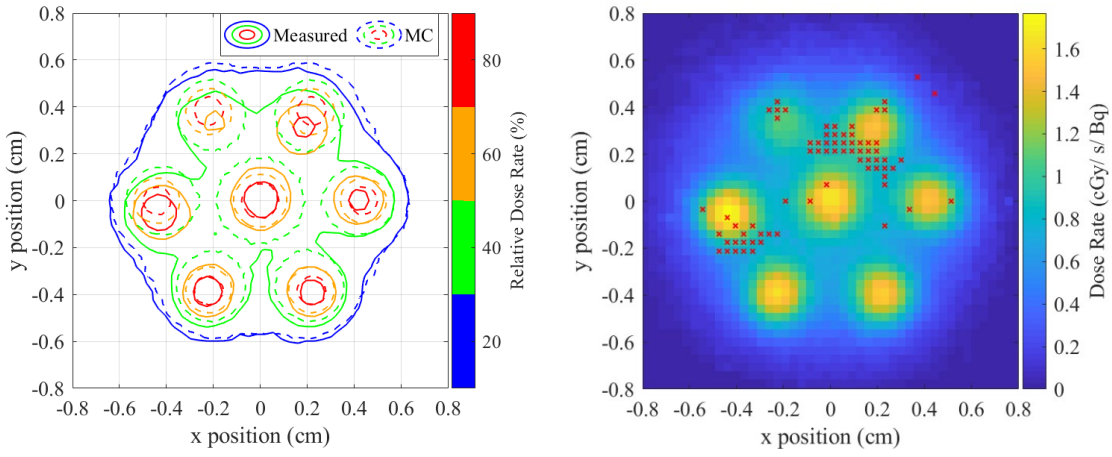

Figure 4.6. Planar dose rate distributions at $d = 0.0171$ cm for six tipped sources located directly on the water equivalent phantom surface. (a) Relative measured and MC simulated planar distributions. (b) MC simulated planar dose rate distribution. The red crosses indicate the calculation points of the measured dose rate distribution where gamma analysis criteria were not met. The passing rate for this analysis was 91.58%.

The maximum dose rate was 1.95×10^{-7} cGy·s^{-1}·Bq^{-1} and 1.78×10^{-7} cGy·s^{-1}·Bq^{-1} for the simulated and measured distributions, respectively. The six maximum dose rates nearest the six non-central sources were, on average, 90% of the maximum dose rate. The central axis dose rate for a single tipped source, shown in Figure 4.3 and Figure 4.4.b, was 1.55×10^{-7} cGy·s^{-1}·Bq^{-1} for the MC simulation and 1.49×10^{-7} cGy·s^{-1} Bq^{-1} for measurement. Including six additional tipped sources increased the maximum dose rate by 26% for both simulation and measurement (Figure 4.6). As shown in Figure 4.7, the surface homogeneity was low. At d = 0.1171 cm, the homogeneity improved significantly, and at d = 0.3171 cm the distribution was continuous. The spreading of dose with increasing depth is a function of scattering within the medium and divergence of the radiation.

At the depth of measurement, the maximum dose rate for the MC simulated and the measured dose distribution occurred nearest the center of the center-most source. The maximum dose rate was 1.95×10^{-7} cGy/s/Bq and 1.78×10^{-7} cGy/s/Bq for the simulated and measured distributions, respectively. The six maximum dose rates nearest the six non-

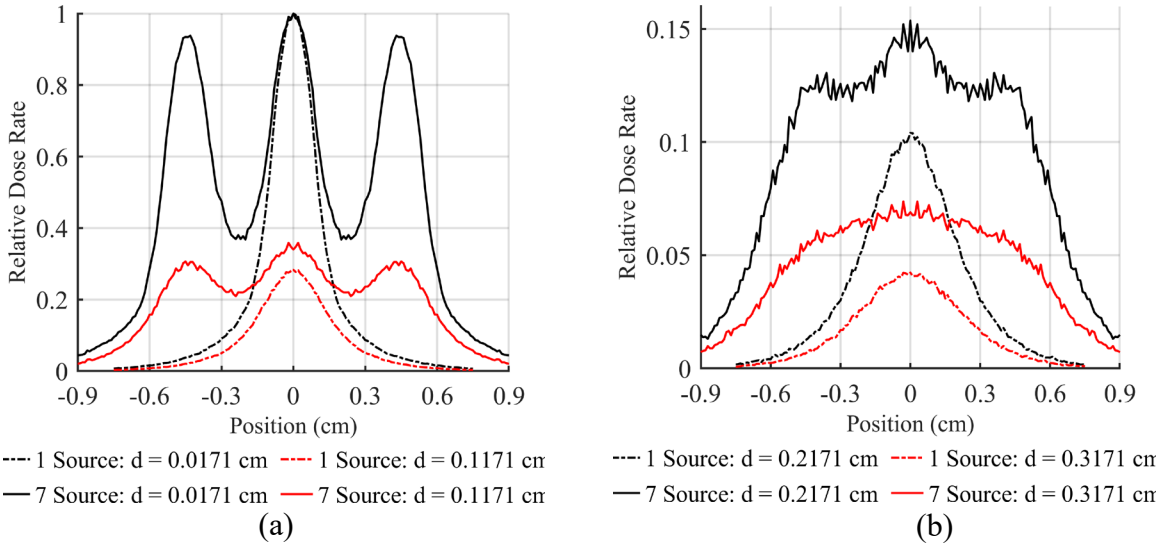

Figure 4.7. MC simulated relative dose profiles for a single tipped source and a matrix of seven sources. The seven-source profile at y = 0 in Figure 4.6. (a) Depths in water of 0.0171 cm and 0.1171 cm. (b) Depths in water of 0.2171cm and 0.3171 cm.

central sources were, on average, 90% of the maximum dose rate. Shown in Figure 4.3 and Figure 4.4.b, the central axis dose rate for a single tipped source was 1.55×10^{-7} cGy·s^{-1} Bq^{-1} for the MC simulation and 1.41×10^{-7} cGy·s^{-1} Bq^{-1} for measurement. As illustrated in Figure 4.6, including six additional tipped sources increased the maximum dose rate by 26% for both simulation and measurement.

4.3 Dose Rate Uncertainties

Uncertainties in the dose rate to water from multiple tipped ^{90}Y sources are summarized in Table 4.1. Dose rates from ten bare sources were measured to determine relative source activity variability within a single batch. The standard deviation of these 10 measurements was 2.7%. At d = 0.0171 cm, the CSBT source position uncertainty was estimated to be ±0.25 mm, which corresponded to an estimated dose rate uncertainty of ±3.0% (Figure 4.6). For each film-based measurement, the timing uncertainty was 0.5 seconds for bare source measurements and 1 second for tipped source measurements. For a tipped source, the dose rate uncertainty due to timing error was 1.9% at d = 0.0171 cm. Without considering scanned film orientation and scanner bed homogeneity, EBT3 film has a red channel uncertainty of 3.2% [96]. The measured dimensions of the ^{89}Y disks were

Table 4.1. Estimated uncertainty in dose rate to water from a tipped ^{90}Y source.

Source of Uncertainty	Uncertainty (%)
Source Position	3.0
Source Activity	2.7
Measurement Timing Error	1.9
EBT3 Film	3.2
Source Geometry	2.3
MC Calculation	1.0
Total Uncertainty (k = 1)	**6.0**
Expanded Uncertainty (k = 2)	**12**

0.203 ± 0.001 cm in diameter and 0.101 ± 0.001 cm thick. Four tipped source MC simulations were performed to account for source geometry uncertainty. The uncertainty in diameter (δr) and thickness (δt) were added and subtracted from the nominal source dimensions for the four simulations in the following manner: (+δr, +δt), (+δr, -δt), (-δr, +δt), (-δr, -δt). The resulting average dose rate uncertainty due to geometric source uncertainty was 2.3%. Finally, for a tipped source placed directly on a water-equivalent phantom surface, at d = 0.0171 cm, the estimated maximum dose rate uncertainty (k = 1) was 6.0%.

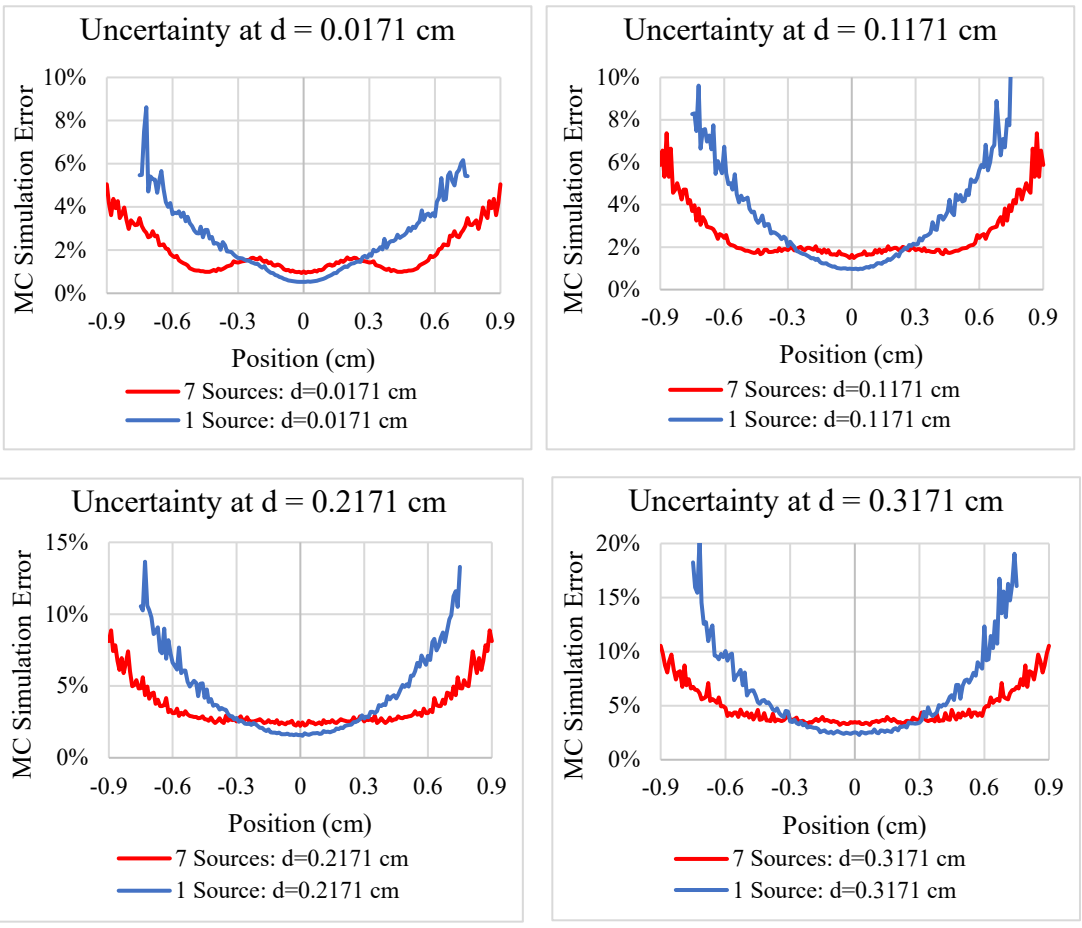

Figure 4.8. Type A simulation error for tipped single and seven-source MC simulations at depths: 0.0171 cm, 0.1171 cm, 0.2171 cm, and 0.3171 cm.

Figure 4.8 shows the y = 0 cm Type A uncertainty profiles for the single and seven-source simulations at d = 0.0171 cm, 0.1171 cm, 0.2171 cm, and 0.3171 cm. For the single source simulations at y = 0 cm, the ROI was $\{x \mid -0.4015 \text{ cm} \leq x \leq 0.4015 \text{ cm}\}$ and $d \leq 0.601$ cm. For the seven-source simulations, the ROIs associated with individual sources overlapped to form a single larger ROI. At y = 0, the ROI was $\{x \mid -0.8515 \text{ cm} \leq x \leq 0.8515 \text{ cm}\}$ and $d \leq 0.601$ cm. Within the ROI of each simulation, the relative error met the $1\sigma \leq 10\%$ requirement.

4.4 Discussion

This chapter presents the first study to describe dosimetric characteristics of ^{90}Y in a customized CSBT device. Importantly, MC simulations were within 10% or 0.02 cm of the measured dose rates for each depth below the surface and can be used to simulate various source arrangements. In the case of the surface dose rate from a bare source, the measured dose rate was greater than the simulated dose rate, which was not unexpected. Other studies have shown that without special calibration, radiochromic film may overestimate surface dose rates [105,106].

Results also demonstrate the need for high precision when treating with beta particle-based superficial brachytherapy. Due to the rapid dose falloff of ^{90}Y, the most superficial few millimeters of tissue will receive nearly 100% of the administered dose. In conjunction with the sources' dose falloff characteristics, the proximity of the sources to the treatment surface will result in a relatively steep dose gradient, resulting in a highly conformal dose distribution.

According to GEC-ESTRO ACROP recommendations in skin brachytherapy [107], the depth of prescription of superficial lesions is usually 3-4 mm when treated with HDR or electronic-based shielded superficial BT applicators[67,108–111]. For the tipped ^{90}Y source, the dose rate at 5 mm depth was approximately 1% of the dose rate at the

surface. For comparison, for the H3 Valencia applicator – a shielded HRD-based applicator – the dose rate at 5 mm depth is approximately 60% of the dose rate at the surface [112]. It is likely that ^{90}Y is only suitable for relatively shallow tumors (<3 mm). As mentioned above, ^{90}Y has been used to successfully treat tumors in mice and humans [77,80,113,114].

As a result of the small source size and the short range of the beta particles, small changes in the source activities or geometries substantially altered the sources' dose rate characteristics. The standard deviation of source activity within one batch of ten activated sources resulted was 1.18%. Therefore, as expected with brachytherapy sources, there may be a 2-3% difference in activity across all sources from the same batch. Variations in source geometry may lead to a 4-5% difference in the dose rates among individual sources, thus supporting source calibration prior to treatment for the batch of sources.

After performing the film-based measurement d = 0.0171 cm for seven tipped sources (Figure 4.6), it was subsequently noted that one of the seven sources was not properly aligned within the source holder tip. Consequently, a source placement tool was designed and constructed to ensure that the sources were properly seated. These data serve to demonstrate the importance of proper pretreatment quality assurance testing. Despite the misaligned source, the measurement still had a pass rate well above 90%. For traditional ^{192}Ir-based HDR-BT, estimated total dosimetric uncertainty (k = 1) has ranged from 5% to 13%, depending on the type of treatment [115]. Therefore, the estimated total uncertainty for multiple 90Y sources of 6.0% was well within an acceptable range. Accounting for potential errors in source spacing will mitigate differences in dose rates, decreasing dose rate uncertainty, and further improving the gamma analysis pass rate.

Chapter 5

CONFORMAL SUPERFICIAL BRACHYTHERAPY APPLICATOR CHARACTERIZATION

In the previous chapter, the basic dosimetry of the ^{90}Y CSBT source was presented. Measured dose rates were compared with simulated dose rates to validate MC simulation of the CSBT ^{90}Y source, and error analysis was performed based on the measurement and simulation of the dose rate of seven CSBT sources.

This chapter delves deeper into the dosimetric characteristics of the ^{90}Y source and the tip-rod assembly, by examining the effect that the tip has on the dose distribution when the tip is placed on the phantom surface. The dose distribution as a function of the tip-to-surface distance is also presented. One of the goals of this work was to generate a treatment planning protocol for the CSBT device. To achieve this goal, it was necessary to determine how the beta particle fluence interacted with other nearby source-tip-rod assemblies and how that interaction affected the dose distributions. It was postulated that if the source-to-source distance is relatively large, then the dose distribution of a multiple source configuration is equal to a superimposed array of equivalent dose distributions.

Table 5.1. Widths of surface dose profiles at different percentages of maximum dose for TSDs: 0.0, 0.01, 0.02, 0.03, 0.04, & 0.05 cm.

TSD	Full Width (cm) at Percentage of Maximum at Phantom Surface				
(cm)	80%	70%	60%	50%	40%
0.0	0.13	0.16	0.18	0.21	0.25
0.1	0.19	0.24	0.29	0.35	0.42
0.2	0.26	0.34	0.42	0.50	0.62
0.3	0.34	0.46	0.56	0.69	0.83
0.4	0.43	0.57	0.70	0.86	1.03
0.5	0.51	0.71	0.88	1.04	1.27

5.1 Effect of increasing the Tip-to-Surface Distance

MC simulations were performed with the standard tip-rod-source assembly to determine the dose distribution change as a function of tip-to-surface distance (TSD). Simulations were performed for TSDs of 0.0 cm to 0.5 cm in 0.1 cm increments. Figure 5.1 shows the normalized depth-profile dose rates for the tipped source at different TSDs. The average dose penetration and dose width both increased as a function of increasing TSD. Table 5.1 lists the full surface dose profile widths at a range of percentages of the maximum dose. At the phantom surface, the full-width-half-maximum (FWHM) increased an average of 0.17 cm per millimeter increase in the TSD (minimum = 0.14 cm; maximum = 0.18 cm).

Figure 5.2.a shows the simulated central axis depth dose rates (left axis) and the dose rates as percentages of the maximum dose rate (right axis) for a tipped source at each TSD. At a depth (d) of 0.0171 cm, the maximum dose rate was 1.53×10^{-7} cGy·s^{-1} Bq^{-1}. These results showed that the maximum dose rate for each TSD decreased by roughly $1/r^2$. Figure 5.2.b shows the depth dose rates for each TSD, normalized to their respective maximum dose rates. With a TSD of 0.0 cm, the relative dose rate decreased by 71.2% at $d = 0.1171$ cm, and by 95.9% by $d = 0.3171$ cm. For a TSD of 0.2 cm, the relative dose rate decreased by 49.9% at $d = 0.0171$cm, and by 88.6% by $d = 0.3171$ cm.

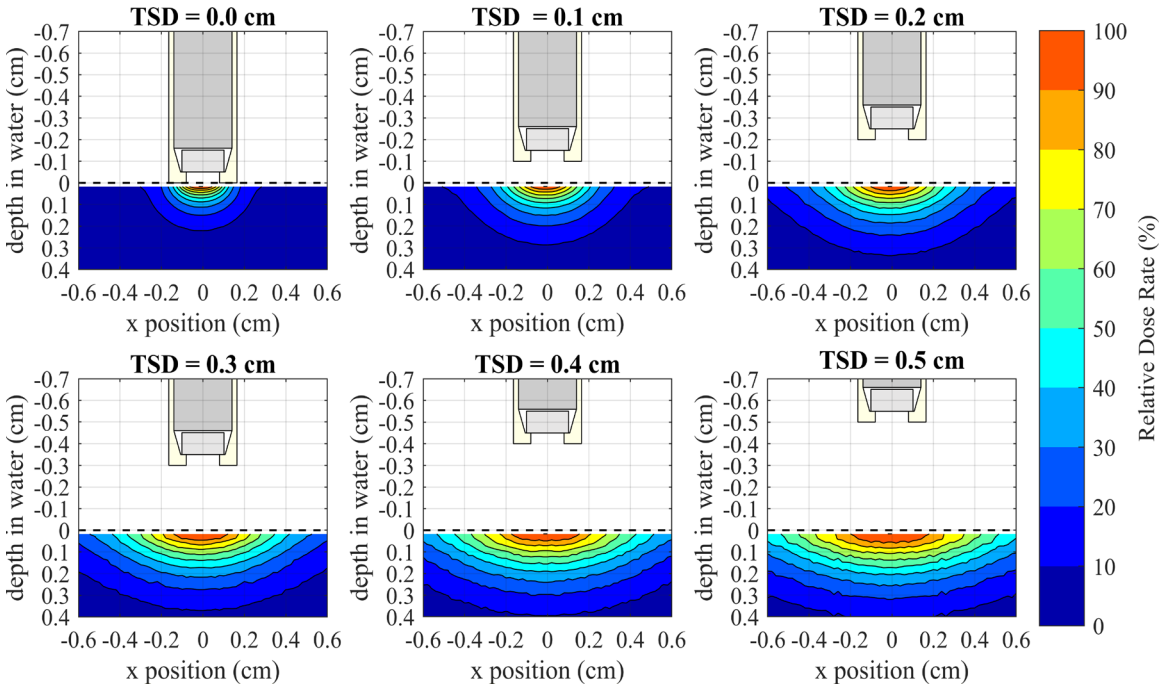

Figure 5.1. Relative profile dose distributions for TSDs: 0.0, 0.1, 0.2, 0.3, 0.4, & 0.5 cm.

5.2 Effect of the Tip on Dose Distribution

The ^{90}Y sources had a nominal thickness of 1.01 mm and a nominal diameter of 2.03 mm. The cylindrical sources' proximal bases were in contact with the distal ends of the tungsten carbide rods and the curved walls of the sources were in close proximity with the 3D printed tips, as were the outer edges of the distal base of each source. The center area of the distal base of each source was exposed directly to the target surface. Within an area close to the target, the emitted electron fluence had the potential of interacting with the tip material, the tungsten carbide rod, or, to a lesser extent, the air between the source and the target.

By MC simulation, the dose rate with a source holder tip was compared to the dose rate for a similar simulation where the tip was replaced by air. For each simulation, the source and rod were in the same position. As the tip material had a higher electron density

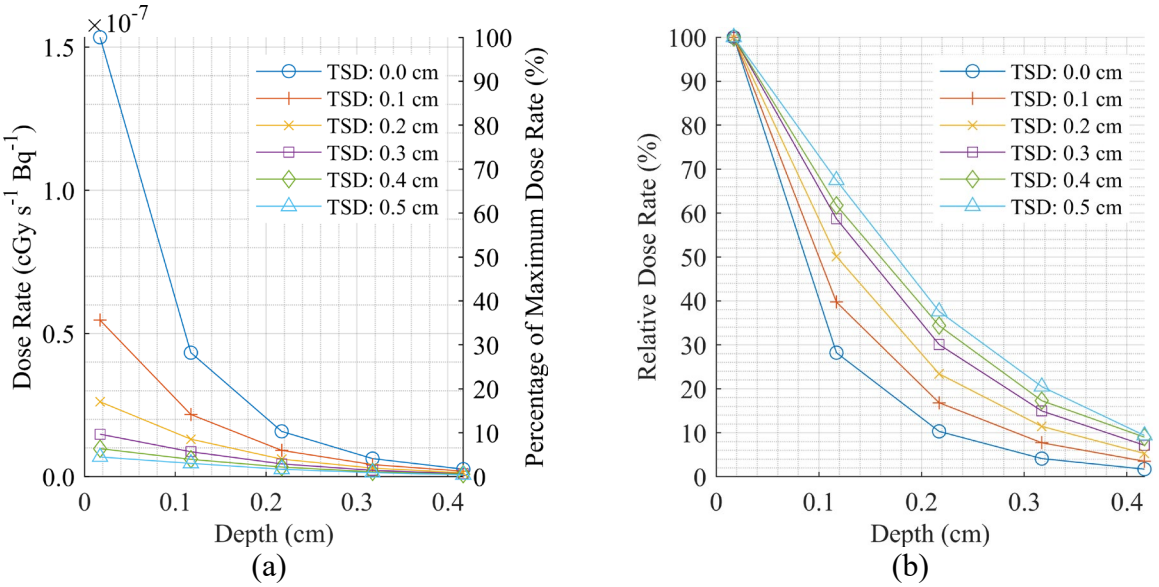

Figure 5.2. Central axis depth dose rates for tipped CSBT sources with increasing TSDs. (a) Absolute dose rates in cGy s^{-1} Bq^{-1}. (b) Percentage depth dose rates normalized to the maximum dose rates for each TSD.

than air, it was hypothesized that the tip caused an increase in electron fluence scatter, which decreased the dose rate in the radial direction.

Figure 5.3.a shows the relative depth profile dose rate for the tipped and untipped sources. It is shown that the width of the dose profile was wider for the simulation with the tip removed for all depths. The central axis depth dose remained unaffected. Figure 5.3.b shows the surface dose rate profiles at $d = 0.0171$ cm and $d = 0.1171$ cm in the logarithmic scale and confirms that the central diameter of 2 mm was unaffected by the tip. The surface dose rate at that width was 55.5% of the maximum dose for each simulation. That region corresponded to the ROI surface area that was exposed directly by the source fluence, unencumbered by the tip material. From the surface dose rate width of 0.2 cm to 0.32 cm, the width of the untipped surface dose rate gradually increased at a rate greater than the tipped source surface dose rate.

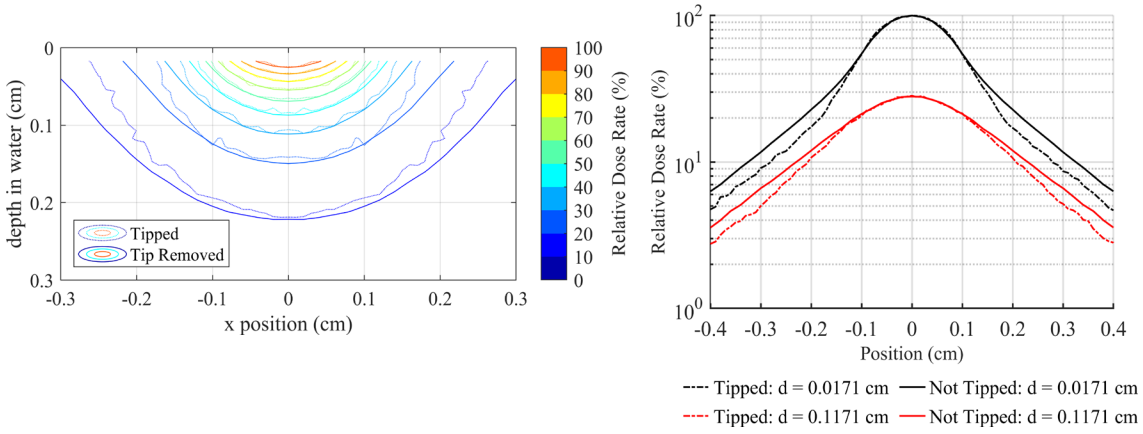

(a) (b)

Figure 5.3. (a) MC simulated profile depth dose distributions showing the effect of the 3D printed source tip when TSD = 0 cm. The dotted line shows the dose distribution of the standard tip-on-surface setup. The dotted line represents the distribution for the exact same setup except that the tip is removed. (b) Percent profile dose at $d = 0.0171$ cm (surface) and $d = 0.1171$ cm for the tipped and "not tipped" CSBT source.

5.3 Source Position and Activity Optimization

The dose distribution of the CSBT applicator may be minutely manipulated by adjusting the TSD or the particle flux exposed to the ROI from individual sources. One method of controlling the particle flux is by using sources of relatively different activities.

MC simulations were performed for a hypothetical abnormally-shaped flat target exposed by the CSBT applicator. The hypothetical target had a "C" shape at the surface. Figure 5.4 illustrates the CSBT source layout for the simulations. Source positions 4, 5, 8, 9, 13, and 14 were void, meaning those rod-tip-source assemblies were not included in the simulations.

In the initial simulation, each source had a TSD of 0.1 cm and equal activities (Figure 5.4.a). For another simulation, the activities were held constant and the TSDs were adjusted (Figure 5.4.b). For another simulation, the TSDs were held constant at 0.1 cm and the relative activities were adjusted (Figure 5.4.c). Finally, another simulation was performed, adjusting each source's TSD and activity (Figure 5.4.d). The objective of

adjusting the TSDs and activities was to yield smoother and more homogeneous dose distributions. Each activity and TSD optimization was performed by trial and error.

Figure 5.5 shows the surface dose rate distribution at $d = 0.1$ cm for each of the four optimization simulations. With each source located at TSD = 0.1 cm and with equal activities (Figure 5.5.a), the surface dose distribution was very inhomogeneous. Sources numbered 1 and 17 were significantly less effective at depositing dose than the cumulated effect of source number 11 and the sources surrounding it. Sources numbered 2, 3, 18, and 19 were also less effective at depositing dose than the sources nearest source number 11.

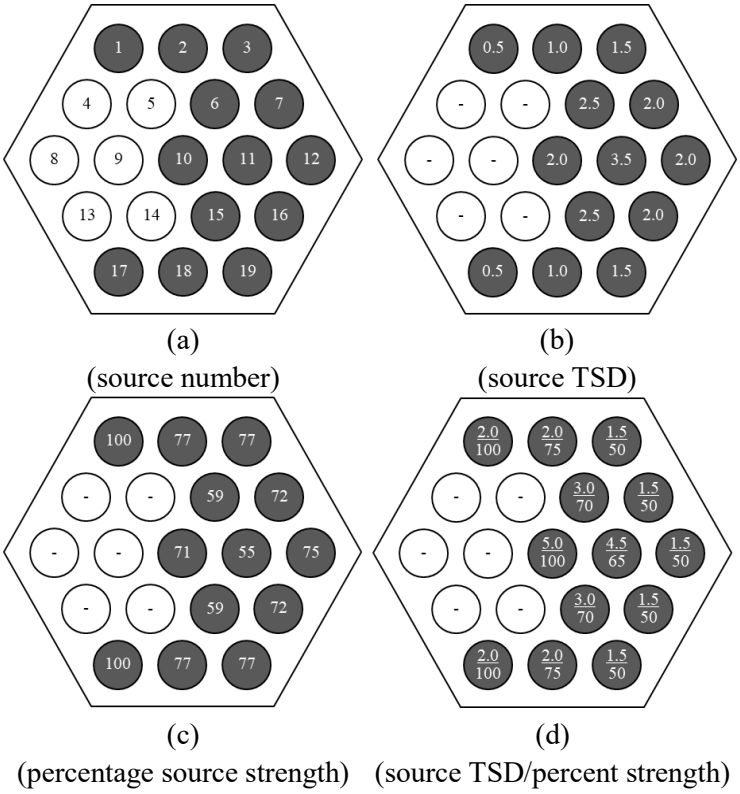

Figure 5.4. Positions and relative activities of the tip-source-rod assemblies for the four MC simulated dose distributions (shown in Figure 5.5). The grey circles represent the sources that were included in the simulations and the white circles represent possible positions of sources that were not included in the simulations. (a) Source numbers. (b) Source TSDs in mm. (c) Relative source activities in percent. (d) Source TSDs in mm (top) and relative source activities in percent (bottom).

By reducing the TSDs of sources near the relatively cold regions of the ROI and increasing the TSDs of the sources near the relatively hot regions of the ROI (Figure 5.4.a), the deviation of the maximum value at each source (x,y) location was reduced and the dose gradient between each source (x,y) location was significantly reduced (Figure 5.5.b). Adjusting the relative activities, rather than the TSDs, had a similar effect in reducing the magnitude of the hot and cold spots (Figure 5.5.c) when compared to Figure 5.5.a. Each

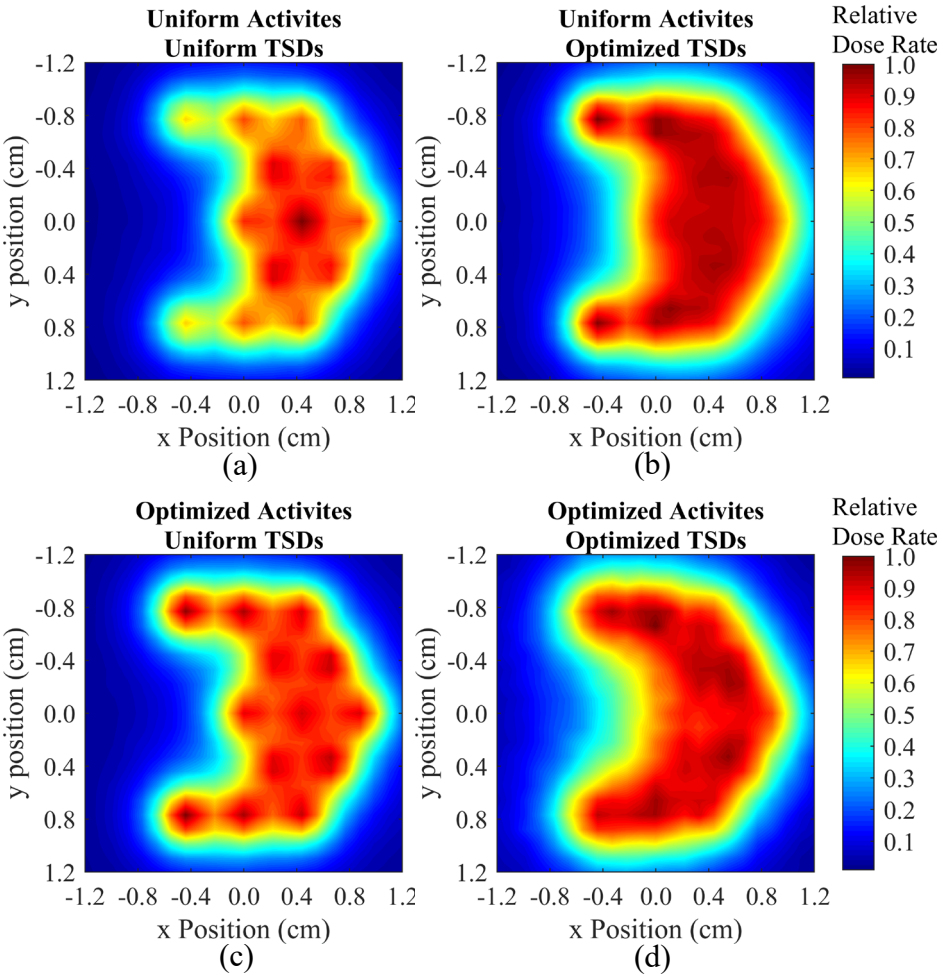

Figure 5.5. MC simulated dose distributions at $d = 0.1$ cm for the exposure of a hypothetical "C" shaped target. (a) Each source had a TSD of 0.1 cm and equal activity. (b) Each source had an equal relative activity. The TSDs of each source was adjusted to redistribute the dose distribution. (c) Each source had an equal TSD of 0.1 cm and the relative source activities were adjusted. (d) The TSD and relative activity of each source was adjusted.

source's (x,y) position was still clearly visible due to the dose gradient between each source being relatively high.

5.4 Superposition of Two Sources

A Matlab script was written to superimpose the simulated dose distribution of a single CSBT source multiple times across an ROI. With the script, it was possible to select the dose distribution for a CSBT source with a TSD of 0.0 cm, 0.1 cm, 0.2 cm, 0.3 cm, 0.4 cm, or 0.5 cm and translate it within its coordinate system. The original dose distribution was centered at $x = 0$ and $y = 0$. The dose distribution was shifted by $x' = -0.225$ cm. A second equivalent distribution was shifted by $x' = +0.225$ cm and the two distributions were summed to generate the superposition distribution. A separate MC simulation was performed with two CSBT sources. The superposition distribution was compared to the simulated two source distribution.

Figure 5.6 shows the MC simulated planar dose distributions of two CSBT sources at depths: d = 0.0171 cm, 0.1171 cm, and 0.2171 cm. The solid lines represent the

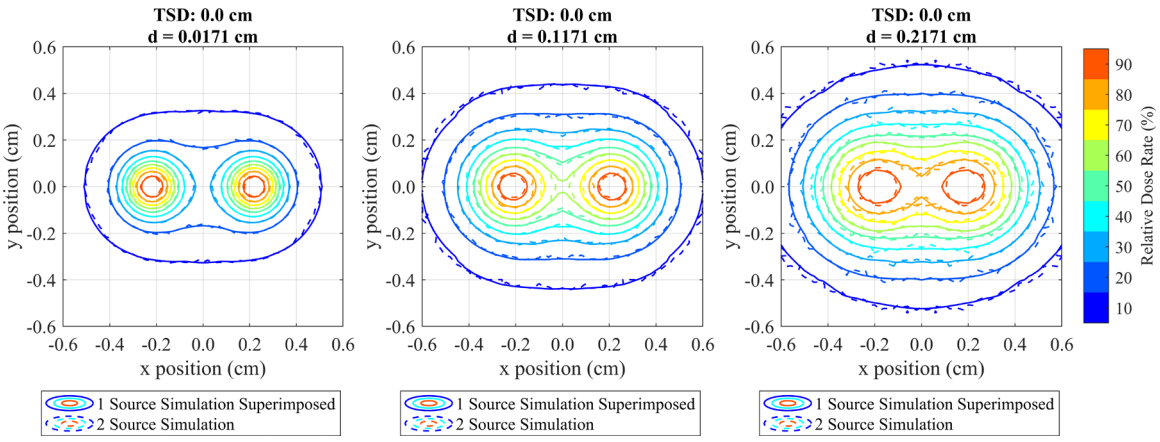

Figure 5.6. Normalized MC simulated planar dose rates for two CSBT sources with a TSD of 0.0 cm. The dashed lines represent the single simulation of two sources. The solid lines represent the superimposed dose rate distribution from a single source.

normalized dose distributions of the two source MC simulation. The dotted lines represent the distributions of the superimposed distributions. Each planar distribution was normalized to its maximum dose.

Gamma analysis was performed for each depth to objectively compare the two sets of distributions. The dose-difference criterion (ΔD_M) and the distance-to-agreement

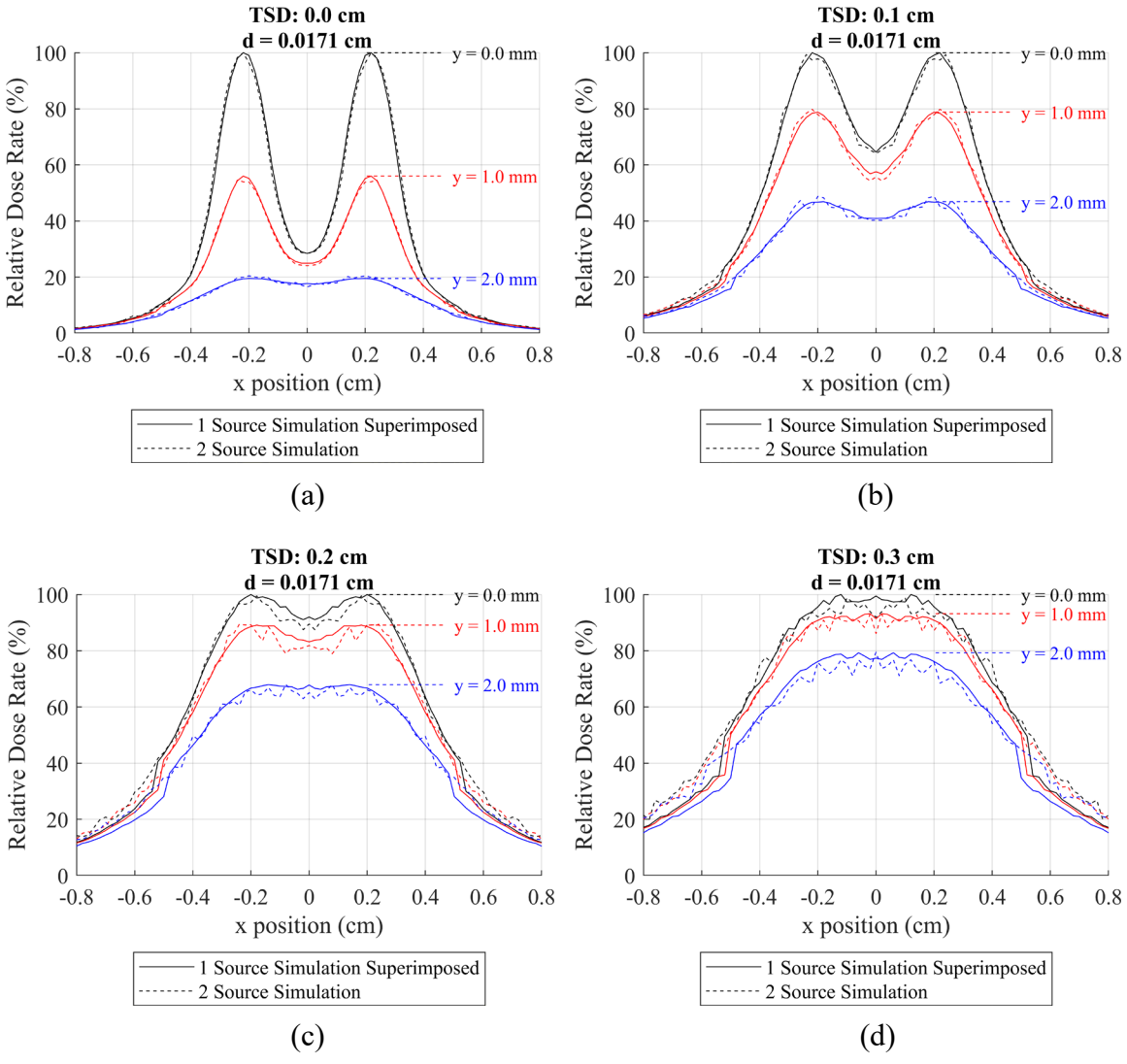

Figure 5.7. Percent surface profile dose of two CSBT sources for TSDs: 0.0 cm, 0.1 cm, 0.2 cm, and 0.3 cm. Each source was positioned on the x-axis. Profiles are shown for y = 0.0 cm, 0.1 cm, and 0.2 cm.

criterion (Δd_M) and dose threshold were set to 2%, 0.05 cm, and 2%, respectively. At $d = 0.0171$ cm, 3785 points were analyzed, and the pass rate was 99.15%. At $d = 0.1171$ cm, 4737 points were analyzed, and the pass rate was 99.5%. Finally, at $d = 0.2171$ cm, 5301 points were analyzed, and the pass rate was 99.7%.

Under the conditions of irradiation from the CSBT with two sources and a TSD of 0.0 cm for each source, it was concluded that the superposition of two single-source dose distributions was equivalent to the simulated dose distribution of two CSBT sources. Therefore, it was concluded that, with the CSBT source center-to-center spacing of 0.45 cm and a TSD of 0.0 cm, the dose distribution has a negligible dependence on the particle fluence of one source that has interacted with neighboring tip-rod-source assemblies.

Figure 5.7 shows the surface profile dose distributions of two CSBT sources for TSDs: 0.0 cm, 0.1 cm, 0.2 cm, and 0.3 cm. The two sources were aligned on the x-axis. Surface dose profiles are displayed for y = 0.0 cm, 0.1 cm, and 0.2 cm. At x = 0 cm, y = 0 cm – the center point between the two sources at the phantom surface – the surface dose rate was 28.43%, 64.08%, 91.99%, and 99.47% of the maximum surface dose rate for TSDs: 0.0 cm, 0.1 cm, 0.2 cm, and 0.3 cm; respectively. At 50% of the maximum dose and for x = 0.0 cm, the maximum width of each profile was 0.66 cm, 0.79 cm, 0.92 cm, and 1.04 cm for TSDs: 0.01 cm, 0.1 cm, 0.2 cm, and 0.3 cm; respectively.

5.5 Discussion

In this chapter, the CSBT tip-source-rod assembly was more fully characterized. Figures 5.1 and 5.2 demonstrate how radiation penetration increased as a source was moved further away from the irradiated material. This effect is a fundamental consequence of radiation divergence. As the source was moved further from the phantom, the dose rate at the surface and at depth each decreased. The dose rate at the surface, however, decreased more rapidly.

It was shown that, unsurprisingly, the widths of the planar dose distributions were highly sensitive to the TSD. By moving the distal end of the source tip from 0 cm to 0.2 cm from the surface of the ROI, the dose distribution's width approximately doubled. As the source was moved further from the surface, the increase of the distribution width diminished. For example, when the source was moved from 0.2 cm to 0.4 cm from the surface, the distribution's width only increased by approximately 50%. The maximum dose rate was also very sensitive to the TSD and decreased with increased TSD. Increasing the TSD from 0 cm to 0.2 cm and from 0.2 cm to 0.4 cm decreased the maximum dose rate by approximately 85% and 67%, respectively. The effect that the source holder tip had on the dose distribution with a TSD of 0 cm was also examined. Due to the tip's design, the region of the surface ROI that was exposed to a dose greater than 40% of the maximum was unaffected by the tip material. In the region of less than 40% of the maximum dose, the tip had the effect of increasing the width of the distribution. While this effect was small, it was beneficial in that it improved the homogeneity of multi-source distributions.

By taking advantage of the high dependence of distribution width and dose rate, it was possible to improve the dose homogeneity for a hypothetical, irregularly shaped treatment target. The highest level of control over the distribution occurred when the source, the TSD, and relative activity were variable quantities. In simulation, adjusting the activities of the sources was a simple task. In reality, such a task would be complicated by the fact that, unless each source were activated together and had the same initial activity, uncertainties in the activation process would propagate to uncertainties in the dose rate distribution. For this work, the optimization process was one of subjective trial and error. This problem would be better suited to reverse planning optimization, where the planner defines the parameters and a desired spatial dose distribution and a computer is used to determine the optimal source configuration.

Chapter 6

MURINE MODEL DOSE ESCALATION STUDY

6.1 Introduction

The mechanisms of radiation-induced skin damage are similar between mice and humans, and, in radiation therapy, mice provide excellent models for human radiation dermatitis [116,117]. Further, tumor regression in mice has been shown following treatment with β^- particles [77,113].

This chapter presents an examination of the CSBT device's effectiveness at administering superficial radiation to living tissue and assesses the level to which the simulated dose distributions can predict histologic injury to skin. To achieve that goal, a dose-escalation study was performed in non-tumor-bearing, SKH-1 mice [118]. The specific aim of this work was to determine an appropriate administration dose for future tumor-murine model studies of the CSBT device and to examine the temporal association between administered radiation and resulting histologic injury.

6.2 Materials and Methods

6.2.1 CSBT Device

The CSBT device was used to administer ^{90}Y β- radiation doses to living tissue targets in mice. Two different source holder tips were used. One of the tip types was the same as what was used for the remainder of this work and was described in section 3.1 of this thesis. Those tips were termed “Tip-0.5mm” because the source-to-surface distance was roughly 0.5 mm. During the course of the experiment, it was discovered that the source activities would not allow for administrated dose within the allowable treatment time. The tips were modified to reduce the tip-to-surface distance to zero in order to increase the dose rate. Those modified tips were termed “Tip-surface”. Figure 6.1 shows the treatment end of the device with the modified tips. For each exposure, the distal tips were placed in light contact with the target surfaces. A single layer of polyethylene food wrap was placed

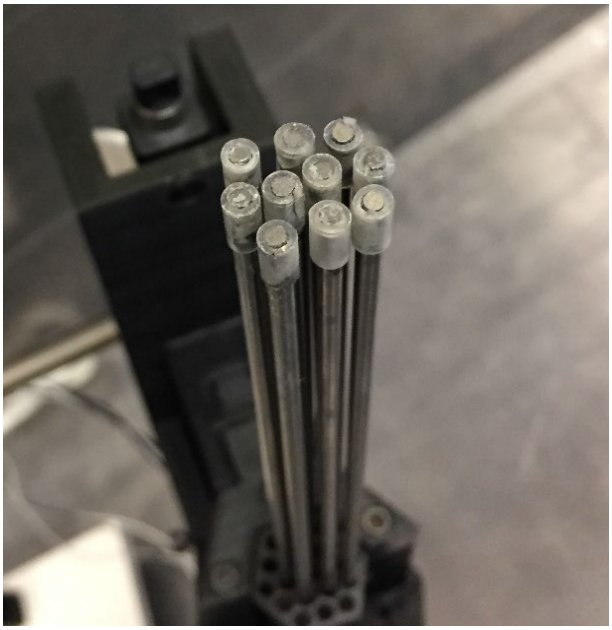

Figure 6.1. Picture of the distal (treatment) end of the CSBT device with 10 ^{90}Y sources and the modified tips (Tip-surface).

between the sources and the target surfaces to prevent potential contamination. It was assumed that the thin polyethylene did not effect on the administered dose.

During treatment, the CSBT device was mounted on a system that allowed precise linear movement of the device in three dimensions. At the start of exposure, the entire mounting system was moved by hand so that the CSBT device was vertically oriented and located directly above the treatment target (~2 cm). The mounting system was then used to lower the CSBT device to its treatment position. Once the sources were in contact with the target surface, the timer was initiated. It took roughly 2 seconds to move the entire mounting system and roughly 2 seconds to lower the CSBT device. The mounting system was lifted up and away from the treated target to end the exposures.

6.2.2 Pre-Experiment Quality Assurance

In preparation for the quality assurance and dose rate measurements performed for this study, an additional EBT3 film calibration curve was obtained for a film development period of two hours. This allowed for dose rate measurements to be rapidly performed in the morning before each experiment.

Roughly 24 hours preceding the first mouse exposure, source constancy measurements were performed with film for each of the ten sources. One source was also chosen at random and its dose rate was measured three times total. To perform each measurement, a cut piece of EBT3 film (10.2 cm × 6.4 cm) was placed beneath a 1 mm thick slab of SW and above a 5 cm thick slab of SW. For 90 seconds, the source was placed directly on the 1 mm thick slab of SW and directly above the piece of film. Following exposure, each piece of film was allowed a two-hour development period before being processed according to the procedure outlined in section 3.2.1. The relative dose rates of each source were assessed.

On the morning of the first mouse treatment, each of the ten sources was loaded in the CSBT device with the unmodified tips. To determine the maximum dose rate of the ten-source CSBT device, a film-based measurement was performed by placing a cut piece of film on SW and placing the device's distal end directly on the film for 60 seconds. Following the two-hour development period, the dose rate ($\dot{D}$) was determined, which allowed for the calculation of each mouse treatment time (T) for each prescribed dose (D) according to

$$T = D/\dot{D} \tag{6.1}$$

The date and time of the initial film-based dose rate measurement were recorded, and the change of dose rate due to source decay was accounted for. The change in activity during each treatment was not accounted for.

6.2.3 Animal Preparation

Hairless SKH-1 mice (n = 20) were obtained. The treated mice were randomly separated into four groups of four, with each group slated to receive 30, 40, 50, or 60 Gy maximum dose to the surface of the skin. The remaining four mice served as controls or as backups if the death of any of the treated mice occurred during anesthesia and treatment. Each mouse was sedated with ketamine/xylazine intraperitoneally and immobilized for treatment. The maximum treatment time was limited to 15 minutes to minimize complications during anesthesia. A 2 cm region on the left hip/hindlimb was delineated as the target and was positioned so that it was flat, allowing each tip to contact the skin when the CSBT device was vertically oriented.

6.2.4 Monitoring of Mice and Collection of Skin Samples

Following irradiation, daily monitoring for the development of dermatitis was performed. Skin toxicity was graded according to a modified VRTOG toxicity scheme

Table 6.1. Modified VRTOG acute skin toxicity scoring criteria

Grade	Description
0	no change over baseline
1	follicular, faint or dull erythema, epilation, dry desquamation
2	tender or bright erythema, patchy moist desquamation, moderate edema
3	confluent moist desquamation (not in skin folds), pitting edema
4	ulceration, hemorrhage, necrosis
5	death

(Table 6.1). At the appearance of peak grade 4 toxicity in the 60 Gy mice, each mouse was humanely euthanized per American Veterinary Medical Association standards, in order to standardize the timepoint of skin injury. Following euthanasia, irradiated skin was promptly collected and placed in formalin to inhibit putrefaction and autolysis in the samples. The samples were then prepared for future histologic examination by being dissected into 4 mm thick cross-sectional serial slices and then placed in 75% ethanol prior to being paraffin-embedded for sectioning.

6.3 Results

Table 6.2 shows the resulting mouse irradiation schedule. During the experiment, three mice died of complications associated with the sedative. Each deceased mouse was from the 50 Gy group and was replaced and two mice were reserved for control, hence the 30 Gy group having only three mice.

Initial quality assurance measurements were performed to assess individual source activities and dose delivered per source at the surface. The mean measured activity on the day the sources were received was 6.8×10^7 Bq (1.8 mCi). The mean dose rate was 22.4 cGy/s at the surface and 4.5 cGy/s at $d = 0.1$ cm. The standard deviation of the relative activity between all ten sources was 1.3%. Modifying the tips decreased the source-to-

surface distance by 0.5 mm to 0 mm. As a result, the maximum dose rate at the surface increased by 87%. Figure 6.2 shows the MC simulated relative surface dose profiles for Tip-0.5mm and Tip-surface. For a single source, the full-width-half-maximum of Tip-surface was 12% lower than Tip-0.5mm. For two sources, the relative surface dose rate halfway between the sources decreased by 35%.

Table 6.2. Mouse irradiation schedule

	Group/ Number	Target Dose (Gy)	CSBT Tip	Dose Rate (Gy/min)	Exposure Duration (min:sec)	Comment
	control	0				
	control	0				
DAY 1	G60/1	60	Tip-0.5mm	4.33	13:52	
	G60/2	60	Tip-0.5mm	4.31	13:55	
	G60/3	60	Tip-0.5mm	4.29	13:58	
	G60/4	60	Tip-0.5mm	4.28	14:01	
	G50/1	50	Tip-0.5mm	4.27	11:43	
	G50/*	50	Tip-0.5mm	4.25	11:45	Died following irradiation
	G50/2	50	Tip-0.5mm	4.24	11:47	
	G50/3*	50	Tip-0.5mm	4.20	11:54	Died overnight
	G50/4*	50	Tip-0.5mm	4.21	11:52	Died overnight
DAY 2	G50/3	50	Tip-surface	8.92	5:36	
	G50/4	50	Tip-surface	8.90	5:37	
	G40/1	40	Tip-surface	8.88	4:30	
	G40/2	40	Tip-surface	8.87	4:30	
	G40/3	40	Tip-surface	8.82	4:32	
	G40/4	40	Tip-surface	8.61	4:39	
	G30/1	30	Tip-surface	8.67	3:27	
	G30/2	30	Tip-surface	8.66	3:28	
	G30/3	30	Tip-surface	8.64	3:28	

Figure 6.3 shows the resulting surface dose rate distributions for ten sources from the pretreatment quality assurance measurements with Tip-0.5mm (Figure 6.3.a) and Tip-surface (Figure 6.3.b). The maximum surface dose rate measured on day one with Tip-0.5mm was 448 cGy/min, which, after accounting for source decay, corresponded to a mean treatment time of 13.9 minutes for the 60 Gy group and 11.8 minutes for the day one 50 Gy group. On day two, the measured maximum dose rate with Tip-surface was 917 cGy/min, which corresponded to mean treatment times of 5.6 minutes, 4.6 minutes, and 3.5 minutes for the day two 50 Gy group, the 40 Gy group, and the 30 Gy group, respectively.

Radiation-induced skin toxicity murine studies showed that the administration of β- particles to mouse skin resulted in dose-dependent induced dermatitis. Figure 6.4 shows the time course of radiation-induced skin dermatitis following exposure from the CSBT device. Figure 6.5 shows the modified VRTOG scores following exposure from the CSBT device. Mice irradiated to 30 Gy or 40 Gy presented with faint erythema on day nine and

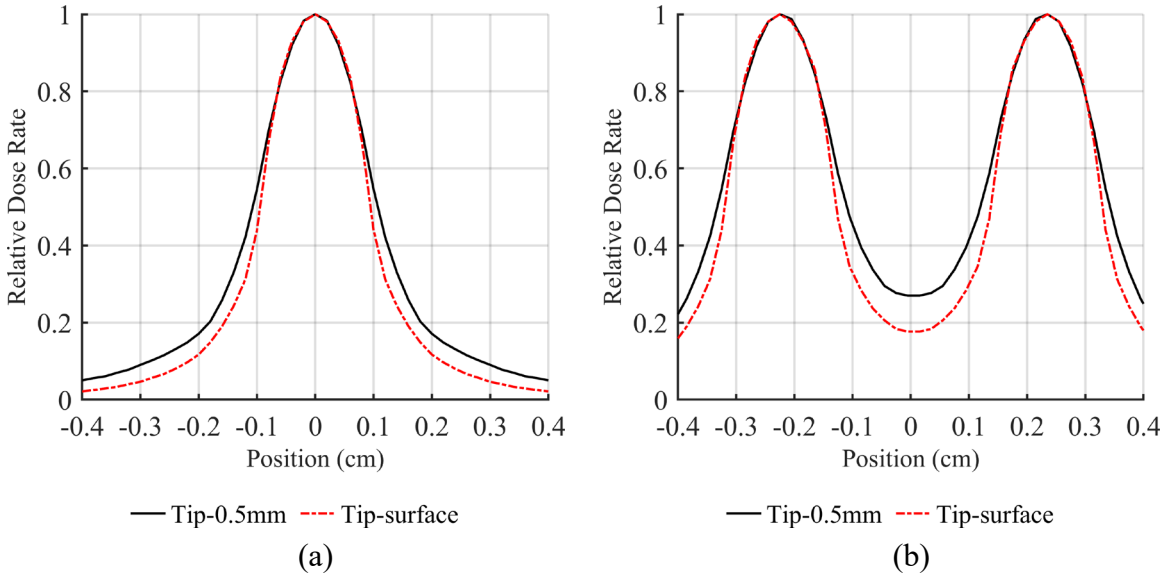

Figure 6.2. MC simulated relative surface dose profiles for Tip-0.5mm and Tip-surface. (a) Surface profiles from a single source. (b) Source profiles from two sources with a center-to-center spacing of 0.45 cm.

the toxicity did not progress in severity during the remainder of the experiment. Mice irradiated to 50 Gy from the CSBT device with Tip-surface presented with clinically observable dermatitis on day 8, and the score steadily increased to a peak of grade 2 on day 12. Mice irradiated with 50 Gy with Tip-0.5mm presented with grade 1 toxicity on day

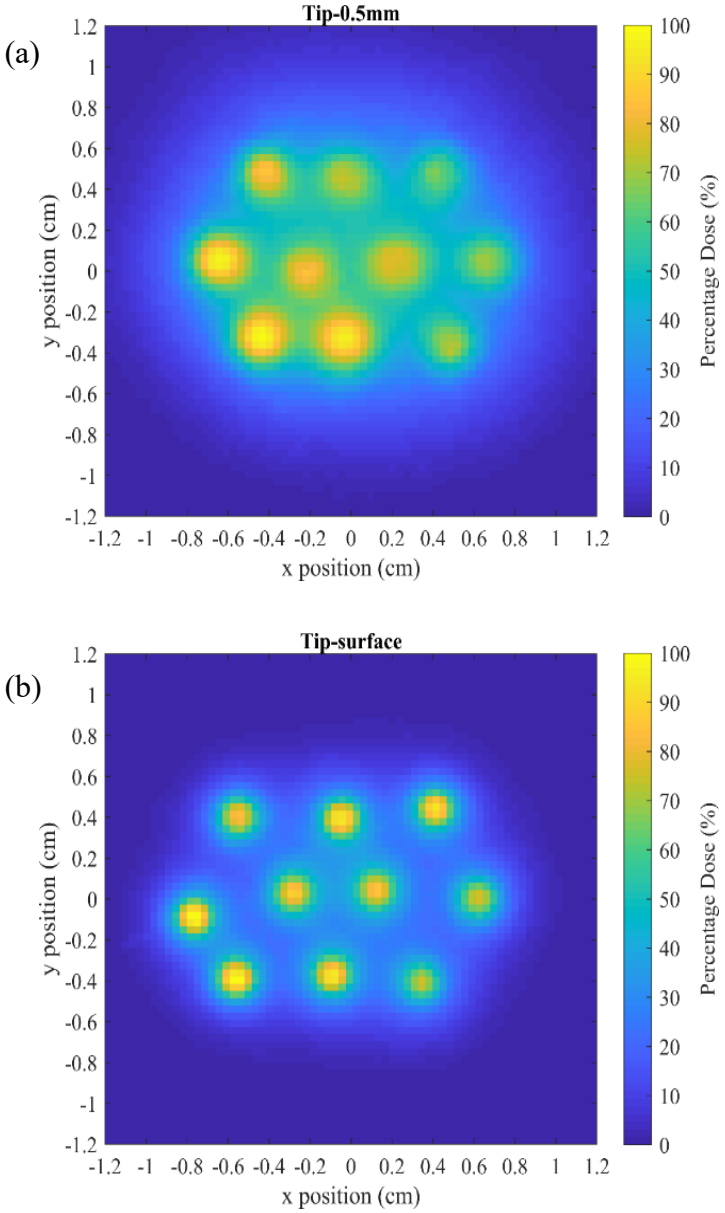

Figure 6.3. Pretreatment quality assurance CSBT film-based surface dose distributions: (a) standard tips (Tip-0.5mm) and (b) modified tips (Tip-surface).

nine and the mean toxicity score progressed to grade 3.5 by day 14. Finally, mice irradiated with 60 Gy presented with faint erythema on day 8, and toxicity progressed to grade 4 on day 14. When grade 4 toxicity was reached by the 60 Gy group, the experiment's grading portion was concluded and all mice were euthanized.

6.4 Discussion

This chapter presented the clinical results of the study of radiation-induced skin dermatitis in a murine model. Two source holder tip types were used. It was shown that the modified tip significantly increased the maximum dose rate at the skin surface. The

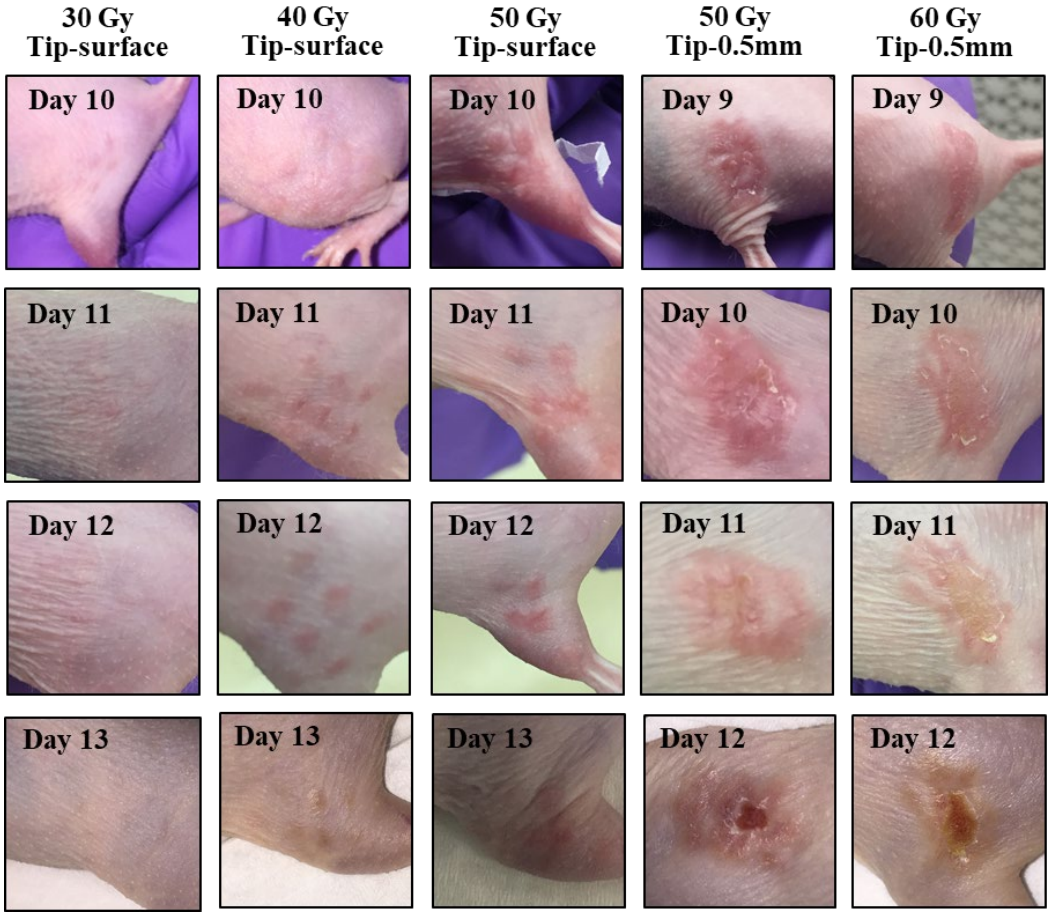

Figure 6.4. Time course of radiation-induced skin dermatitis following exposure from the ^{90}Y-based CSBT device.

increase in dose rate decreased the treatment times required to administer the prescribed doses. The modified tip also decreased the homogeneity of the 10-source dose distribution. As shown by the two 50 Gy groups in Figure 6.4, reducing the source-to-surface distance of each source – by using Tip-surface rather than Tip-0.5mm – reduced the device's effectiveness to induce homogeneous dermatitis. The tissue volume effect may explain this outcome. J. W. Hopewell has shown that decreasing the volume of pig skin exposed to β-radiation can drastically reduce acute toxicity [25]. With the unmodified tips (Tip-0.5mm), 50 Gy was a sufficient dose to induce grade 4 toxicity in SKH-1 mice. An increase to 60 Gy did not yield subjectively different severity of radiation-induced dermatitis.

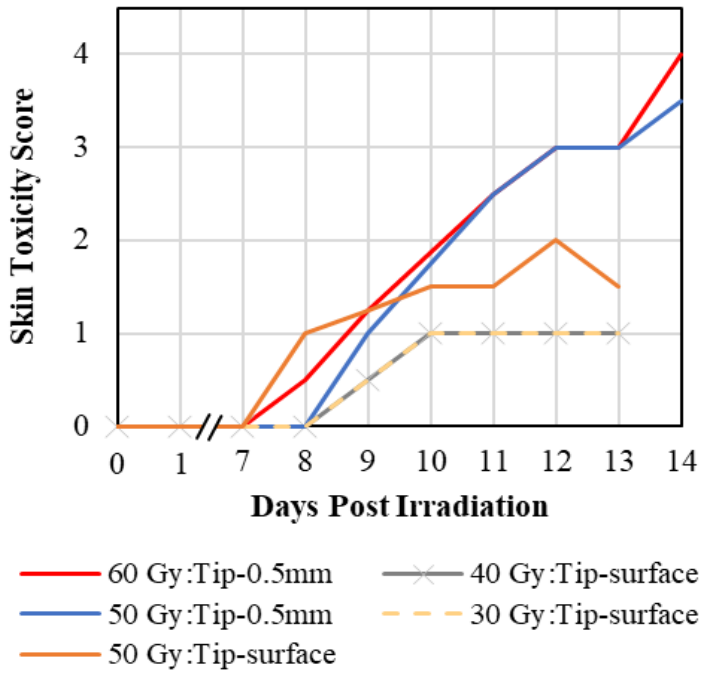

Figure 6.5. Mean skin toxicity scores (Modified VRTOG scheme) following exposure from the CSBT device.

Chapter 7

SUMMARY AND RECOMMENDATIONS FOR FUTURE WORK

7.1 Summary

The primary goal of this work was to examine the potential of the conformal superficial brachytherapy (CSBT) device as a clinical therapy option for the treatment of non-melanoma skin cancer (NMSC). The device was designed to limit exposure to healthy tissue, thereby reducing the chances for acute or long-term complications to arise. The CSBT device was also designed to provide the flexibility to deliver patient-specific treatments, giving the treatment specialist the ability to precisely tailor the planned dose to each lesion's unique characteristics. Three primary aims were outlined to determine CSBTs ability to achieve these benchmarks. The first aim was to characterize the base yttrium-90 (^{90}Y) beta radiation source. The second aim was to characterize the CSBT device with multiple sources. The third aim was to demonstrate the high dose gradient of the CSBT device by clinically defining radiation-induced dermatitis in a non-tumor murine model.

Placing the ^{90}Y source in the source holder tip significantly reduced the dose rate and did not have a significant effect on the penetration of the dose. The decrease in dose

rate was due to the source being lifted from the target surface. From a clinical perspective, the decrease in dose rate caused by the tip is of little consequence as adjusting the necessary source activity is a simple task. A less trivial outcome was the indication of how sensitive the dose rate was to the source-to-surface distance. The sensitivity of the dose rate on source-to-surface distance was further confirmed when it was shown in Section 5.1 that the maximum dose rate from one source could reduce by half if the source-to-surface distance was a millimeter too large or double if a millimeter too small. Managing this sensitivity may be done simply by only performing treatments with the distal end of the source holder tips in contact with the target surface

There is a benefit from the ability to alter the source-to-surface distances. By increasing the tip-to-surface distance (TSD), the increase in dose homogeneity would allow for deeper lesions to be treated. As shown in Figure 5.2.b, simply increasing the TSD from 0.0 cm to 0.4 cm increased the depth along the central axis that received 70% of the maximum dose by approximately 60%, while almost doubling the depth that received 50% of the maximum dose. That action would come at the cost of an increase in the required source activity or treatment time. It would also decrease the individual source dose gradient and increase the width of the dose distribution.

For multiple source exposures, the surface dose rate between the sources was increased by increasing the TSD of each source. By selectively manipulating the sources' TSDs, the resulting dose distribution was far more homogeneous than when each TSD was equal. Consequentially, the dose gradient at the periphery of the distribution increased, expanding the 50% isodose by roughly 0.17 cm for every millimeter of added TSD. It is, therefore, possible to finely manipulate the dose distribution as needed to cover irregularly shaped lesions while sparing healthy tissue. A balance between dose homogeneity and conformity will need to be optimized depending on the target lesion's exact shape, thus allowing for patient-specificity.

Selective manipulation of the activity and TSD of each source yielded the highest level of control over the dose distributions. While adjusting the TSDs resulted in far more homogeneous dose distributions, adjusting the activities as well was more effective for making fine adjustments to the shape of the distributions. This method of adjusting the activities and TSDs would provide the most conformal and homogeneous dose distributions, but because of the nature of radioactive decay, treating various activities would likely be overly complicated.

Maintaining a limit of the source-to-surface distance imposed by source holder tips at 0.05 cm, rather than 0 cm, induced a more homogeneous distribution of dermatitis in the murine model. When using the tips with a source-to-surface distance of 0 cm (Tip-surface), the appearance of dermatitis was spatially periodic, corresponding to the locations of the distal end of the sources during exposure. This periodic effect was not seen when the tips with a source-to-surface distance of 0.5 mm (Tip-0.5mm) were used. It is recommended that Tip-0.5mm is the superior design. Using Tip-0.5mm, the shapes of radiation-induced dermatitis corresponded to the positions of the distal ends of the sources. The ability to conform dose distributions to target lesions is necessary to administer doses to diseased tissue while sparing healthy tissue.

As patient throughput in radiation therapy clinics is of constant concern, a device capable of quickly and simply treating skin lesions with high dose conformity would benefit the clinic and the patients. This study provided the proof of principle that the CSBT device can provide conformal treatments, thus warranting continued investigation. Characterization of the ^{90}Y CSBT source showed that it was possible to theoretically administer a therapeutic conformal dose *in vivo*. The next logical step is to perform a histologic examination of treated living tissue in a non-tumor murine model and to examine the device's ability to reduce tumor size in a tumor murine model.

BIBLIOGRAPHY

[1] American Cancer Society I. American Cancer Society. Cancer Facts & Figures 2018. Atlanta: American Cancer Society; 2018. BMJ 2018;309:1689. https://doi.org/10.1136/bmj.309.6970.1689.

[2] Rogers HW, Weinstock MA, Feldman SR, Coldiron BM. Incidence Estimate of Nonmelanoma Skin Cancer (Keratinocyte Carcinomas) in the US Population, 2012. JAMA Dermatology 2015;151:1081–6. https://doi.org/10.1001/jamadermatol.2015.1187.

[3] Dubas LE, Ingraffea A. Nonmelanoma Skin Cancer. Facial Plast Surg Clin NA 2013;21:43–53. https://doi.org/10.1016/j.fsc.2012.10.003.

[4] Fahradyan A, Howell A, Wolfswinkel E, Tsuha M, Sheth P, Wong A. Updates on the Management of Non-Melanoma Skin Cancer (NMSC). Healthcare 2017;5:82. https://doi.org/10.3390/healthcare5040082.

[5] Apalla Z, Lallas A, Sotiriou E, Lazaridou E, Ioannides D. Epidemiological trends in skin cancer. Dermatol Pract Concept 2017;7:1–6. https://doi.org/10.5826/dpc.0702a01.

[6] Fuchs A, Marmur E. The kinetics of skin cancer: Progression of actinic keratosis to squamous cell carcinoma. Dermatologic Surg 2007;33:1099–101. https://doi.org/10.1111/j.1524-4725.2007.33224.x.

[7] Bhatnagar A. Nonmelanoma skin cancer treated with electronic brachytherapy: Results at 1 year. Brachytherapy 2013;12:134–40. https://doi.org/10.1016/j.brachy.2012.08.003.

[8] Simões MCF, Sousa JJS, Pais AACC. Skin cancer and new treatment perspectives: A review. Cancer Lett 2015;357:8–42. https://doi.org/10.1016/j.canlet.2014.11.001.

[9] Van Loo E, Mosterd K, Krekels GAM, Roozeboom MH, Ostertag JU, Dirksen CD, et al. Surgical excision versus Mohs' micrographic surgery for basal cell carcinoma of the face: A randomised clinical trial with 10 year follow-up. Eur J Cancer

2014;50:3011–20. https://doi.org/10.1016/j.ejca.2014.08.018.

[10] Patel R, Strimling R, Doggett S, Willoughby M, Miller K, Dardick L, et al. Comparison of electronic brachytherapy and Mohs micrographic surgery for the treatment of early-stage non-melanoma skin cancer: a matched pair cohort study. J Contemp Brachytherapy 2017;9:338–44. https://doi.org/10.5114/jcb.2017.68480.

[11] Kauvar ANB, Cronin T, Roenigk R, Hruza G, Bennett R. Consensus for nonmelanoma skin cancer treatment: Basal cell carcinoma, including a cost analysis of treatment methods. Dermatologic Surg 2015;41:550–71. https://doi.org/10.1097/DSS.0000000000000296.

[12] Van Hezewijk M, Creutzberg CL, Putter H, Chin A, Schneider I, Hoogeveen M, et al. Efficacy of a hypofractionated schedule in electron beam radiotherapy for epithelial skin cancer: Analysis of 434 cases. Radiother Oncol 2010;95:245–9. https://doi.org/10.1016/j.radonc.2010.02.024.

[13] Ota K, Adar T, Dover L, Khachemoune A. Review: the reemergence of brachytherapy as treatment for non-melanoma skin cancer. J Dermatolog Treat 2018;29:170–5. https://doi.org/10.1080/09546634.2017.1341617.

[14] Delishaj D, Rembielak A, Manfredi B, Ursino S, Pasqualetti F, Laliscia C, et al. Non-melanoma skin cancer treated with high-dose-rate brachytherapy: A review of literature. J Contemp Brachytherapy 2016;8:533–40. https://doi.org/10.5114/jcb.2016.64112.

[15] Paravati AJ, Hawkins PG, Martin AN, Mansy G, Rahn DA, Advani SJ, et al. Clinical and cosmetic outcomes in patients treated with high-dose-rate electronic brachytherapy for nonmelanoma skin cancer. Pract Radiat Oncol 2015;5:e659–64. https://doi.org/10.1016/j.prro.2015.07.002.

[16] Gerbi BJ, Antolak JA, Deibel FC, Followill DS, Herman MG, Higgins PD, et al. TG-70: Recommendations for clinical electron beam dosimetry: Supplement to the recommendations of Task Group 25. Med Phys 2009;36:3239–79. https://doi.org/10.1118/1.3125820.

[17] Chmura J, Erdman A, Ehler E, Lawrence J, Wilke CT, Rogers B, et al. Novel design and development of a 3D- printed conformal superficial brachytherapy device for the treatment of non-melanoma skin cancer and keloids. 3D Print Med 2019;5:1–6. https://doi.org/10.1186/s41205-019-0045-z.

[18] Ferreira C, Johnson D, Rasmussen K, Leinweber C, Ahmad S, Jung JW. A novel conformal superficial high-dose-rate brachytherapy device for the treatment of nonmelanoma skin cancer and keloids. Brachytherapy 2017;16:215–22. https://doi.org/10.1016/j.brachy.2016.09.002.

[19] Rogers B, Lawrence J, Chmura J, Ehler E, Ferreira C. Dosimetric characterization of a novel 90Y source for use in the conformal superficial brachytherapy device. Phys Medica 2020;72:52–9. https://doi.org/10.1016/j.ejmp.2020.03.002.

[20] Hall EJ, Giaccia AJ. Radiobiology for the Radiologist. 7th ed. Philadelphia: Wolters Kluwer Health/Lippincott Williams & Wilkins; 2012.

[21] ICRP. The Biological Basis for Dose Limitation in the Skin. ICRP Publ 59 Ann 1992;ICRP 22.

[22] Cross WG, Böhm J, Charles M, Piesch E, Seltzer SM, Cross, W. G.; Böhm, J.; Piesch, E.; Seltzer SM, et al. ICRU Report 56: Dosimetry of External Beta Rays for Radiation Protection. J Int Comm Radiat Units Meas 1997;os29:NP-NP. https://doi.org/10.1093.

[23] ICRP. The 2007 Recommendations of the International Commission on Radiological Protection. ICRP Publication 103. 2007.

[24] Shore RE. Overview of Radiation-induced Skin Cancer in Humans. Int J Radiat Biol 1990;57:809–27. https://doi.org/10.1080/09553009014550951.

[25] Hopewell JW. The Skin: Its Structure and Response to Ionizing Radiation. Int J Radiat Biol 1990;57:751–73. https://doi.org/10.1080/09553009014550911.

[26] Cox JD, Stetz J, Pajak TF. Toxicity Criteria of the Radiation Therapy Oncology Group (RTOG) and the European Organization for Research and Treatment of Cancer (EORTC). Int J Radiat Oncol Biol Phys 1995;31:1341–6.

[27] Gershenwald JE, Scolyer RA, Hess KR, Faries MB, Kirkwood JM, Mcarthur GA. Melanoma Staging: Evidence-Based Changes in the American Joint Committee on Cancer Eighth Edition Cancer Staging Manual. CA Cancer J Clin 2017;67:472–92. https://doi.org/10.3322/caac.21409.

[28] Amin MB, Edge S, Greene F, Byrd DR, Brookland RK, Washington MK, et al., editors. AJCC Cancer Staging Manual. Springer International Publishing; 2017.

[29] von Domarus H v., Stevens PJ. Metastatic basal cell carcinoma: Report of five cases and review of 170 cases in the literature. J Am Acad Dermatol 1984;10:1043–60. https://doi.org/10.1016/S0190-9622(84)80334-5.

[30] Nguyen-Nielsen M, Wang L, Pedersen L, Olesen AB, Hou J, Mackey H, et al. The incidence of metastatic basal cell carcinoma (mBCC) in Denmark, 1997-2010. Eur J Dermatology 2015;25:463–8. https://doi.org/10.1684/ejd.2015.2546.

[31] Snow SN, Sahl W, Lo JS, Mohs FE, Warner T, Dekkinga JA, et al. Metastatic basal cell carcinoma. Report of five cases. Cancer 1994;73:328–35. https://doi.org/10.1002/1097-0142(19940115)73:2<328::AID-CNCR2820730216>3.0.CO;2-U.

[32] NCCN Clinical Practice Guidelines in Oncology. Basal Cell Skin Cancer, Version 1.2019 2015.

[33] Laurence J, Astrint SM, Astrin SM, Astrint SM. Human immunodeficiency virus induction of malignant transformation in human B lymphocytes. Proc Natl Acad Sci U S A 1991;88:7635–9. https://doi.org/10.1073/pnas.88.17.7635.

[34] Perez C, Kavanagh B. Uterine cervix. Princ. Pract. Radiat. Oncol. 4th ed., Philadelphia: Lippincott Williams & Wilkins; n.d.

[35] Bordea C, Wojnarowska F, Millard PR, Doll H, Welsh K, Morris PJ. Skin cancers in renal-transplant recipients occur more frequently than previously recognized in a temperate climate. Transplantation 2004;77:574–9. https://doi.org/10.1097/01.TP.0000108491.62935.DF.

[36] Rubió-Casadevall J, Hernandez-Pujol A, Ferreira-Santos M, Morey-Esteve G, Vilardell L, Osca-Gelis G, et al. Trends in incidence and survival analysis in non-melanoma skin cancer from 1994 to 2012 in Girona, Spain: A population-based

study. Cancer Epidemiol 2016;45:6–1. https://doi.org/10.1016/j.canep.2016.09.001.
[37] Schmults C, Karia P, Carter J, Han J, Qureshi A. Factors predictive of recurrence and death from cutaneous squamous cell carcinoma: a 10-year, single-institution cohort study. JAMA Dermatology 2013;149:541–7. https://doi.org/10.1001/jamadermatol.2013.2139.
[38] Eisemann N, Jansen L, Castro F, Chen T, Eberle A, Nennecke A, et al. Survival with nonmelanoma skin cancer in Germany. Br J Dermatol 2016;174:778–85. https://doi.org/10.1111/bjd.14352.
[39] NCCN Clinical Practice Guidelines in Oncology. Squamous Cell Skin Cancer, Version 1.2020 2019.
[40] Rowe D, Carroll R, Day CJ. Prognostic factors for local recurrence, metastasis, and survival rates in squamous cell carcinoma of the skin, ear, and lip. Implications for treatment modality selection. J Am Acad Dermatology1 1992;26:976–90.
[41] Hernández-Machin B, Borrego L, Gil-García M, Hernández B. Office-based radiation therapy for cutaneous carcinoma: evaluation of 710 treatments. Int J Dermatol 2007;46:453–9.
[42] Schulte K, Lippold A, Auras C, Bramkamp G, Breitkopf C, Elsmann H, et al. Soft x-ray therapy for cutaneous basal cell and squamous cell carcinomas. J Am Acad Dermatol 2005;53:993–1001.
[43] Marconi DG, Resende C, Rauber E, Cassia P De, Fernandes JM, Mehta N, et al. Head and Neck Non-Melanoma Skin Cancer Treated By Superficial X-Ray Therapy: An Analysis of 1021 Cases. PLoS One 2016;11:1–9. https://doi.org/10.1371/journal.pone.0156544.
[44] Cognetta A, Howard B, Heaton H, Stoddard E, Hong H, Green W. Superficial x-ray in the treatment of basal and squamous cell carcinomas: a viable option in select patients. J Am Acad Dermatol 2012;67:1235–41.
[45] Barlow J, Zalla M, Kyle A, DiCaudo D, Lim K, Yiannias J. Treatment of basal cell carcinoma with curettage alone. JAAD 2006;54:1039–45.
[46] Thissen M, Neumann M, Schouten L. A systematic review of treatment modalities for primary basal cell carcinomas. Arch Dermatol 1999;135:1177–83.
[47] Honeycutt W, Jansen G. Treatment of squamous cell carcinoma of the skin. Arch Dermatol 1973;108:670–2.
[48] Shiffman N. Squamous cell carcinomas of the skin of the pinna. Can J Surg 1975;18:279–83.
[49] Rowe D, Carroll R, Day CJ. Long-term recurrence rates in previously untreated (primary) basal cell carcinoma: implications for patient follow-up. J Dermatol Surg Oncol 1989;15:315–28.
[50] Kuijpers D, Thissen M, Berretty P, Ideler F, Nelemans P, Neumann M. Surgical excision versus curettage plus cryosurgery in the treatment of basal cell carcinoma. Dermatologic Surg 2007;33:579–87.
[51] Rhodes L, de Rie M, Leifsdottir R, Yu R, Bachmann I, Goulden V, et al. Five-year follow-up of a randomized, prospective trial of topical methyl aminolevulinate photodynamic therapy vs surgery for nodular basal cell carcinoma. Arch Dermatol

2007;143:1131–6.
[52] Griffiths R, Feeley K, Suvarna S. Audit of clinical and histological prognostic factors in primary invasive squamous cell carcinoma of the skin: assessment in a minimum 5 year follow-up study after conventional excisional surgery. Br J Plast Surg 2002;55:287–92.
[53] Bath-Hextall F, Ozolins M, Armstrong S, Colver G, Perkins W, Miller P, et al. Surgical excision versus imiquimod 5% cream for nodular and superficial basal-cell carcinoma (SINS): a multicentre, non-inferiority, randomised controlled trial. Lancet Oncol 2014;15:96–105. https://doi.org/10.1016/S1470-2045(13)70530-8.
[54] Yanaginda T. 2018 Varian: A "Brave New World" in Science. Seibutsu Butsuri 2010;50:116–7. https://doi.org/10.2142/biophys.50.116.
[55] Guide U. 2017 elekta brachytherapy applicators and accessories. October 1995;1.
[56] Pérez-Calatayud J, Granero D, Ballester F, Puchades V, Casal E, Soriano A, et al. A dosimetric study of Leipzig applicators. Int J Radiat Oncol Biol Phys 2005;62:579–84. https://doi.org/10.1016/j.ijrobp.2005.02.028.
[57] Evans MDC, Yassa M, Podgorsak EB, Roman TN, Schreiner LJ, Souhami L. Surface applicators for high dose rate brachytherapy in aids-related Kaposi's sarcoma. Int J Radiat Oncol 1997;39:769–74. https://doi.org/10.1016/S0360-3016(97)00360-X.
[58] Likhacheva AO, Devlin PM, Shirvani SM, Barker CA, Beron P, Bhatnagar A, et al. Skin surface brachytherapy: A survey of contemporary practice patterns. Brachytherapy 2017;16:223–9. https://doi.org/10.1016/j.brachy.2016.10.006.
[59] Granero D, Perez-Calatayud J, Ballester F, Ouhib Z. Radiation leakage study for the Valencia applicators. Phys Medica 2013;29:60–4. https://doi.org/10.1016/j.ejmp.2011.11.006.
[60] Vijande J, Candela-Juan C, Niatsetski Y, Van der Laarse R, Granero D, Ballester F, et al. EP-1992: Design and characterization of a new HDR brachytherapy Valencia applicator for larger skin lesions. Radiother Oncol 2016;119:S942–3. https://doi.org/10.1016/s0167-8140(16)33243-1.
[61] Kubo HD, Glasgow GP, Pethel TD, Thomadsen BR, Williamson JF. High dose-rate brachytherapy treatment delivery: Report of the AAPM Radiation Therapy Committee Task Group No. 59. Med Phys 1998;25:375–403. https://doi.org/10.1118/1.598232.
[62] Pérez-Calatayud J, Granero D, Ballester F, Crispín V, Van Der Laarse R. Technique for routine output verification of Leipzig applicators with a well chamber. Med Phys 2006;33:16–20. https://doi.org/10.1118/1.2138008.
[63] Standard Imaging [Brochure]. HDR 1000 Plus Well Chamber. 2008.
[64] Dinsmore M, Harte KJ, Sliski AP, Smith DO, Nomikos PM, Dalterio MJ, et al. A new miniature x-ray source for interstitial radiosurgery: Device description. Med Phys 1996;23:45–52. https://doi.org/10.1118/1.597790.
[65] Ramachandran P. New era of electronic brachytherapy. World J Radiol 2017;9:148. https://doi.org/10.4329/wjr.v9.i4.148.
[66] Kasper ME, Chaudhary AA. Novel treatment options for nonmelanoma skin cancer:

Focus on electronic brachytherapy. Med Devices Evid Res 2015;8:493–502. https://doi.org/10.2147/MDER.S61585.

[67] Rong Y, Welsh JS. Surface applicator calibration and commissioning of an electronic brachytherapy system for nonmelanoma skin cancer treatment. Med Phys 2010;37:5509–17. https://doi.org/10.1118/1.3489379.

[68] Rong Y, S. J. New Technology in High-Dose-Rate Brachytherapy with Surface Applicators for Non-Melanoma Skin Cancer Treatment: Electronic Miniature X-Ray Brachytherapy. Ski. Cancer Overv., InTech; 2012. https://doi.org/10.5772/25472.

[69] Eaton DJ. Electronic brachytherapy—current status and future directions. Br J Radiol 2015;88. https://doi.org/10.1259/bjr.20150002.

[70] Goubert M, Parent L. Dosimetric characterization of INTRABEAM® miniature accelerator flat and surface applicators for dermatologic applications. Phys Medica 2015;31:224–32. https://doi.org/10.1016/j.ejmp.2015.01.009.

[71] Valdes-Cortez C, Niatsetski Y, Perez-Calatayud J, Ballester F, Vijande J. A Monte Carlo-based dosimetric characterization of Esteya® , an electronic surface brachytherapy unit. Med Phys 2019;46:356–69. https://doi.org/10.1002/mp.13275.

[72] Rong Y, Zou L, Bazan JG. Radiotherapy treatment for nonmelanoma skin cancer. Expert Rev Anticancer Ther n.d. https://doi.org/10.1586/14737140.2015.1042865.

[73] Sheu RD, Powers A, Lo YC. Commissioning a 50-100 kV X-ray unit for skin cancer treatment. J Appl Clin Med Phys 2015;16:161–74. https://doi.org/10.1120/jacmp.v16i2.5182.

[74] Olek D, El-Ghamry MN, Deb N, Thawani N, Shaver C, Mutyala S. Custom mold applicator high-dose-rate brachytherapy for nonmelanoma skin cancer—An analysis of 273 lesions. Brachytherapy 2018;17:601–8. https://doi.org/10.1016/j.brachy.2018.01.002.

[75] Guix B, Finestres F, Tello JI, Palma C, Martinez A, Guix JR, et al. Treatment of skin carcinomas of the face by high-dose-rate brachytherapy and custom-made surface molds. Int J Radiat Oncol Biol Phys 2000;47:95–102. https://doi.org/10.1016/S0360-3016(99)00547-7.

[76] Park SY, Kang S, Park JM, An HJ, Oh DH, Kim J in. Development and dosimetric assessment of a patient-specific elastic skin applicator for high-dose-rate brachytherapy. Brachytherapy 2019;18:224–32. https://doi.org/10.1016/j.brachy.2018.11.001.

[77] Mukherjee A, Pandey U, SARMA HD, Pillai MRA, VENKATESH M. Preparation and evaluation of Y skin patches for therapy of superficial tumours in mice. Nucl Med Commun 2002;23:243–7. https://doi.org/10.1097/00006231-200203000-00007.

[78] Salgueiro MJ, Duran H, Palmieri M, Pirchio R, Medina V, Ughetti R, et al. Bioevaluation of 32P patch designed for the treatment of skin diseases. Nucl Med Biol 2008;35:233–7. https://doi.org/10.1016/j.nucmedbio.2007.08.004.

[79] Saxena SK, Kumar Y, Shaikh SH, Pandey U, Kumar SA, Dash A. Preparation of Radioactive Skin Patches Using Polyhydroxamic Acid-Grafted Cellulose Films

Toward Applications in Treatment of Superficial Tumors. Cancer Biother Radiopharm 2017;32:364–70. https://doi.org/10.1089/cbr.2017.2362.

[80] Koneru B, Shi Y, Munaweera I, Wight-Carter M, Kadara H, Yuan H, et al. Radiotherapeutic bandage for the treatment of squamous cell carcinoma of the skin. Nucl Med Biol 2016;43:333–8. https://doi.org/10.1016/j.nucmedbio.2016.02.010.

[81] Goodfellow M, Hayes A, Murphy S, Brealey M. A retrospective study of (90)Strontium plesiotherapy for feline squamous cell carcinoma of the nasal planum. J Feline Med Surg 2006;8:169–76. https://doi.org/10.1016/j.jfms.2005.12.003.

[82] Hammond GM, Gordon IK, Theon AP, Kent MS. Evaluation of strontium Sr 90 for the treatment of superficial squamous cell carcinoma of the nasal planum in cats: 49 cases (1990–2006). J Am Vet Med Assoc 2007;231:736–41. https://doi.org/10.2460/javma.231.5.736.

[83] Berlato D, Murphy S, Laberke S, Verganti S. Response, disease-free interval and overall survival of cats with nasal planum squamous cell carcinoma treated with a fractionated vs a single-dose protocol of strontium plesiotherapy. J Feline Med Surg 2019;21:306–13. https://doi.org/10.1177/1098612X18773913.

[84] Andrade AL De, Fernandes MAR, Sakamoto SS, Luvizotto MCR. Beta therapy with 90strontium as single modality therapy for canine squamous cell carcinoma in third eyelid. Ciência Rural 2015;45:1066–72. https://doi.org/10.1590/0103-8478cr20140918.

[85] Nath R, Amols H, Coffey C, Duggan D, Schell M, Soares C, et al. Intravascular brachytherapy physics : Report of the AAPM Radiation Therapy Committee Task Group No . 60. Med Phys 1999;26:119–52.

[86] Callens M, Crijns W, Simons V, De Wolf I, Depuydt T, Maes F, et al. A spectroscopic study of the chromatic properties of GafChromic^{TM} EBT3 films. Med Phys 2016;43:1156–66. https://doi.org/10.1118/1.4941312.

[87] Lewis D, Chan MF. Correcting lateral response artifacts from flatbed scanners for radiochromic film dosimetry. Med Phys 2015;42:416–29. https://doi.org/10.1118/1.4903758.

[88] Borca VC, Pasquino M, Russo G, Grosso P, Cante D, Sciacero P, et al. Dosimetric characterization and use of GAFCHROMIC EBT3 film for IMRT dose verification. J Appl Clin Med Phys 2013;14:158–71. https://doi.org/10.1120/jacmp.v14i2.4111.

[89] Niroomand-Rad A, Blackwell CR, Coursey BM, Gall KP, Galvin JM, McLaughlin WL, et al. Radiochromic film dosimetry: Recommendations of AAPM Radiation Therapy Committee Task Group 55. Med Phys 1998;25:2093–115. https://doi.org/10.1118/1.598407.

[90] Micke A, Lewis D, Yu X. Multi-Channel Film Dosimetry with Non-Uniformity Correction. Med Phys 2011;38:3410. https://doi.org/10.1118/1.3611636.

[91] Gafchromic radiotherapy films. Ashland, KY. Available from: www.gafchromic.com n.d.

[92] Chetty IJ, Curran B, Cygler JE, DeMarco JJ, Ezzell G, Faddegon BA, et al. Report of the AAPM Task Group No. 105: Issues associated with clinical implementation

of Monte Carlo-based photon and electron external beam treatment planning. Med Phys 2007;34:4818–53. https://doi.org/10.1118/1.2795842.

[93] Cross WG, Freedman NO, Wong PY. Tables of beta-ray dose distributions in water. At Energy Canada Limited, AECL 1992:1–107.

[94] Deufel CL, Courneyea LA, McLemore LB, Petersen IA. Experimental and theoretical dosimetry of the RIC-100 phosphorus-32 brachytherapy source for implant geometries encountered in the intraoperative setting. Brachytherapy 2015;14:734–50. https://doi.org/10.1016/j.brachy.2015.05.006.

[95] Loevinger R. The Dosimetry of Beta Sources in Tissue. The Point-Source Function. Radiology 1956. https://doi.org/10.1148/66.1.55.

[96] León Marroquin EY, Herrera González JA, Camacho López MA, Villarreal Barajas JE, García-Garduño OA, Marroquin EYL, et al. Evaluation of the uncertainty in an EBT3 film dosimetry system utilizing net optical density. J Appl Clin Med Phys 2016;17:466–81. https://doi.org/10.1120/jacmp.v17i5.6262.

[97] Cross WG. Variation of beta dose attenuation in different media. Phys Med Biol 1968;13:611–8. https://doi.org/10.1088/0031-9155/13/4/310.

[98] Sechopoulos I, Rogers DWO, Bazalova-Carter M, Bolch WE, Heath EC, McNitt-Gray MF, et al. RECORDS: Improved Reporting of montE CarlO RaDiation transport Studies: Report of the AAPM Research Committee Task Group 268. Med Phys 2018;45:e1–5. https://doi.org/10.1002/mp.12702.

[99] Rivard MJ, Coursey BM, DeWerd LA, Hanson WF, Huq MS, Ibbott GS, et al. TG-43U1: Update of AAPM Task Group No. 43 Report: A revised AAPM protocol for brachytherapy dose calculations. Med Phys 2004;31:633–74. https://doi.org/10.1118/1.1646040.

[100] X-5 Monte Carlo Team. MCNP - A General Monte Carlo N-Particle Transport Code, Version 5. LA-UR-03-1987 2008.

[101] ZZ MCNPDATA, Standard Neutron, Photon and Electron Data Libraries for MCNP-4C and MCB1C. Bibliographic information available from INIS: http://inis.iaea.org/search/search.aspx?orig_q=RN:43123833 Available on-line: http://www.nea.fr/abs/html/dlc-0200.html 2002.

[102] Hughes HG. Treating Electron Transport in MCNP LA-UR-96-4583, Los Alamos National Laboratory. Proc Train Course Use MCNP Radiat Prot Dosim 1996.

[103] Almond PR, Biggs PJ, Coursey BM, Hanson WF, Huq MS, Nath R, et al. AAPM's TG-51 protocol for clinical reference dosimetry of high-energy photon and electron beams. Med Phys 1999;26:1847–70. https://doi.org/10.1118/1.598691.

[104] Low DA, Harms WB, Mutic S, Purdy JA. A technique for the quantitative evaluation of dose distributions. Med Phys 1998;25:656–61. https://doi.org/10.1118/1.598248.

[105] Akbas U, Kesen ND, Koksal C, Okutan M, Demir B, Becerir HB. Surface dose measurement with Gafchromic EBT3 film for intensity modulated radiotherapy technique 2017;01011:7–9. https://doi.org/10.1051/epjconf/201715401011.

[106] Hansen JB, Culberson WS, DeWerd LA. Surface dose rate from a flat 106Ru/106Rh episcleral plaque measured with a planar windowless extrapolation chamber and un-laminated EBT3 film. Radiat Meas 2019;121:18–25.

https://doi.org/10.1016/j.radmeas.2018.12.002.
[107] Guinot JL, Rembielak A, Perez-Calatayud J, Rodríguez-Villalba S, Skowronek J, Tagliaferri L, et al. GEC-ESTRO ACROP recommendations in skin brachytherapy. Radiother Oncol 2018;126:377–85. https://doi.org/10.1016/j.radonc.2018.01.013.
[108] Garcia-Martinez T, Chan J-PP, Perez-Calatayud J, Ballester F. Dosimetric characteristics of a new unit for electronic skin brachytherapy. J Contemp Brachytherapy 2014;6:45–53. https://doi.org/10.5114/jcb.2014.40770.
[109] Gauden R, Pracy M, Avery AM, Hodgetts I, Gauden S. HDR brachytherapy for superficial non-melanoma skin cancers. J Med Imaging Radiat Oncol 2013;57:212–7. https://doi.org/10.1111/j.1754-9485.2012.02466.x.
[110] Grant-Kels JM, Vanbeek MJ. The ethical implications of "more than one way to skin a cat": Increasing use of radiation therapy to treat nonmelanoma skin cancers by dermatologists. J Am Acad Dermatol 2014;70:945–7. https://doi.org/10.1016/j.jaad.2014.01.849.
[111] Candela-Juan C, Niatsetski Y, van der Laarse R, Granero D, Ballester F, Perez-Calatayud J, et al. Design and characterization of a new high-dose-rate brachytherapy Valencia applicator for larger skin lesions. Med Phys 2016;43:1639–48. https://doi.org/10.1118/1.4943381.
[112] Granero D, Pérez-Calatayud J, Gimeno J, Ballester F, Casal E, Crispín V, et al. Design and evaluation of a HDR skin applicator with flattening filter. Med Phys 2008;35:495–503. https://doi.org/10.1118/1.2825622.
[113] Mukherjee A, Pandey U, Sarma HD, Gupta SK, Ingle AD, Pillai MRA, et al. Bioevaluation of radioactive bandages in a murine model of melanoma. Int J Radiat Biol 2003;79:839–45. https://doi.org/10.1080/09553000310001610989.
[114] Sedda A, Cipriani C, Carrozzo A. Dermatological Single-Session Beta Emitter Conformational Brachytherapy of Non-Melanocyte Skin Tumors. Brachytherapy Types, Dosing Side Eff., Nova Science Publishers; 2011, p. 73–88.
[115] Kirisits C, Rivard MJ, Baltas D, Ballester F, Brabandere M De, Laarse R Van Der, et al. Review of clinical brachytherapy uncertainties: analysis guidelines of GEC-ESTRO and the AAPM. Radiother Oncol 2014;110:199–212. https://doi.org/10.1016/j.radonc.2013.11.002.
[116] Phillips J, Moore-medlin T, Sonavane K, Ekshyyan O, Mclarty J, Nathan CO. Curcumin Inhibits UV Radiation–Induced Skin Cancer in SKH-1 Mice. Otolaryngol Neck Surg 2013;148:797–803. https://doi.org/10.1177/0194599813476845.
[117] Reisman ASA, Lee CI, Meyer CJ, Proksch JW, Sonis ST, Reisman SA, et al. Topical Application of the Synthetic Triterpenoid RTA 408 Protects Mice from Radiation-Induced Dermatitis. Radiat Res 2014;181:512–20. https://doi.org/10.1667/RR13578.1.
[118] Benavidesa F, Oberyszynb TM, VanBuskirkc AM, Reeved VE, Kusewitt DF. The hairless mouse in skin research. J Dermatol Sci 2009;53:10–8. https://doi.org/10.1016/j.jdermsci.2008.08.012.The.
[119] Brown FB. MCPN5 development, verification, and performance n.d.
[120] Brown F, Kiedrowski B, Bull JS, Gonzales M, Gibson N. Verification of MCNP5-

1.60. LA-UR-10-05611 2010.

APPENDIX A

Table A.1: Monte Carlo simulation parameters.

Item name	Description	Reference
Code, version	MCNP5 version 1.6 (2008)	[100,119]
Validation	Previously validated	[120]
Timing	CPU time was on the order of 10^4 minutes.	
Source description	Cylinder with base parallel to phantom surface. • radius: 1.01 mm • diameter: 2.03 mm • mass density: 4.47 g/cm^3 ^{90}Y β^- spectrum from ICRU56, Table D.1.	[22]
Cross-sections	EL03 electron physics library database MCPLIB04 photoatomic library database	[94,95]
Transport parameters	Photon-electron mode Electron cut-off below 50 keV H2O material card set to ESTEP = 10	
Scored quantities	*F8 tally: Energy deposited per unit voxel. Voxel size: 0.01 × 0.01 × 0.01 cm^3.	
# histories/ statistical uncertainty	Single source: 5×10^7 histories. Seven sources: 6×10^8 histories. Type A uncertainties (k=1) <10% for within region of interest.	
Post-processing	Energy deposited in each voxel (MeV) was converted to cGy by converting MeV to centi-Joules and dividing by the mass of each voxel (kg). The point of measurement of each voxel was considered to be the exact center of each voxel.	

APPENDIX B

The following MCNP5 input script is an example of what was used for the work presented in this document. The code can be saved in notepad and initiated with MCNP5. It simulates the energy deposited in a water phantom from a ^{90}Y tip-source-rod assembly placed directly on the surface of the phantom. The source card contains all of the geographic information of the remaining 18 sources of the CSBT.

▼▼▼▼▼▼▼DO NOT COPY THIS LINE▼▼▼▼▼▼▼

```
c
c              Cell Card
c ccccccccccccccccccccccccccccccccccccccccccccccccc
c
3    1    -4.47    -3                          $ source
203  6    -1.1     -203   3     303  403  503    $ truncated cone
303  2    -0.0013  -203  #203  #3   #403         $ air
403  201  -15.63   -403  #3                    $ rod
c
c     tally voxels
103 3 -0.998 -103 fill=2
101 3 -0.998 -101 u=1
111 3 -0.998  101 u=1
102 3 -0.998 -102 lat=1 u=2 fill=1
c
100 3 -0.998 -100 #103              $ H2O phantom
c
999  2 -0.0013 -999 100 203  403     $ world
9990 0 999                          $ universe
```

```
c

c                SURFACE CARD
c ccccccccccccccccccccccccccccccccccccccccccccccccc
999 RPP -11   11  -11   11   -15    21          $world
c
c    Sources
c
1 RCC -0.9 0 -0.05 0 0 -0.101 0.1015             $ source
501 TRC -0.9 0 -0.05 0 0 -0.11 0.1075 0.1294     $ truncated cone
201 RCC -0.9 0 0 0 0 -0.8 0.165                  $ tip outer
301 RCC -0.9 0 0 0 0 -0.05 0.08                  $ source opening
401 RCC -0.9 0 -0.16 0 0 -10 0.14 $ rod
c
2 RCC -0.45 0 -0.05 0 0 -0.101 0.1015            $ source
502 TRC -0.45 0 -0.05 0 0 -0.11 0.1075 0.1294    $ truncated cone
202 RCC -0.45 0 0 0 0 -0.8 0.165                 $ tip outer
302 RCC -0.45 0 0 0 0 -0.05 0.08                 $ source opening
402 RCC -0.45 0 -0.16 0 0 -10 0.14               $ rod
c
3 RCC 0 0 -0.05 0 0 -0.101 0.1015                $ source
503 TRC 0 0 -0.05 0 0 -0.11 0.1075 0.1294        $ truncated cone
203 RCC 0 0 0 0 0 -0.8 0.165                     $ tip outer
303 RCC 0 0 0 0 0 -0.05 0.08                     $ source opening
403 RCC 0 0 -0.16 0 0 -10 0.14                   $ rod
c
4 RCC 0.45 0 -0.05 0 0 -0.101 0.1015             $ source
504 TRC 0.45 0 -0.05 0 0 -0.11 0.1075 0.1294     $ truncated cone
204 RCC 0.45 0 0 0 0 -0.8 0.165                  $ tip outer
304 RCC 0.45 0 0 0 0 -0.05 0.08                  $ source opening
404 RCC 0.45 0 -0.16 0 0 -10 0.14                $ rod
c
5 RCC 0.9 0 -0.05 0 0 -0.101 0.1015              $ source
505 TRC 0.9 0 -0.05 0 0 -0.11 0.1075 0.1294      $ truncated cone
205 RCC 0.9 0 0 0 0 -0.8 0.165                   $ tip outer
305 RCC 0.9 0 0 0 0 -0.05 0.08                   $ source opening
405 RCC 0.9 0 -0.16 0 0 -10 0.14                 $ rod
c
6 RCC -0.675 0.389711432 -0.05 0 0 -0.101 0.1015         $ source
506 TRC -0.675 0.389711432 -0.05 0 0 -0.11 0.1075 0.1294 $ truncated cone
206 RCC -0.675 0.389711432 0 0 0 -0.8 0.165              $ tip outer
306 RCC -0.675 0.389711432 0 0 0 -0.05 0.08              $ source opening
406 RCC -0.675 0.389711432 -0.16 0 0 -10 0.14            $ rod
```

```
c
7 RCC -0.225 0.389711432 -0.05 0 0 -0.101 0.1015          $ source
507 TRC -0.225 0.389711432 -0.05 0 0 -0.11 0.1075 0.1294    $ truncated cone
207 RCC -0.225 0.389711432 0 0 0 -0.8 0.165               $ tip outer
307 RCC -0.225 0.389711432 0 0 0 -0.05 0.08               $ source opening
407 RCC -0.225 0.389711432 -0.16 0 0 -10 0.14             $ rod
c
8 RCC 0.225 0.389711432 -0.05 0 0 -0.101 0.1015           $ source
508 TRC 0.225 0.389711432 -0.05 0 0 -0.11 0.1075 0.1294     $ truncated cone
208 RCC 0.225 0.389711432 0 0 0 -0.8 0.165                $ tip outer
308 RCC 0.225 0.389711432 0 0 0 -0.05 0.08                $ source opening
408 RCC 0.225 0.389711432 -0.16 0 0 -10 0.14              $ rod
c
9 RCC 0.675 0.389711432 -0.05 0 0 -0.101 0.1015           $ source
509 TRC 0.675 0.389711432 -0.05 0 0 -0.11 0.1075 0.1294     $ truncated cone
209 RCC 0.675 0.389711432 0 0 0 -0.8 0.165                $ tip outer
309 RCC 0.675 0.389711432 0 0 0 -0.05 0.08                $ source opening
409 RCC 0.675 0.389711432 -0.16 0 0 -10 0.14              $ rod
c
10 RCC -0.45 0.779422863 -0.05 0 0 -0.101 0.1015          $ source
510 TRC -0.45 0.779422863 -0.05 0 0 -0.11 0.1075 0.1294     $ truncated cone
210 RCC -0.45 0.779422863 0 0 0 -0.8 0.165                $ tip outer
310 RCC -0.45 0.779422863 0 0 0 -0.05 0.08                $ source opening
410 RCC -0.45 0.779422863 -0.16 0 0 -10 0.14              $ rod
c
11 RCC 0 0.779422863 -0.05 0 0 -0.101 0.1015              $ source
511 TRC 0 0.779422863 -0.05 0 0 -0.11 0.1075 0.1294         $ truncated cone
211 RCC 0 0.779422863 0 0 0 -0.8 0.165                    $ tip outer
311 RCC 0 0.779422863 0 0 0 -0.05 0.08                    $ source opening
411 RCC 0 0.779422863 -0.16 0 0 -10 0.14                  $ rod
c
12 RCC 0.45 0.779422863 -0.05 0 0 -0.101 0.1015           $ source
512 TRC 0.45 0.779422863 -0.05 0 0 -0.11 0.1075 0.1294      $ truncated cone
212 RCC 0.45 0.779422863 0 0 0 -0.8 0.165                 $ tip outer
312 RCC 0.45 0.779422863 0 0 0 -0.05 0.08                 $ source opening
412 RCC 0.45 0.779422863 -0.16 0 0 -10 0.14               $ rod
c
13 RCC -0.675 -0.389711432 -0.05 0 0 -0.101 0.1015          $ source
513 TRC -0.675 -0.389711432 -0.05 0 0 -0.11 0.1075 0.1294    $ truncated cone
213 RCC -0.675 -0.389711432 0 0 0 -0.8 0.165              $ tip outer
313 RCC -0.675 -0.389711432 0 0 0 -0.05 0.08              $ source opening
413 RCC -0.675 -0.389711432 -0.16 0 0 -10 0.14            $ rod
c
```

```
14 RCC -0.225 -0.389711432 -0.05 0 0 -0.101 0.1015          $ source
514 TRC -0.225 -0.389711432 -0.05 0 0 -0.11 0.1075 0.1294   $ truncated cone
214 RCC -0.225 -0.389711432 0 0 0 -0.8 0.165                $ tip outer
314 RCC -0.225 -0.389711432 0 0 0 -0.05 0.08                $ source opening
414 RCC -0.225 -0.389711432 -0.16 0 0 -10 0.14              $ rod
c
15 RCC 0.225 -0.389711432 -0.05 0 0 -0.101 0.1015           $ source
515 TRC 0.225 -0.389711432 -0.05 0 0 -0.11 0.1075 0.1294    $ truncated cone
215 RCC 0.225 -0.389711432 0 0 0 -0.8 0.165                 $ tip outer
315 RCC 0.225 -0.389711432 0 0 0 -0.05 0.08                 $ source opening
415 RCC 0.225 -0.389711432 -0.16 0 0 -10 0.14               $ rod
c
16 RCC 0.675 -0.389711432 -0.05 0 0 -0.101 0.1015           $ source
516 TRC 0.675 -0.389711432 -0.05 0 0 -0.11 0.1075 0.1294    $ truncated cone
216 RCC 0.675 -0.389711432 0 0 0 -0.8 0.165                 $ tip outer
316 RCC 0.675 -0.389711432 0 0 0 -0.05 0.08                 $ source opening
416 RCC 0.675 -0.389711432 -0.16 0 0 -10 0.14               $ rod
c
17 RCC -0.45 -0.779422863 -0.05 0 0 -0.101 0.1015           $ source
517 TRC -0.45 -0.779422863 -0.05 0 0 -0.11 0.1075 0.1294    $ truncated cone
217 RCC -0.45 -0.779422863 0 0 0 -0.8 0.165                 $ tip outer
317 RCC -0.45 -0.779422863 0 0 0 -0.05 0.08                 $ source opening
417 RCC -0.45 -0.779422863 -0.16 0 0 -10 0.14               $ rod
c
18 RCC 0 -0.779422863 -0.05 0 0 -0.101 0.1015               $ source
518 TRC 0 -0.779422863 -0.05 0 0 -0.11 0.1075 0.1294        $ truncated cone
218 RCC 0 -0.779422863 0 0 0 -0.8 0.165                     $ tip outer
318 RCC 0 -0.779422863 0 0 0 -0.05 0.08                     $ source opening
418 RCC 0 -0.779422863 -0.16 0 0 -10 0.14                   $ rod
c
19 RCC 0.45 -0.779422863 -0.05 0 0 -0.101 0.1015            $ source
519 TRC 0.45 -0.779422863 -0.05 0 0 -0.11 0.1075 0.1294     $ truncated cone
219 RCC 0.45 -0.779422863 0 0 0 -0.8 0.165                  $ tip outer
319 RCC 0.45 -0.779422863 0 0 0 -0.05 0.08                  $ source opening
419 RCC 0.45 -0.779422863 -0.16 0 0 -10 0.14                $ rod
c
c
c        PHANTOM
100 1 RPP -5 5 -5 5 0 10
101 1 RPP -0.01 0.01 -0.01 0.01 0.0070962 0.0270962
102 1 RPP -0.01 0.01 -0.01 0.01 0.0070962 0.0270962
103 1 RPP -0.01 1.51 -0.01 1.51 0.0070962 1.0270962
c
```

```
c ccccccccccccccccccccccccccccccccccccccccccccccccc

c DATA CARDS
c
c                  MOD CARD
CUT:e j 0.05  $50 keV electron cutoff
c
c
c                  TRANSFORMATIONS
c
c TRn X Y Z or TRn X Y Z B1 B2 B3 B4 B5 B6 B7 B8 B9 M
c Default: TRn 0 0 0 1  0  0  0  1  0  0  0  1  1
c
TR1  0 0 0.0     $ Altering the Z (3rd entry) alters the tip-to-surface distance by shifting
the phantom and tally voxels.
c
c
c                 MATERIAL CARD
c
m1  039090  1   COND=-1                          $ yttrium (4.47 g/cm3)
m2  007014 -0.7809  008016 -0.2095  018040 -0.0096    $ air (0.0013 g/cm3)
m3  001001 2 008016 1  ESTEP=10                    $ water (1.1 g/cm3)
m6  6012   5 8016 2 1001 8                        $ PMMA-C5O2H8 (1.1 g/cm3)
m201 74000 -0.5 8016 -0.5                         $ Tungsten Carbide W(50%) C(50%)
(15.63 g/cm3)
c
c
c  MODE AND IMPORTANCE CARD
c
MODE p e
IMP:p,e 1 9R 0
c
c
c  SOURCE CARD
c
SDEF ERG=d111  PAR=3 POS=d3 RAD=d6 EXT=d7 AXS=0 0 1
c
SI3 L  0  0 -0.05
SP3    1
c
SI6   0    0.1015
SP6  -21   1
c
```

```
SI7  -0.101  0
SP7   0      1
c
c
c     Y90 Beta Spectrum (ICRU 56)
SI111 A 0          &
       0.057025    &
       0.11405     &
       0.171075    &
       0.2281      &
       0.285125    &
       0.34215     &
       0.399175    &
       0.4562      &
       0.513225    &
       0.57025     &
       0.627275    &
       0.6843      &
       0.741325    &
       0.79835     &
       0.855375    &
       0.9124      &
       0.969425    &
       1.02645     &
       1.083475    &
       1.1405      &
       1.197525    &
       1.25455     &
       1.311575    &
       1.3686      &
       1.425625    &
       1.48265     &
       1.539675    &
       1.5967      &
       1.653725    &
       1.71075     &
       1.767775    &
       1.8248      &
       1.881825    &
       1.93885     &
       1.995875    &
       2.0529      &
       2.109925    &
```

```
      2.16695   &
      2.223975  &
      2.281
c
SP111 0.018850165  &
      0.021029947  &
      0.023407892  &
      0.025562904  &
      0.027494984  &
      0.029204132  &
      0.030690347  &
      0.0319784    &
      0.033068292  &
      0.033984791  &
      0.034703128  &
      0.035545317  &
      0.035743479  &
      0.03581779   &
      0.035768249  &
      0.035619628  &
      0.035371925  &
      0.035025142  &
      0.034554507  &
      0.034009561  &
      0.033365535  &
      0.032572886  &
      0.031681157  &
      0.030665577  &
      0.029501375  &
      0.028188551  &
      0.026702336  &
      0.025067499  &
      0.02325927   &
      0.02130242   &
      0.019196948  &
      0.016942855  &
      0.014589681  &
      0.012186966  &
      0.009759481  &
      0.007381536  &
      0.005127443  &
      0.003145822  &
      0.001510986  &
```

```
     0.000421094   &
     0
c
c  TALLY CARD
c
prdmp 2j 1                    $Create MCTal Output File
NPS 1E8                       $ number of histories
RAND SEED = 7515569547                $ beginning random number
dbcn 17j 2                    $ use detailed Landau straggling logic (energy- and step-
specific)
*F18:p,e (101<102[0:37 0:37 00:00]<103)      $ depth = 0.0171 cm
c
c    Tally
*F28:p,e (101<102[37:37 37:37 05:05]<103)    $ depth = 0.1171 cm
*F38:p,e (101<102[37:37 37:37 10:10]<103)    $ depth = 0.2171 cm
*F48:p,e (101<102[37:37 37:37 15:15]<103)    $ depth = 0.3171 cm
*F58:p,e (101<102[37:37 37:37 20:20]<103)    $ depth = 0.4171 cm
PRINT
▲▲▲▲▲▲▲ DO NOT COPY THIS LINE ▲▲▲▲▲▲▲
```